Streaking and Splashing:

Design of a Grazing Incidence X-ray Streak Camera and Time-resolved Measurements of the Structure of Water.

A Thesis Submitted in Fulfillment of the
Requirements for the Degree of
Doctor of Philosophy
in
Electronic Engineering

By
Mr Donnacha Lowney
B Eng , M Eng , C Eng , MIEE, MIEEE

School of Electronic Engineering
Faculty of Engineering and Computing
Dublin City University

Research Supervisors
Prof Patrick J McNally (Dublin City University)
Dr Philip Heimann (Lawrence Berkeley National Laboratory)

May 2006

Declaration

I hereby certify that this material, which I now submit for assessment on the programme of study leading to the award of Doctor of Philosophy in Electronic Engineering is entirely my own work and has not been taken from the work of others save and to the extent that such work has been cited and acknowledged within the text of my work

Signed *Donnacha Lowney*   Date *18/5/2006*

Acknowledgments

The streak camera design would not have been possible without the helpful insights provided by Andrew MacPhee and Dana Weinstein During testing Maik Kaiser of the Swiss Light Source and Zhao Hao were invaluable Jung Feng and Tony Young were very generous with equipment and access time on the beamline 4 laser system Ali Belkacem provided the high voltage pulser and MCP

The collaboration of Eric Gullikson, Andy Aquila and Anton Tremsin during the cesium iodide and diamond photocathode characterisation measurements is acknowledged Thierry Boutboul of CERN also provided his expertise in the Monte Carlo simulations relating to secondary electron transit times in photocathodes

It was also a privilege to take part in the first measurements at the Sub-Picosecond Photon Source (SPPS) at SLAC It would be impossible to name everyone involved given the size and nature of the experiment but it was quite interesting to watch the old dogs teaching the young pups a few new tricks

This work was helped on a daily basis behind the scenes by the technical and user support staff of the ALS Rich Celestre who was always helpful when we managed to fry a motor (or ten), James, Ron, Tim, Tony and Pete of the EM shop, Steve Clinger and Frank Zucca of vacuum support services, Todd, Gary, Kenny and Tony of user services, Steve Cooper and his colleagues in electrical services, Wayno Oglesby, John Hodrige and the staff of the building 80 machine shop, Tom West and Curtis Cummings of the engineering division, John Pruyn for his help with horrible chemicals and his insights into John Steinbeck, Donna Hammamoto and Will Thur, the ESG group secretaries, Marsha Fenner and Cathy Cooper, and, Everett and Tim from computer services I apologise to and thank any person I may have forgotten to mention

My research was also selflessly supported from afar by Patrick McNally in Dublin City University I consider it a privilege to count him as a friend and I would like to thank Pat for his continued encouragement and support, especially during difficult times He has opened many doors for me including the first beam shutter when we started frying LEDs late one night under the beam at HASYLAB beamline F-1 Pat knocked over the first domino in the chain of events that eventually led to this thesis and I'll be ever grateful I would also like to thank Jim Dowling and Charles McCorkell for the encouragement to pursue such an unconventional PhD for an engineer

A very special debt of gratitude goes to my family and friends who've supported me in all my endeavors to date Mam, Dad, Fintan, Ronan and Ethel thank you for your phone calls and visits, especially the calls from the bow of an oil tanker at 4 in the morning explaining the latest shannanigans back home ,-)

Finally, I'd like to thank my wife Eilish who often felt like she'd become a synchrotron widow with the anti-social hours that come with synchrotron life Without her unfailing love and encouragement throughout this thesis, I'm one hundred percent sure I'd have thrown the hat in a long time ago Thanks BM2K :-x

Thank you, one and all

Donnacha Lowney, December 2005

Dedication

Le Eilísh

Mo ghrá,
Mo chroí,
Mo shaol

Abstract

Streaking and Splashing:

Design of a Grazing Incidence X-ray Streak Camera and
Time-resolved Measurements of the Structure of Water

Mr Donnacha Lowney

The performance of cesium iodide photocathodes has been characterized for use with grazing incidence soft x-rays The total electron yield and pulsed quantum efficiency has been measured in a reflection geometry as a function of photon energy (100 eV to 1 keV), angle of incidence, and the electric field between the anode and photocathode The total electron yield and pulsed quantum efficiency increase as the x-ray penetration depth approaches the secondary electron escape depth Unit quantum efficiency in a grazing incidence geometry is demonstrated A weak electric-field dependence is observed for the total yield measurements, while no significant dependence is found for the pulsed quantum efficiency The effect of the pulse height distribution on the detective quantum efficiency is discussed Theoretical predictions agree accurately with experiment

Demonstrated unit quantum efficiency in a reflection geometry motivated the development of a grazing incidence x-ray streak camera for the Ultrafast X-ray Science beamline, under construction at the Advanced Light Source, Lawrence Berkeley National Laboratory, USA Design considerations particular to synchrotron radiation sources are discussed An analytical model and particle simulation for a camera incorporating magnetostatic imaging and meander sweep plates is presented The camera is characterised with the third harmonic from a titanium-sapphire based laser system, 70 ps intrinsic and 150 fs "sliced" x-ray photon pulses from a synchrotron bend magnet source A grazing incidence x-ray streak camera with an instrument temporal response of 6 ps is demonstrated

Dynamical changes in the structure factor of liquid water are measured using time-resolved x-ray diffraction techniques with 100 ps resolution On short time scales, before the system has had time to expand following femtosecond optical excitation, temperature-induced changes associated with rearrangements of the hydrogen-bonded structure at constant volume are observed Transient changes in the pair correlation function associated with isochoric heating effects are extracted and interpreted in terms of a decrease in the local tetrahedral ordering in the liquid

Contents

List of Tables

'

List of Figures

Chapter 1

Introduction

To gain a fundamental understanding of chemical, physical and biological reactions one needs to probe matter on timescales corresponding to vibrational periods of atoms (~ 1 fs or 10^{-15} s) with spatial resolution close to inter-atomic dimensions (~ 1 Å or 10^{-10} m) Ultrafast x-ray science aims to probe this phase space and beyond A schema of typical transient processes and the length scales upon which they occur is shown in Figure 1 1 The field is the progeny of two branches of photonic science x-rays, discovered by Rontgen [2] in 1896, and the laser, invented by Gould [3, 4] in 1957 X-ray scattering techniques have been employed to determine the structure of all manner of condensed matter samples, most notably the structure of DNA [5], whilst the most recent Nobel prize has been awarded in part for the development of laser-based precision spectroscopy, including the optical frequency comb technique [6] Contemporary optical-pump x-ray probe techniques have reached a level of sophistication wherein it has been possible to resolve the onset of liquid-like motion during non-thermal melting of semi-conductors [7, 8], coherent motion of optical phonons [9] and insulator-metal phase transitions [10] with the femtosecond-Ångstrom precision prescribed above Other work on a picosecond timescales has captured the functional mechanism of the myoglobin protein [11], mimicked the liquid carbon inside the planets Uranus and Neptune [12], and brought insight into magnetization dynamics of ferromagnetic vortices [13], a problem of major technological importance

The scientific achievements made in the field to date have relied intimately on the photon sources and detectors employed This symbiotic relationship is certain to continue in the future An extremely tantalising scientific case is awaiting exploration with the sources presently under development Feasible experiments include, non-crystallised single protein imaging with X-ray Free Electron Lasers (XFELs) [14] and realtime measurement of the electronic structure of atoms with attosecond pulse trains from high harmonic laser systems [15, 16] A potentially viable hybrid scheme has been suggested that purports to generate intense "seeded attosecond x-ray radiation" from an XFEL source [17] Such a source, with the ability to probe sub-Ångstrom spatial dimensions with attosecond temporal resolution, will surely be as revolutionary as the laser and x-ray were in their own right

ablation →

10⁻⁹ s — 1 ns ↕ gigahertz electronics

heat diffusion ↕

Optical ← telecommunications

storage ring pulse ↕ ↕ phonon-phonon scattering

thermal melting ↑
– – – –
non-thermal melting ↓

10⁻¹² s — 1 ps ↕ molecular vibrations & acoustic phonons

x-ray streak camera →

↕ carrier-phonon scattering

electron decoherence in semiconductors →

↕ optical oscillation period

Ti : Sapphire laser pulse ↕ ↕ optical phonons

10⁻¹⁵ s — 1 fs ↕ carrier-carrier scattering

Electron orbital period in H atom →

10⁻¹⁸ s — 1 as

x-ray oscillation period @ 12.4 keV ←

10⁻⁶ m — 1 µm

optical wavelengths ↕

optical microscope resolution ←

Cu track thickness →

Transistor gate oxide →

DNA helix diameter ←

10⁻⁹ m — 1 nm

Semiconductor bond length ↕

water molecule diameter →

TEM resolution ←

Bohr radius →

x-ray wavelength ← @ 12.4 keV

10⁻¹² m — 1 pm

Au nucleus diameter →

10⁻¹⁵ m — 1 fm

Proton diameter ←

Figure 1.1: Schema illustration different time and length scales probed by time-resolved techniques. Adapted from Figure 6.1 in [1].

Relative to the experimental demands, the intensity of current picosecond and femtosecond x-ray sources is quite low [18] Thus detector and experiment optimisation is of paramount importance This thesis is concerned with the development of experimental methodologies and instrumentation for contemporary and future ultrafast x-ray sources Specifically, a grazing incidence x-ray streak camera is constructed and a method to determine the structure of liquid water in an isochoric non-equilibrium transient state is presented As such this is a thesis of two halves

A state of the art synchrotron based femtosecond photon source is presently under construction at the Advanced Light Source, Lawrence Berkeley National Laboratory In short, the "slicing" mechanism modulates a storage ring electron bunch (of duration ~ 100 ps) with the electric field of an ultrafast optical laser (of duration ~ 100 fs) [19, 20] Thus a femtosecond imprint of the laser pulse duration is sliced into the picosecond electron bunch In a dispersive part of the storage ring the electrons lose energy by synchrotron radiation production [21] A femtosecond pulse spatially displaced from the picosecond background is produced This pulse possesses all the intrinsic properties of synchrotron radiation a continuous spectrum of radiation extending from the infrared to the hard x-ray region, high degree of polarisation and low divergence [22] At present no other tunable femtosecond spectral source exists with superior characteristics The potential of the source is well recognised within the scientific community with several other synchrotrons (BESSY and SLS) developing their own slicing programs

Absolute discrimination of the sliced photons from the picosecond background is not possible because of the imperfect imaging of the electron source Hence sliced photons co-propagate with picosecond background scatter For an integrating detector, whose response time is much greater than the duration of the picosecond pulse, the relatively weak sliced photon signal is degraded by the background photon shot noise The signal to noise ratio can be improved and the integration times significantly reduced if a detector with temporal resolution on the order of a picosecond is employed Thus temporal discrimination, achievable with a streak camera, will effectively reduce the background contribution by the ratio of the background pulse duration to the streak camera time resolution

A streak camera converts the temporal history of a photonic signal (optical or X-ray) into spatial information An analogous example would be a standard laboratory oscilloscope wherein an electrical signal is displayed on a phosphor screen A schematic illustrating the principle of operation is shown in Figure 1 2 on page 4 Photons strike a photocathode and generate low energy electrons These are accelerated away from the cathode by biasing the photocathode at a potential less than the anode (nominally a few kV) As the electrons traverse the sweep plates, a symmetric linearly ramped electrical pulse co-propagates along the serpentine traces The electrical pulse is derived from a photoconductive switch [23] The electrical field between the plates due to the pulse is orthogonal to the direction

3
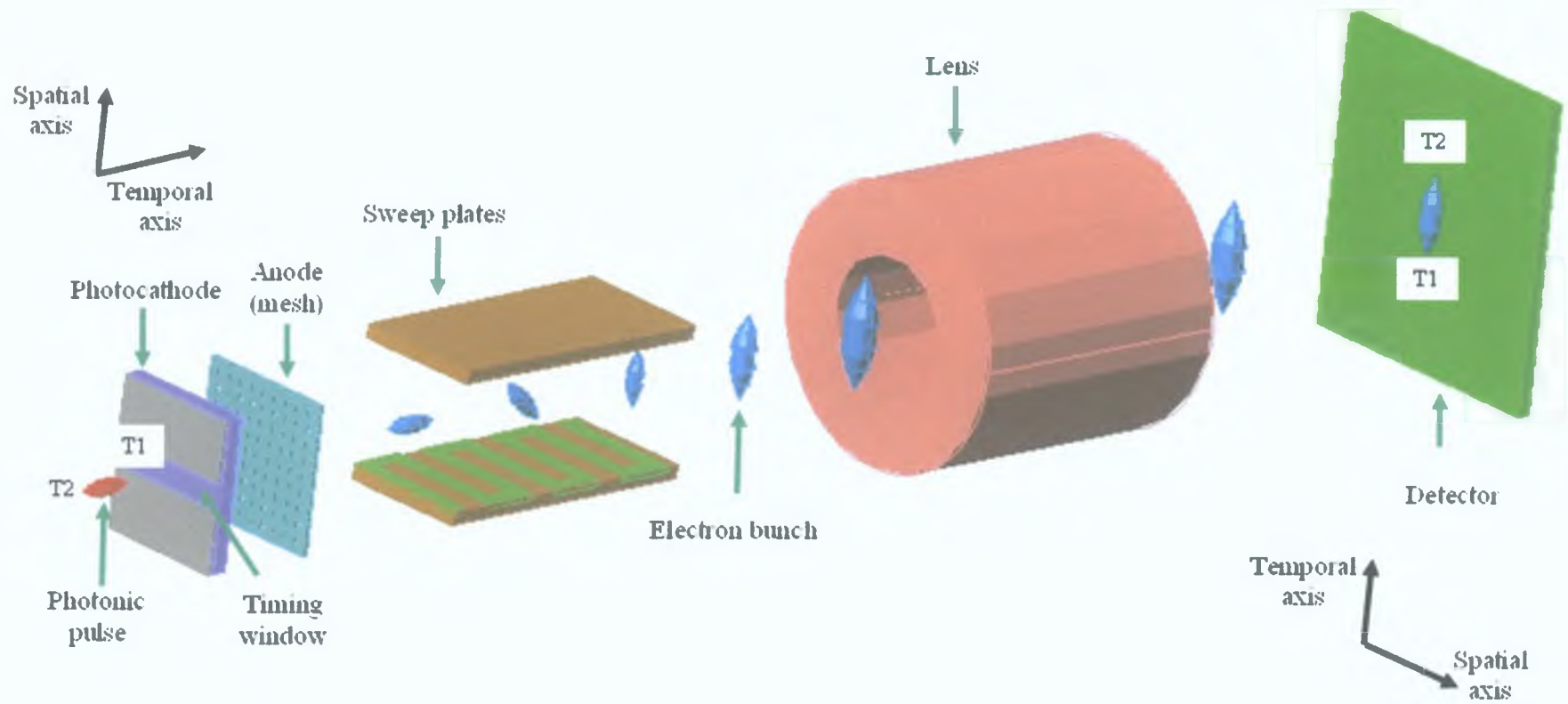
Figure 1.2: Schematic illustrating streak camera operation principle. Not drawn to scale.

of electron motion Electrons at the front of the bunch experience a different electric field and consequently experience a different deflection compared to those at the tail of the bunch Thus, the temporal history of the photonic signal is converted into a spatially dependent signal and imaged on a 2-D detector such as a CCD using electrostatic or magnetostatic electron optics In summary, the spatial extent of the photon beam along the swept axis, of dimension w_{dc}, is streaked across the camera with sweep speed v_{sweep} The ultimate temporal resolution of the camera is thus given by

$$\tau_{dc} = \frac{w_{dc}}{v_{sweep}} \tag{1 1}$$

However, it will be appreciated that timing jitter, space charge and electron chromaticity effects can degrade the temporal resolution of the instrument $\tau_{instrument} < \tau_{dc}$

Since the development of the first streak camera employing electrostatic deflection by Courtney-Pratt in 1949 [24], there has been a monotonic increase in temporal resolution with current state of the art cameras demonstrating 280 fs at ultraviolet wavelengths This value has been recorded by Man Shakya and Chang under idealised experimental circumstances at visible wavelengths [25] Still the ultimate resolution of 10 fs suggested by Zavoisky and Fanchenko [26] has remained illusive and is perhaps even theoretically impossible with current streak camera technology

Two factors, intrinsic to the photocathode, differentiate x-ray streak cameras from their visible cousins First, x-rays produce low energy secondary electrons following the decay of fast high energy primary electrons created by the initial photon absorption event The resulting secondary electron energy distribution (typically on the order of a few eV, compared to the kT scale distribution created by visible photons) leads to temporal dispersion in acceleration and drift regions of the camera This degrades the temporal resolution The best temporal resolution achieved with an x-ray streak camera to date is sub-600 fs [27,28] Second, the quantum efficiency of the cathodes employed in x-ray streak cameras is significantly lower than at optical wavelengths This characteristic has particular consequence for this thesis

The low quantum efficiency of x-ray photocathodes excited at normal incidence is due the large mismatch between the penetration depth of the x-ray (typically a few micrometers) and the secondary electron escape depth (generally less than 30 nm) Only x-rays absorbed within a mean free path of the secondary electron exit surface contribute to the measured signal Quantum efficiencies between 0 1 % and 10 % are typical This implies for the slicing process the gain achieved by the increased temporal resolution has been lost by the reduced detection efficiency This can be avoided and one can recover the improved signal to noise ratio if the cathode is excited in a grazing incidence geometry with the penetration depth of the x-ray matched to the secondary electron escape depth

5

Measurements of cesium iodide photocathodes discussed in Chapter 2 demonstrate that it is possible to achieve unit quantum efficiency in a reflection geometry. The total electron yield and pulsed quantum efficiency has been measured in a reflection geometry as a function of photon energy (100 eV to 1 keV), angle of incidence, and the electric field between the anode and photocathode. An increase in the total electron yield and pulsed quantum efficiency is observed as the x-ray penetration depth approaches the secondary electron escape depth. The electric field dependence is also investigated. Predictions made using Fraser's theory [29,30] agree with measurement.

Demonstration of unit quantum efficiency in a reflection geometry promoted the design and construction of the grazing incidence x-ray streak camera described in Chapter 3. A careful analysis of the design considerations imposed by the slicing beamline was undertaken. A novel approach to sweep plate structure design, wherein a compromise is struck between forward coupled crosstalk of the sweep ramp and the effect of inter-track spacing on the sweep speed, is presented. The resulting camera design was modeled analytically by following a paraxial electron trajectory through the camera using elementary electrodynamics and kinematics. Space charge and fringe field effects, neglected in the analytical model, were incorporated in a full particle simulation of the camera. Close agreement between the analytical and empirical models is obtained. The constructed camera was characterised by impulsive excitation with ultraviolet photons from a femtosecond laser system. This measurement facilitated a clean calibration of the temporal resolution and sweep speed. The camera's response to soft x-ray sliced and unsliced photons from the Advanced Light Source was measured. A streak camera possessing an instrument temporal resolution of 6 ps with sufficient sensitivity to detect sliced photons is demonstrated.

In the latter part of this thesis the technique of time-resolved x-ray diffuse scattering is used to examine a non-equilibrium isochoric transient state of liquid water. Water appears to make our planet unique among the celestial bodies and is directly tied to the genesis of life. Approximately three quarters of our planet surface is covered with water and it contributes a similar fraction to our body mass. Water is perhaps the most important and ubiquitous molecule of all. For example, it regulates all aspects of our bio-sphere from temperature to precipitation, acts as a medium for all manner of bio-chemical reactions and defines the geography and topography of our environment. Yet for all its prevalence within and importance to our society, a complete physical picture of the structure of liquid water still eludes us. Why?

The molecule itself is covalently bonded and like all other molecules experiences attractive and repulsive van der Waals forces. What sets this molecule apart from many others and points toward an answer to the previous question is the additional force due to the transient strongly directional hydrogen bonded network. Rotational fluctuations involving a few molecules occur on femtosecond timescales [31], whilst in the picosecond domain,

diffusive motion resulting in the breaking and forming of hydrogen bonds transpires [32] The dynamic hydrogen bonded network is responsible for water's properties including its anomalous ones and its complicated phase diagram [33] Forty-one anomalies have been cited in the literature [34] Typical examples include a density maximum and an isobaric specific heat minimum as a function of temperature [35, 36], and a fast sound anomaly wherein sound propagates at about twice its normal velocity [37, 38] Traditionally, a locally coordinated tetrahedral structure has been ascribed to the liquid (see Figure 1 3 (b) on page 8), wherein each water molecule is hydrogen bonded to four nearest neighbours via two donor bonds (the OH group donating hydrogen bonds to neighbouring oxygen atoms) and two acceptor bonds (the lone electron pair on the oxygen atom accepting hydrogen bonds from other water molecules) [39] Whilst this is the view accepted and developed within this thesis significant controversy still surrounds the aqueous structure For example, Nilsson et al purport that liquid water comprises a large fraction of broken hydrogen bonds and that on average each molecule only forms two strong hydrogen bonds [43] This implies a ring or chain-like molecular arrangement in stark contrast to the tetrahedral model supported by the Saykally group [44] and others

The average local structure has been determined statically using x-ray diffraction [39, 45–48], x-ray absorption spectroscopy [49–52], x-ray Raman scattering [53, 54], x-ray photoemission spectroscopy [55, 56] and neutron scattering [48, 57, 58] These studies have been supported by a number of theoretical studies and molecular dynamics simulations [59–62] Each experimental technique has its own advantages and disadvantages

For scattering experiments, complimentary data is obtained using x-rays and neutrons X-rays probe atomic dimensions on the order of magnitude of the x-ray wavelength by scattering elastically from the electron cloud, the intensity of the measured signal being proportional to the square of the number of electrons Thus x-ray diffraction is primarily sensitive to the oxygen-oxygen radial distribution function and it is difficult though not impossible to detect changes due to isotopic substitution [63] In contrast, neutrons interact directly with the nuclei within a molecule making the technique extremely sensitive to both the hydrogen-hydrogen and oxygen-hydrogen radial distribution functions [58] Isotopic substitution is often employed in neutron scattering measurements of liquid water Both techniques are sensitive to the liquid bulk with significantly faster data acquisition times offered by x-ray diffraction over neutron scattering

The near edge x-ray absorption (NEXAFS or XANES) [64] and extended x-ray absorption fine structure (EXAFS) [65] spectroscopic techniques are element specific and particularly suited to the measurement of disordered media The techniques provide related but slightly different information by probing the unoccupied dipole-allowed one electron density of states The former applies when the photon excitation energy is within ~ 50 eV of the absorption edge and typically provides information on the chemical state, whilst

7

(a) Solvated electron.   (b) Water cluster.   (c) Eigen solvated proton.   (d) Zundel solvated proton.
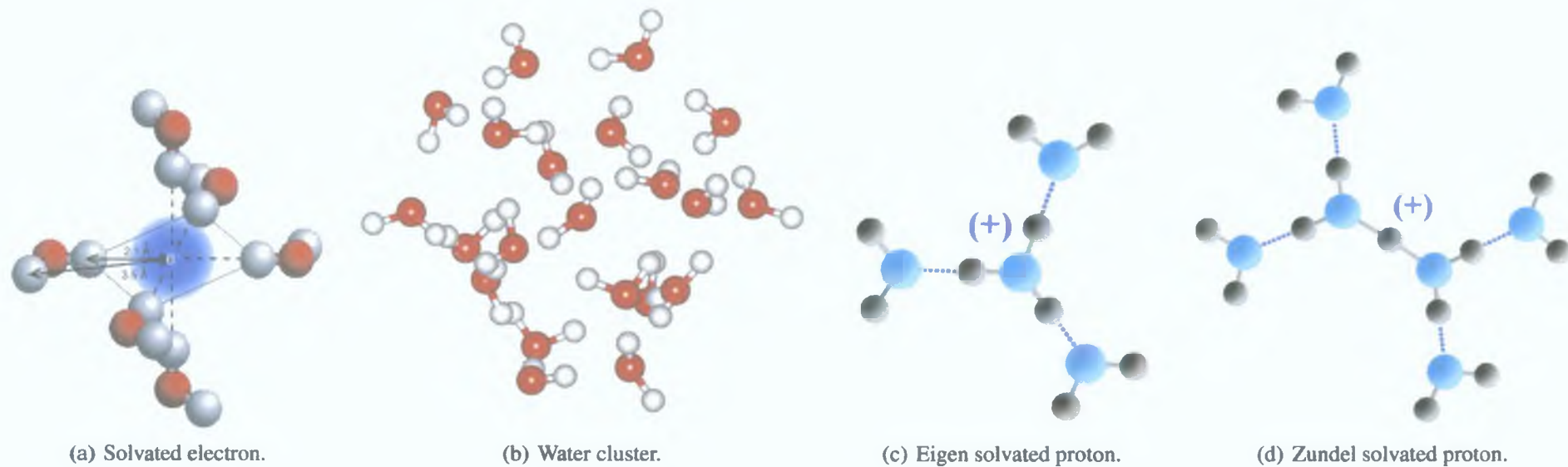
Figure 1.3: Ball and stick models of (a) solvated electron, (b) tetrahedrally co-ordinated water molecule, (c) Eigen model $(H_9O_4)^+$ and (d) Zundel model $(H_5O_2)^+$ of solvated proton, respectively. In the case of the water cluster (b), one can clearly see the presence of two acceptor electron sites on the oxygen atom and two hydrogen atoms participating in H-bond formation with neighbouring acceptor sites. Adapted or reproduced from [40–42].

the latter occurs when the photoelectron is promoted into the continuum and backscatters from neighbouring atoms, thus providing information on the local atomic coordination The techniques can be made both surface and bulk sensitive by judicious experimental configuration However, working with volatile liquids such as water proves difficult in the soft x-ray regime, with elaborate differential pumping schemes being required to transcend the problems imposed by the need to operate in vacuum [50,51]

X-ray Raman scattering is a bulk sensitive technique wherein a hard x-ray photon scatters inelastically from the sample [66] The small transfer of energy to the sample facilitates electronic excitation of core levels Thus the technique can measure absorption spectra with edge energies lying in the soft x-ray regime The technique provides the same information as classical absorption spectroscopies, is not sensitive to saturation effects intrinsic to XANES and EXAFS measurements, and can be performed in an ambient environment without the need for high vacuum Its downside is the weak scattering cross section and slightly poorer energy resolution

The traditional techniques for structural determination of liquid water are yielding diminishing returns owing to the collective efforts of many generations of researchers New results are starting to appear in the literature from alternative research fields Using femtosecond optical spectroscopy the relaxation dynamics of systems has been probed via OH stretching frequencies [67] Recent measurements have successfully determined the role water plays in the kinetics of acid-base photo-initiated proton transfer [68], the character of water molecules in the hydration shell about an anion [69] and the structure of protonated water clusters [70,71] Time resolved photoelectron spectroscopy has attempted unsuccessfully to elucidate the hydrated electron structure [72,73], whilst time-resolved electron diffraction has probed the evolution of a thin ice film following impulsive laser heating [74]

The vibrational spectroscopies infer indirect structural information by relating the OH stretching mode vibration to variations in the hydrogen bond length However, the relationship may not be one-to-one in linear vibrational absorption spectra due to broadening of the spectral bands from anharmonic coupling of low frequency modes and homogeneous broadening by the fast dephasing of coherent optical polarisations as pointed out by Elsaesser et al [75] Whilst photoelectron spectroscopy and ultrafast electron diffraction provide direct information pertaining to the chemical environment / atomic scale structure, respectively, they are surface sensitive techniques inherently unsuitable for the characterisation of bulk volatile liquids

The initial aim of our experiment was to probe in a time-resolved manner perturbations in the local aqueous structure caused by solvated proton and electron species Different dynamical effects were expected for the two systems Prototropic mobility is essentially

a random co-operative, even democratic process, where the proton hops from one water molecule to another. In contrast it is believed that the hydrated electron, surviving immediate geminate recombination, remains confined in a solvation shell defined by six equivalent water molecules octahedrally arranged as shown in Figure 1.3 (a) [76].

Proton transfer, commonly referred to as the von Grotthuss mechanism, is as much a source of debate within the literature as the structure of water itself. A precise lucid understanding of the process would have major impact on all chemistry related specialisms, with huge technological importance for areas such as fuel cell design. Numerous models have been suggested [77] with the simple "Gedank" proposal of Agmon [78], inferred from and self-consistent with available experimental data, making the most physical sense to date. After "birth", the solvated proton begins its itinerant journey from a plane-trigonal co-ordinated hydronium complex $(H_3O)^+$ embedded in an Eigen cation $(H_9O_4)^+$ as shown in Figure 1.3 (c). Dynamical fluctuations in the solvent preselect the proton's migratory path by breaking a hydrogen bond in the second co-ordination shell of the cluster. Bond breakage in the hydronium complex itself is not favoured by energy considerations. Thus the water molecule that has broken away from the Eigen cluster begins to reorient on a picosecond timescale. In the remaining protonated cluster ultrafast (femtosecond timescale) readjustment of bond configurations occurs leading to large proton polarizabilities and an intermediate Zundel $(H_5O_2)^+$ cluster as shown in Figure 1.3 (d). The proton consequently transfers to the water molecule whose second shell bond was originally broken. The water molecule from which the proton originated stabilises in a tetrahedrally co-ordinated structure by bonding with another molecule in the second solvation shell. The result is a new Eigen cation from which the process can start over. Thus the prototropic mobility is an incoherent Markovian process involving fluxional defect isomerisations between the Eigen and Zundel structures. The net result is displacement of the proton by approximately two water molecules from its starting position even though the individual atoms only move a fraction of an Ångström. The essence of the model has been confirmed by molecular dynamics simulations [79].

In contrast the bound state of the solvated electron can be formed by two photon absorption of ultraviolet light in neat water. Thus water molecules can be promoted into a highly excited state and decay via dissociative or ionisation pathways, with a respective branching ratio of 0.76 : 0.24 [80]. Dissociative decay results in the formation of hydroxyl and protonated species. For the ionisation channel recent femtosecond infrared spectroscopic measurements confirm the evolution of the solvated electron from a nascent excited state "wet" electron precursor with a lifetime of $\sim$ 500 fs [81]. Of the initial set of solvated electrons, approximately 36 % undergo geminate non-radiative recombination within 2.5 ps before reaching the Onsager radius, the distance where the Coulombic binding energy equals the thermal energy of the electron [82]. The remainder form the long lived solvated

electrons These are stabilised within a solvation shell of radius $\sim 2\,1$ Å This makes for a very interesting quantum system as the spatial extent of the electron wavefunction is comparable to the cluster dimension [83]

With this scientific motivation an experiment was designed to try and investigate photo-initiated charge transfer dynamics in aqueous solution From the foregoing discussion on experimental methods, time-resolved x-ray diffraction immediately suggests itself as a suitable technique, as transient optically induced perturbations to the hydrogen network will correspond to changes in the oxygen-oxygen radial distribution function The technique obviates the need to work in vacuum, is suitable for bulk volatile liquid samples and interpretation of data is relatively straightforward The dominant contribution to the signal will originate from intermolecular rearrangements with structure factor changes at high momentum transfer remaining relatively constant As the differential structure factor tends to zero faster than the structure factor itself, changes in the pair correlation function can be extracted from data over a limited range of momentum transfer [84] To date the technique has been successfully applied to monitor the recombination of laser-dissociated iodine molecules dissolved in CCl_4 [85] and the formation of the bridged radical $CH_2ICH_2\bullet$ in methanol [86]

In the time-resolved x-ray diffraction experiment discussed in Chapter 4 solvated electrons were created by photoionisation of neat water with femtosecond pulses of ultra-violet light Protons were injected into the liquid by single photon excitation of water doped with the photoacid pyranine The temporal resolution of the experiment was set by the intrinsic x-ray pulse duration from the Advanced Light Source (~ 100 ps) As accentuated above, the quantum efficiency for solvated electron production is quite low ($\sim 0\,15$) and significant non-radiative recombination of the solvated species occurs on picosecond timescales [81,87] Thus the dominant contribution to our excited state signal arose from temperature-induced changes associated with rearrangements of the hydrogen-bonded structure at constant volume, before the system had time to expand Unfortunately charge-transfer contributions to the signal were much weaker and could not be discerned Transient changes in the oxygen-oxygen pair correlation function were extracted and interpreted as a decrease in the local tetrahedral ordering Thus a technique to probe temperature-jump effects in liquids under arbitrary initial conditions was developed

Whilst progress was made toward the initial experimental goal, it was not possible to structurally determine the solvation shell surrounding an aqueous proton or electron However, it is worth noting that our experimental geometry is fully compatible with XFEL sources under development at present It is to be expected that repetition of the measurement in the future with the femtosecond or even attosecond temporal and Ångstrom spatial resolution offered by these sources will surely force nature to give up water's secrets, secrets that have been probed relentlessly since Rontgen's time [67] For now we

progress to the thesis proper and try to satisfy ourselves initially with the development of an ultrafast detector for a current source of femtosecond x-rays

Chapter 2

Quantum Efficiency of CsI Reflection Photocathodes

2.1 Introduction

Current femtosecond and picosecond time resolved studies of structural and electronic dynamics are limited by the intensity of the x-ray sources [88, 89] Consequently the quantum efficiency of the detector is a key experiment parameter X-ray streak cameras operating under normal incidence excitation in a transmission geometry, whilst demonstrating high time resolution, have had a low quantum efficiency, between 0 1 and 10 % [28] A streak camera can posess unit quantum efficiency when the photocathode is in a grazing incidence geometry and the incidence angle of the x-rays is chosen such that the x-ray penetration depth (measured perpendicular to the surface) matches the secondary electron escape depth By sweeping perpendicular to the plane of the incident x-rays and cathode normal, it should be possible to achieve temporal resolution comparable to normal incidence cameras Tilting of the swept image due to dispersive excitation of the cathode can be easily compensated for in the data analysis

To date, most work in the literature pertaining to the quantum efficiency of detector materials examines what is termed the total electron yield (TEY) i e the average number of electrons produced per incident photon This quantity does not directly reflect the number of photons that effectively interacted with the sample in the production of electrons For low intensity measurements, the pulsed quantum efficiency (PQE), defined as the probability of obtaining a cluster of any number of electrons per incident photon, is a more relevant parameter For example, obtaining 2,0,4,1,2 electrons per photon in a particular time interval would yield a TEY = 9/5 and a PQE = 4/5 However, inherent in the emission process is a probability distribution of the number of electrons emitted, which is an intrinsic noise source The detective quantum efficiency (DQE) is a measure of the overall system efficiency It incorporates the additional noise imparted by the detection process i e the effect of the pulse height distribution on the pulsed quantum efficiency The DQE provides the most relevant description of the photocathode efficiency

CsI is typically the photoconverter chosen for use in the ultraviolet to x-ray region of the

13

electromagnetic spectrum. Being an alkali halide it is an excellent secondary electron emitter with a narrow secondary electron distribution curve and a high quantum yield. Extensive experimental and theoretical investigations have been performed to understand the photoemissive characteristics of this material. The early work of Henke *et al.* [90, 91] focused on analysis of the energy distribution and yield of secondary electrons. Henke described the secondary electron transport in terms of a one dimensional random walk. Collective excitation effects are not treated in this model and thus the plasmon shoulder evident in the secondary electron energy distribution curve is not accounted for in his model. Henke used the angular dependence of the primary photoelectron yield to determine the photon absorption coefficient and mean free path of the photoelectron [92].

Fraser developed a relatively simple model that accurately predicted the photoelectric yields in x-ray photocathodes [29, 30]. This work examined the phenomena of pulsed quantum efficiency and total yield as a function of the photon incidence angle and energy. Close agreement was found between the model and the limited experimental data set that was available [93]. Fraser's model describes the generation of secondary electrons, their transport and emission processes in terms of average parameters for the secondary electron creation energy and the inelastic mean free path. All information pertaining to the bandstructure of the sample and its influence on the photoelectron generation and subsequent secondary electron transport processes are lost in this model.

The Monte Carlo simulation performed by Akkerman *et al.* [94, 95] is the most complete model of secondary electron emission in CsI to date. This microscopic model deals with the processes of photon absorption and electron transport, including electron interactions with acoustic and longitudinal optical phonons [96], elastic scattering and emission [97]. Consequently a theoretically more accurate analysis of the electron inelastic mean free path, stopping power [98, 99] and spatial characteristics of the electron cascade [100] has been obtained. This work has been complimented where possible by experimental investigations by the authors [101, 102]. Exchange and correlation effects are not treated in this model: the first order Born approximation is used in the treatment of the differential inelastic mean free path of the valence electrons. The significance of pulsed quantum efficiency for detectors is discussed and the model is compared with data in the hard x-ray regime as a function of sample thickness for a transmission geometry [103].

In this chapter we characterize the total electron yield, pulsed quantum efficiency and detective quantum efficiency of CsI as a function of the incident photon energy, angle of incidence and the anode-photocathode electric field in the soft x-ray energy range 100 eV to 1 keV. The results discussed in this chapter can be extended to the hard x-ray regime. The total electron yield is obtained by measuring the electron current for a given photon flux; whilst the pulsed quantum efficiency is measured by counting electron bunches using an electron multiplier. For energies where the x-ray penetration depth is greater than the

secondary electron escape depth, the yields increase as the cosecant of the incident angle
A small increase in the total electron yield with increasing electric field is observed This
is explained in terms of a reduction of the cathode electron affinity No significant field
dependence is observed in the pulsed quantum efficiency measurements as the escape
probability of an electron in a batch does not change appreciably Assuming a binomial
probability distribution for the electron emission process, we examine the detective quan-
tum efficiency by Monte Carlo simulation The results show greater efficiency at grazing
angle

2.2 Theory

In this section we quickly summarize the salient features of Fraser's model [29] as it is
pertinent to interpretation of the results and the subsequent discussion For the energy
range examined in this chapter (100 eV to 1 keV), Henke [91] has shown experimentally
that the primary electron contribution to the total electron yield in CsI is less than 0 4
% This has also been confirmed by our retarding field measurements of the secondary
electron distribution (see Section 2 3) Thus, for the energy range discussed in this chapter
the primary electron contribution to all yields is neglected Incidentally for streak camera
applications, the primary electron contribution from the photocathode does not effect the
measurement These electrons, posessing kinetic energy far greater than the secondary
electrons, are not imaged in the detector plane by the camera electron optics For energies
below the CsI L-edges, fluorescent decay of the core hole is negligible [30]

The probability of an X-ray photon possessing energy E_γ, striking a photocathode of
thickness T, at an angle α with respect to the surface, being absorbed in a layer dz at a
depth z below the surface is

$$P_\gamma = [1 - R(\alpha)]\, \mu \csc \alpha' \exp\left(-\mu z \csc \alpha'\right) dz \quad , \qquad (2\ 1)$$

where μ is the energy dependent linear absorption coefficient, $R(\alpha)$ is the Fresnel re-
flectivity coefficient and α' is the angle the refracted x-ray makes with respect to the
photocathode surface Assuming an energy ε is required to promote a single secondary
electron from the valence band with sufficient kinetic energy to escape the sample implies
the number of electrons generated within this layer dz is

$$dN(z) = E_\gamma \varepsilon^{-1} [1 - R(\alpha)]\, \mu \csc \alpha' \exp\left(-\mu z \csc \alpha'\right) dz \qquad (2\ 2)$$

15

Assuming an escape probability for the electron generated at a depth z of the form

$$P(z) = P_s(0) \exp -z/L_s \quad , \tag{2 3}$$

where L_s and $P_s(0)$ are average values for the mean free path of the secondary electron and its escape probability at the surface respectively, yields an expression for the total electron yield

$$Y_s = E_\gamma \varepsilon^{-1} \mu \csc \alpha' \left[1 - R(\alpha)\right] P_s(0) \int_0^T \exp -z \left(\mu \csc \alpha' + L_s^{-1}\right) dz \tag{2 4}$$

To obtain an expression for the pulsed quantum efficiency we note that the probability of generating a batch of electrons between z and $z + dz$ is simply the probability of photon absorption within this layer, P_γ The probability of escape for a single electron in the bunch is given by Equation (2 3) The probability that this electron does not escape is $1 - P(z)$ Therefore, the probability that no electrons generated in the batch escape is $[1 - P(z)]^{dN(z)}$ Hence, the probability that a batch of secondary electrons escapes from a depth between z and $z + dz$ is

$$P_b(z) = 1 - [1 - P(z)]^{dN(z)} \tag{2 5}$$

Hence we obtain an expression for the pulsed quantum efficiency of the material based on the photon absorption and secondary electron batch escape probabilities

$$Y_p = [1 - R(\alpha)] \mu \csc \alpha' \int_0^T \exp \left(-\mu z \csc \alpha'\right) \left\{1 - [1 - P(z)]^{dN(z)}\right\} dz \tag{2 6}$$

The probability of n secondary electrons emerging into the vacuum out of the $N = E_\gamma \varepsilon^{-1}$ electrons produced at depth z can be calculated assuming a binomial probability distribution [104, 105]

$$T(n) = \frac{N!}{(N - n)! n!} \left[P_s(0) \exp -z/L_s\right]^n \left[1 - P_s(0) \exp -z/L_s\right]^{N-n} \tag{2 7}$$

and the probability for photon absorption within the layer i e Equation (2 1) above Thus, the escape probability for a batch possessing one or more electrons is

$$P(n \quad n \geq 1) = [1 - R(\alpha)] \mu \csc \alpha' \frac{N!}{(N - n)! n!} \times$$
$$\int_0^t \exp \left(-\mu z \csc \alpha'\right) \left[P_s(0) \exp -z/L_s\right]^n \left[1 - P_s(0) \exp -z/L_s\right]^{N-n} dz \tag{2 8}$$

16

The average number of electrons in a batch is given by

$$\bar{n} = \sum_{n=1}^{\infty} n \frac{P(n)}{1 - P(0)} \quad , \tag{2 9}$$

where the probability of zero electron emission, $P(0)$, is calculated from $1 - Y_p$ at the experimental point of interest

The detective quantum efficiency which the encompasses the additional noise imparted through the detection process is defined as

$$Y_d = \frac{(SNR_o)^2}{(SNR_i)^2} \quad , \tag{2 10}$$

where SNR_o and SNR_i are the signal to noise ratios at the output and input of the detector, respectively From the pulse height distribution, $P(n \quad n \geq 1)$, the detective quantum efficiency can be determined by the relation [106]

$$Y_d = \frac{Y_p}{1 + \left(\frac{\sigma}{\bar{n}}\right)^2} \quad , \tag{2 11}$$

where σ is the standard deviation and $\bar{n}$ the mean

Values for $R(\alpha)$ and μ were calculated using the Henke tables [107] A secondary electron escape energy $\varepsilon = 7$ eV was calculated on the basis of the electron affinity and bandgap energy of CsI, assuming all electrons possessed the peak energy of the secondary electron energy distribution curve Negligible energy losses during transport were assumed A secondary electron mean free path $L_s = 215$ Å and the values of $P_s(0)$ listed in Table 2 1 were used for modelling the experimental data These values are consistent with those cited in the literature [30, 91, 96] The detective quantum efficiency was determined by Monte Carlo simulation 10^5 trials were run for each point yielding a simulation error less than 1 %

E (eV)	$P_s(0)$
100	0 3
500	0 18
1000	0 24

Table 2 1 Values of $P_s(0)$ used in modelling the experimental data

17

2.3 Experimental Method

All measurements were performed at beamline 6 3 2 at the Advanced Light Source [108] For the total electron yield and pulsed quantum efficiency measurements the apparatus was setup on a θ–2θ goniometer in the reflectometer chamber Typical chamber vacuum pressure was 10^{-8} Torr Photon energies of 100 eV, 500 eV and 1000 eV were used High orders from the monochromator were suppressed by three mirrors and by filters

The apparatus for the total yield measurement is shown in Figure 2 1 on page 19 Incident x-ray photons passed through a 1 mm slot in the anode and struck a 1000 Å thick CsI photocathode deposited on an aluminum blank by the Luxel Corporation The size of the beam striking the cathode was approximately 50 μm $\times$ 100 μm The resulting primary and secondary electrons were accelerated toward the anode by the electric field that was normal to both the anode and cathode surfaces The cathode was rotated by $10°$ with respect to the incident beam about the y-axis (angle χ in Figure 2 1), ensuring all electrons were collected by the anode Thus no electrons could escape through the anode slot as occurs in a conventional streak camera The electric field was varied between 100 V/mm and 10 kV/mm For a given photon energy and electric field, the experimental stage was rotated about $0° \leq \theta \leq 90°$ Due to the tilt of the cathode about the y-axis with respect to the incident beam this corresponds to an actual rotation from $0° \leq \theta \leq 80°$ The electron yield current was recorded using a current amplifier attached to a computer The incident photon flux was measured using a GaAsP/Au Schottky diode [109] traceable to NIST The total electron yield was obtained by division of these two measurements The secondary electron energy distribution was determined by the retarding field method wherein a positive retarding potential was applied to the cathode

For the pulsed quantum efficiency measurements, the apparatus shown in Figure 2 2 on page 20 was used During multibunch operation mode, subsequent buckets are separated by 2 ns in the storage ring The incident photon flux was attenuated such that approximately one photon every microsecond was incident on the sample The number of photons incident on the sample per second was approximately 0 2 % of the multibunch rate i e a single photon was incident on the sample at a given time This is lower than the maximum operation frequency of the bunch detection electronics (50 MHz) The probability of two or more photons striking the cathode was negligible The electron bunch generated by the incident photon was accelerated towards the channeltron electron multiplier by the electric field between the cathode and a 90 % transparent gold mesh on the anode The channeltron output pulse was capacitively coupled to a constant fraction discriminator operating in threshold mode to eliminate background noise The number of output pulses per second from the discriminator were counted using a personal computer The electric field was varied between 100 V/mm and 1 kV/mm The kinetic energy of the electrons
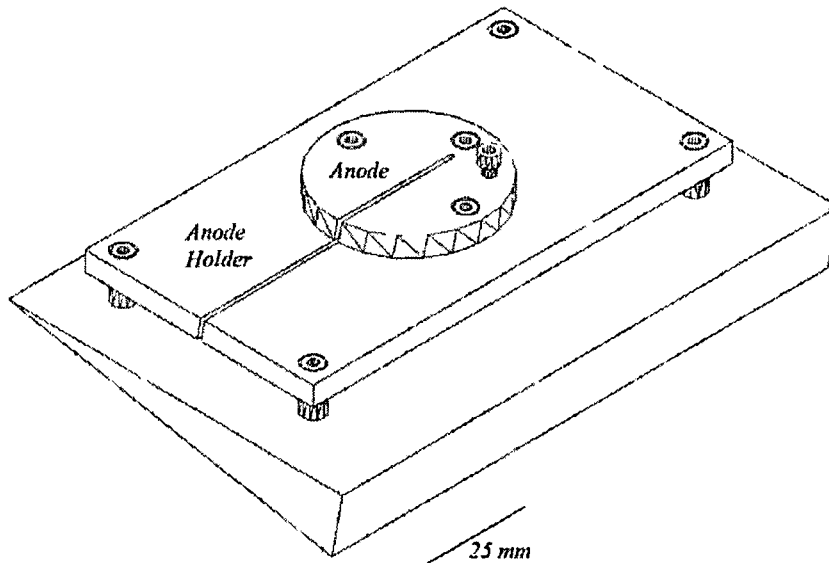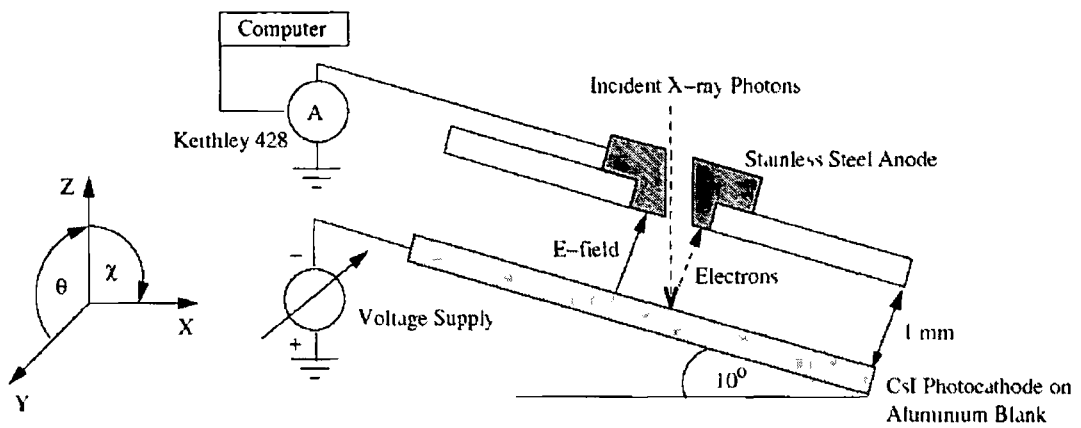
Figure 2 1 Experimental setup used to measure the total electron yield Top electrical system Bottom perspective view of the electron collection assembly

striking the channeltron varied between 100 eV and 1 keV depending on the electric field used The efficiency of the channeltron was greater than 80 % for this energy range [110] For a given electric field and photon energy, the experimental stage was rotated about $0° \leq \theta \leq 90°$ Due to the 45° tilt of the cathode with respect to the incident beam this corresponds to an actual rotation from $0° \leq \theta \leq 45°$ The angular dependence of the photon attenuation by the mesh was accounted for by measuring the mesh transmission with a diode situated in the cathode position The pulsed quantum efficiency was obtained by dividing the number of electron bunches detected per second by the number of photons per second incident on the cathode

19
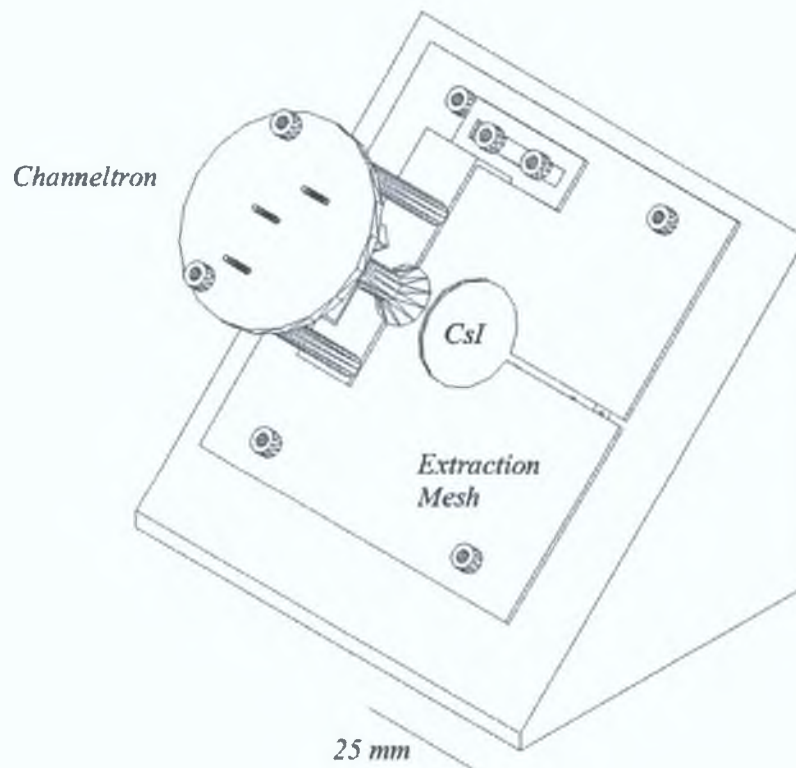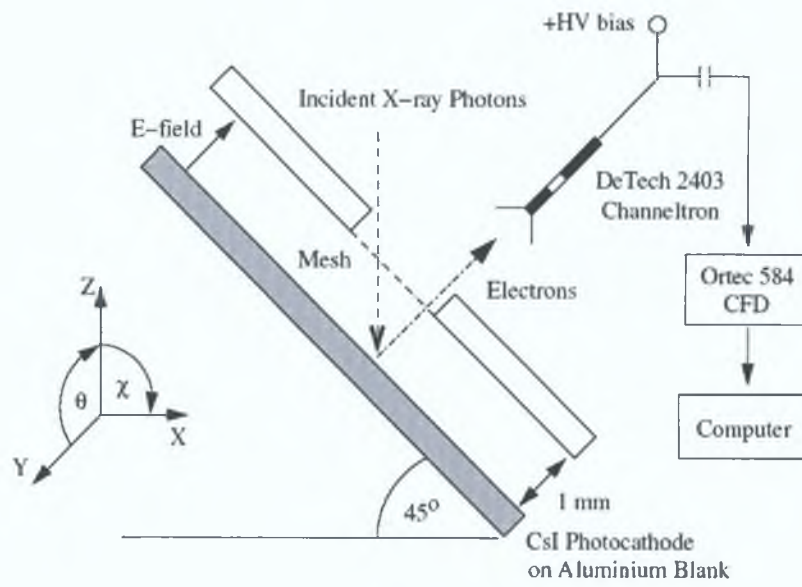
Figure 2.2: Experimental setup used to measure the pulsed quantum efficiency. Top: electrical system. Bottom: perspective view of the electron collection assembly.

2.4   Results and Discussion

The secondary electron energy distribution curve (EDC) of CsI is shown in Figure 2.3. 1 keV photons were used as the excitation source. The retarding field method measures the component of the energy which is normal to the surface [111]. A FWHM for the secondary electron EDC of 1.5 eV along with evidence of the plasmon shoulder is found to be in close agreement with the literature [90, 91]. A negligible contribution to the yield was observed for retarding fields greater than 10 V indicating the electron yield is primarily due to low energy secondary electrons.
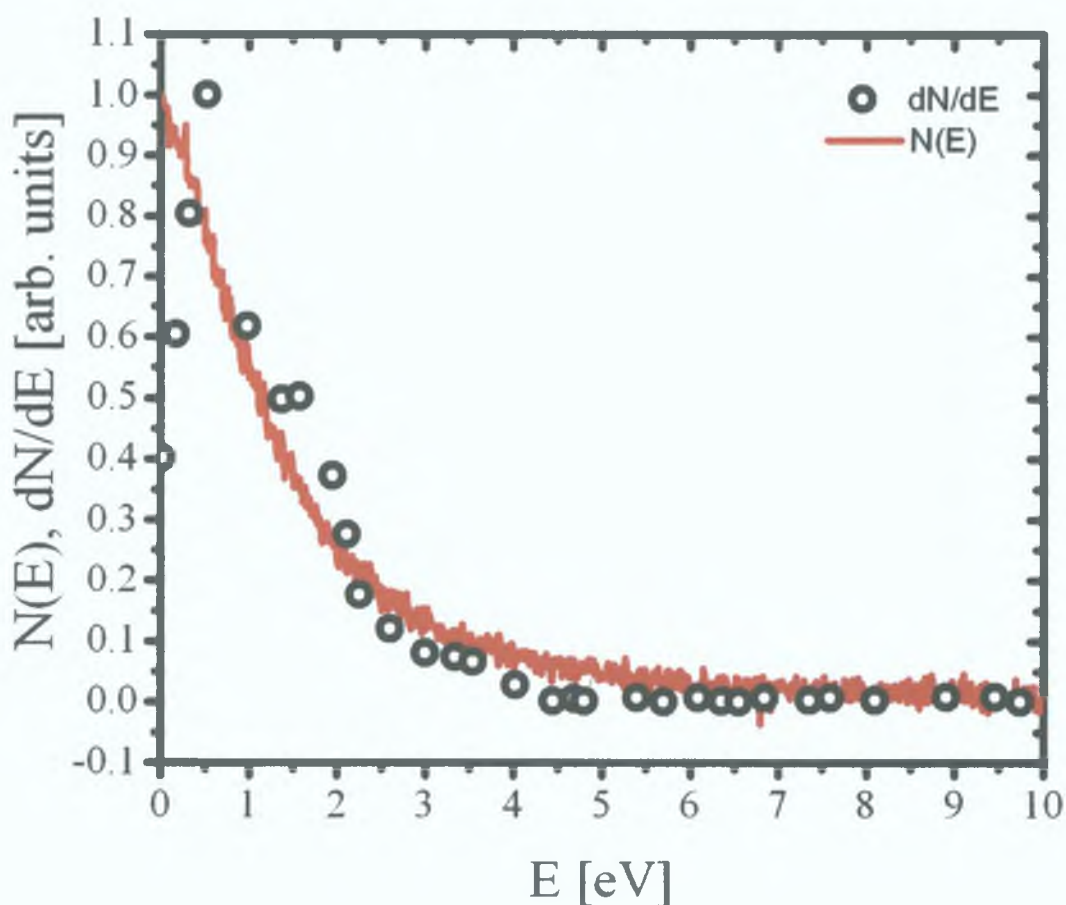
Figure 2.3: Secondary electron distribution curve of CsI. The integral distribution $N(E)$ is shown as the solid curve and the differential distribution dN/dE is shown as circles.

The measured total electron yield as a function of angle of incidence is shown in Figure 2.4 for 100 eV incident photons with an anode-cathode field $F = 1$ kV/mm. A near constant yield is obtained above 15°. The x-ray penetration depth varies from 6.5 nm at 15° to 20 nm at normal incidence. The shallow x-ray penetration depth is due to the strong absorption associated with the $4d - \epsilon f$ transitions in the Cs^+ and I^- ions [112]. Based on the secondary electron distribution curve and Monte Carlo simulations [97] of the

escape probability for secondary electrons, one can conclude that the x-rays are exciting secondary electrons from a region shallower than the secondary electron mean free path. Henke defines this escape depth to be 25 nm over the energy range of interest [90]. Below 15° the total yield decreases due to increased reflectivity from the cathode.
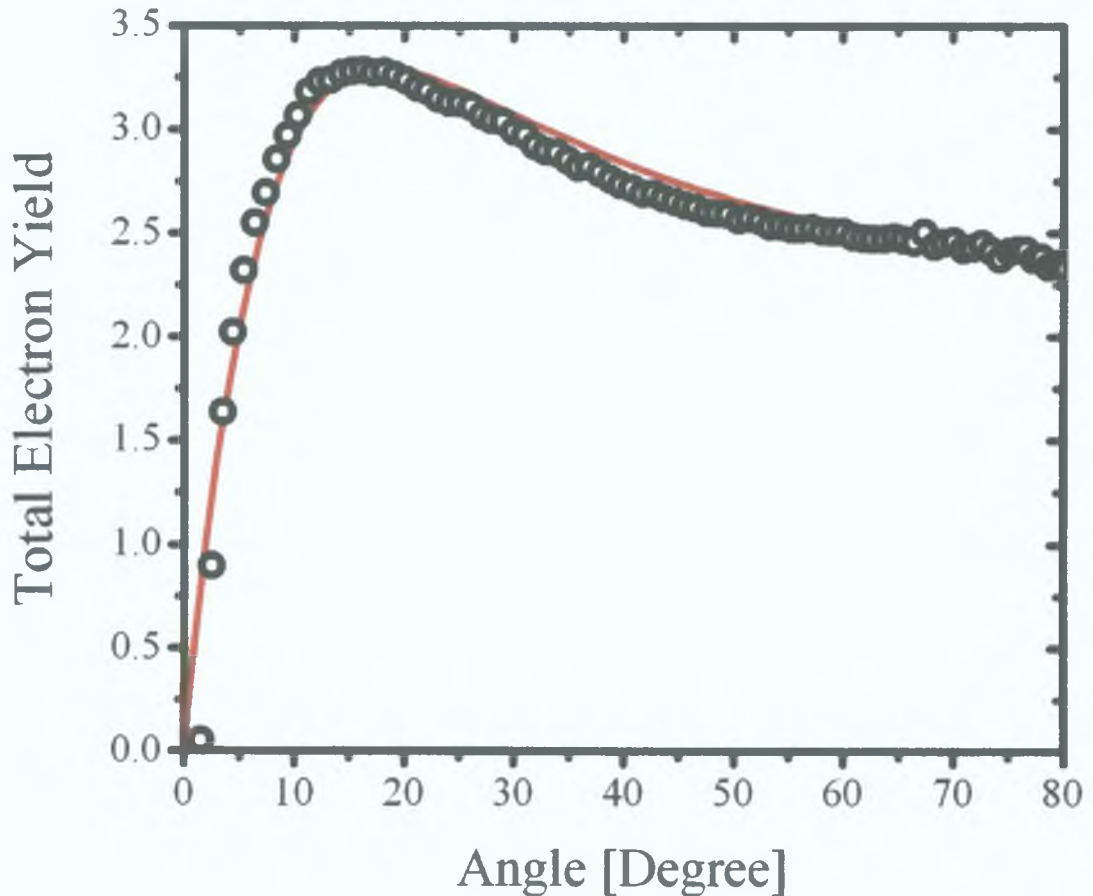
Figure 2.4: Total electron yield from 1000 Å thick CsI photocathode excited by 100 eV photons. $F = 1 \, kV/mm$. The solid line was calculated using Fraser's model.

For the case where the x-ray penetration depth is greater than the secondary electron escape depth, the total yield increases with the cosecant of the incidence angle as shown for 500 eV and 1 keV photons in Figures 2.5 (a) and (b) on page 23, respectively. At normal incidence the total yield at 500 eV is less than the yield at 100 eV. The 500 eV and 1 keV photons penetrate deeper into the cathode than the secondary electron escape depth before being absorbed and thus detection efficiency of the electrons created is reduced. At grazing incidence wherein the photon penetration depth is matched with the secondary electron escape depth, the number of secondary electrons created within a mean free path of the surface has increased due to the greater energy of the initial 500 eV and 1 keV photoelectron compared to the 100 eV case. Henke has shown that the total yield as a function of energy is proportional to the product of the photon energy and the linear absorption coefficient [91].
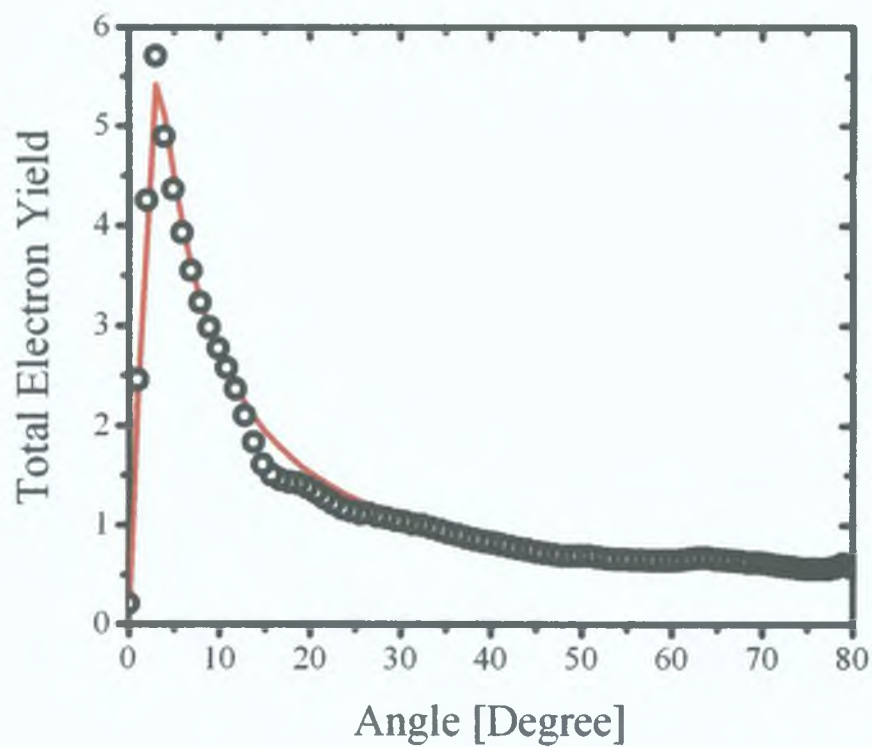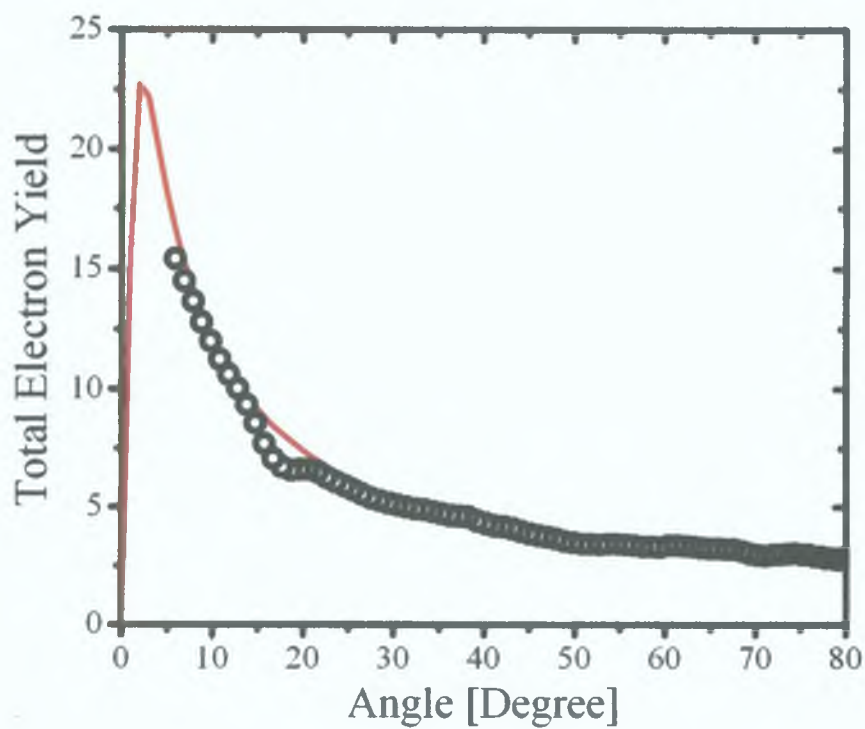
Figure 2.5: Total electron yield from 1000 Å thick CsI photocathode excited by (a) 500 eV and (b) 1 keV photons. $F = 1$ kV/mm. The solid lines were calculated using Fraser's model.

The increase in total yield with increasing electric field has been modeled by a reduction in the electron affinity. Through momentum and energy conservation of the escaping electron, Henke has shown that the secondary electron yield in the case of insulators is inversely proportional to the electron affinity [90]. Buzulutskov *et. al* [113] have modelled the reduction in the electron affinity, and subsequent increase in yield, by considering that electrons in the insulator interact with their image charge in a manner similar to Schottky barrier lowering in metals. The field-induced reduction in the electron affinity can be expressed as

$$\Delta E_a = \sqrt{\frac{\alpha e F}{4\pi\epsilon}}; \qquad \alpha = \frac{\epsilon_\infty - 1}{\epsilon_\infty + 1} \quad , \tag{2.12}$$

where e is the electron charge, F is the electric field strength, $\epsilon_\infty = 2.69$ is the high-frequency dielectric constant and ϵ is the permittivity of CsI. Figure 2.6 shows the total electron yield as a function of electric field for 100 eV, 500 eV and 1 keV photons. A slow increase in total electron yield with increasing electric field is observed.
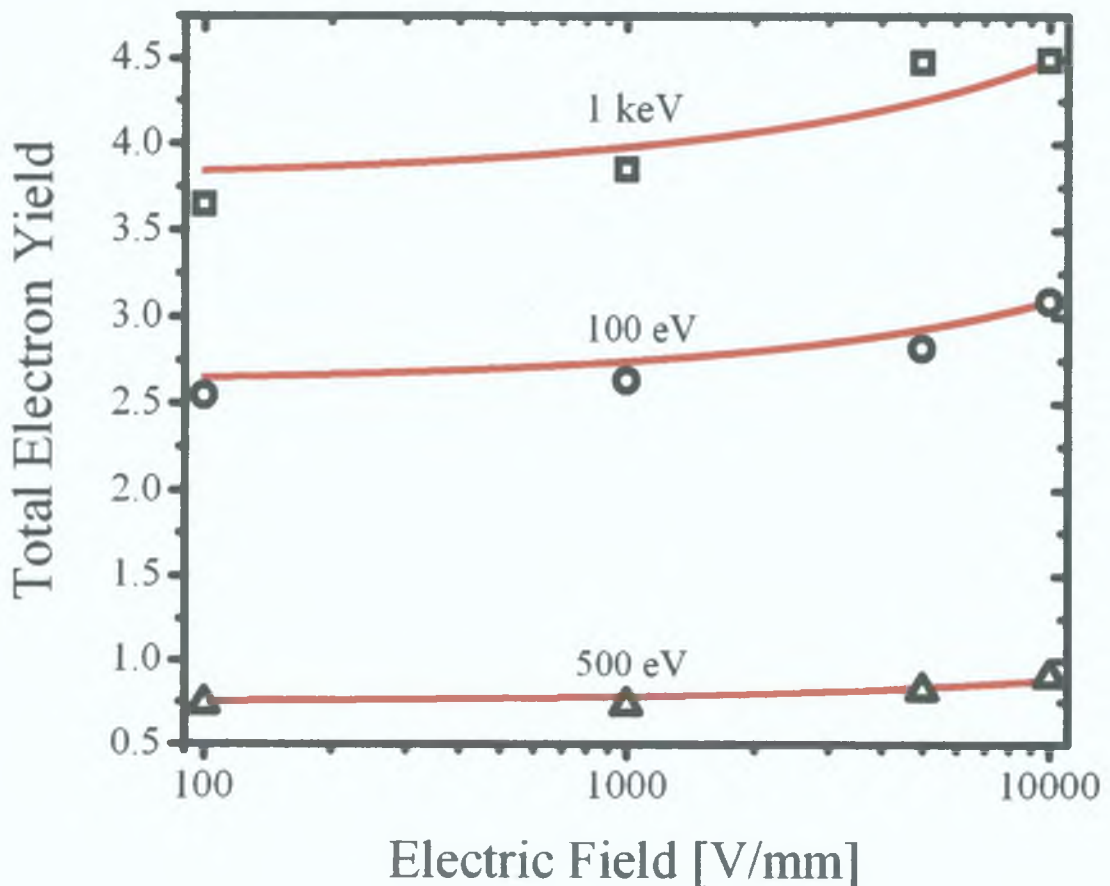
Figure 2.6: Total electron yield dependence on electric field at an incidence angle of 45°. The solid lines were calculated using Fraser's model incorporating the field dependent electron affinity.

The pulsed quantum efficiency of CsI at 500 eV and 1 keV for an electric field $F = 1$

kV/mm is shown in Figures 2.7 (a) and (b) on page 26, respectively. When the photocathode is excited by 1 keV photons it is possible to achieve unit pulsed quantum efficiency at an incidence angle of 3°. For 500 eV photons the photocathode reflectivity increases faster than the decrease in the x-ray penetration depth. Still a maximum pulsed quantum efficiency of 90 % is achieved.

The increase of the pulsed quantum efficiency with decreasing incidence angle is less dramatic than that shown in the total electron yield data. In contrast to the total electron yield measurement, the pulsed quantum efficiency is insensitive to the number of electrons produced at a depth z in the sample, provided one electron is detected. This is couched inside the integrals of Equations (2.4) and (2.6) in Section 2.2. Indicative probability distributions of n electron emission $P(n)$ for 500 eV photons incident on a 1000 Å CsI photocathode at 45° and 5° are shown in Figure 2.8 on page 27. The average number of electrons per batch $\bar{n} = 3$ and 8.5 for 500 eV and 1 keV photons incident on the sample at 45°, respectively. This increases to $\bar{n} = 4.8$ and 17.4 at 5° for the respective energies. Whilst the total electron yield is dependent on the total number of electrons emitted, the pulsed quantum efficiency only depends on the number of batches emitted. The latter increases more slowly than the former and thus, the increase of the pulsed quantum efficiency with decreasing incidence angle is slower than the total electron yield.

Although the electric field modifies the surface potential of the cathode and increases the probability of escape for individual electrons no significant increase in the pulsed quantum efficiency is seen with increasing field. The reduction in the electron affinity only leads to an increase in the number of electrons emitted per bunch, not the number of bunches emitted. Analysis of the pulse height distribution has shown that on average more than one electron per bunch is emitted and thus no significant field effect in the pulsed quantum efficiency is experimentally observed.

Using the values of $P_s(0)$ and L_s employed in modelling the experimental data, the detective quantum efficiency has been evaluated at 500 eV and 1 keV (Figure 2.7) by Monte Carlo simulation. A maximum detective quantum efficiency of 58 % at 4° and 83 % at 3° is achieved for 500 eV and 1 keV photons, respectively. Comparison with the pulsed quantum efficiency shows that the distribution in the number of electrons emitted in a batch reduces the effective efficiency of the photocathode. However, the data clearly shows that it is preferable to operate in a grazing incidence regime. The pulse height distribution adds more statistical uncertainty at larger incidence angle as the ratio of the standard deviation to the mean of the distribution is reduced at grazing incidence. This change in the statistical uncertainty with grazing angle is reflected in the representative pulse height distribution shown in Figure 2.8. The ratio of the standard deviation to the mean is larger at an incidence angle of 45° than at 5°.
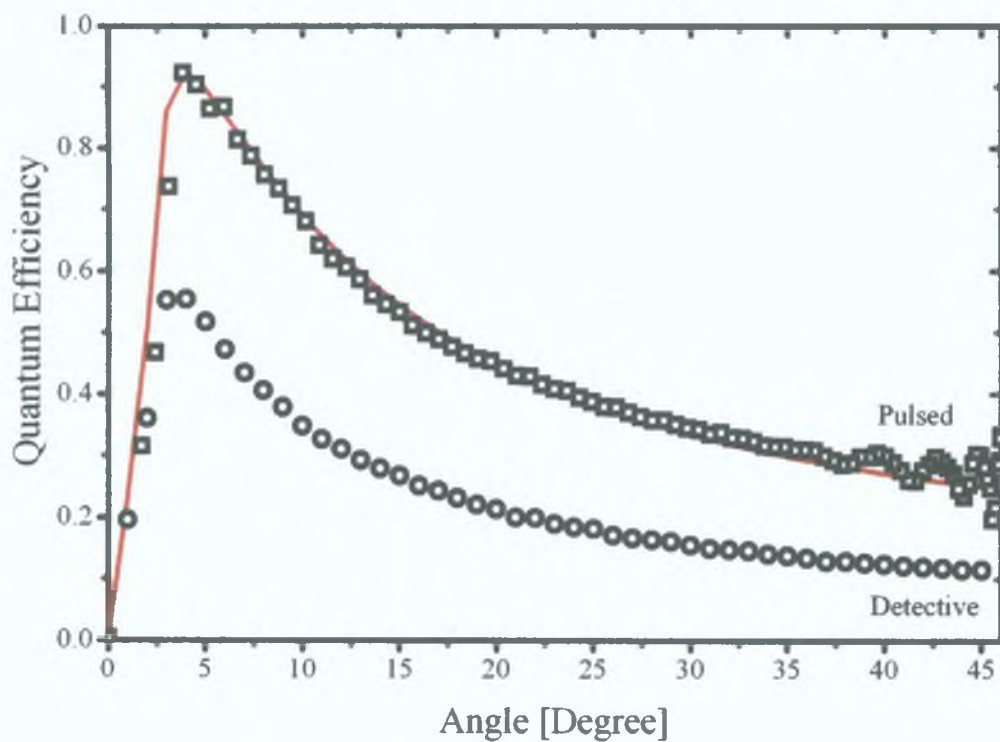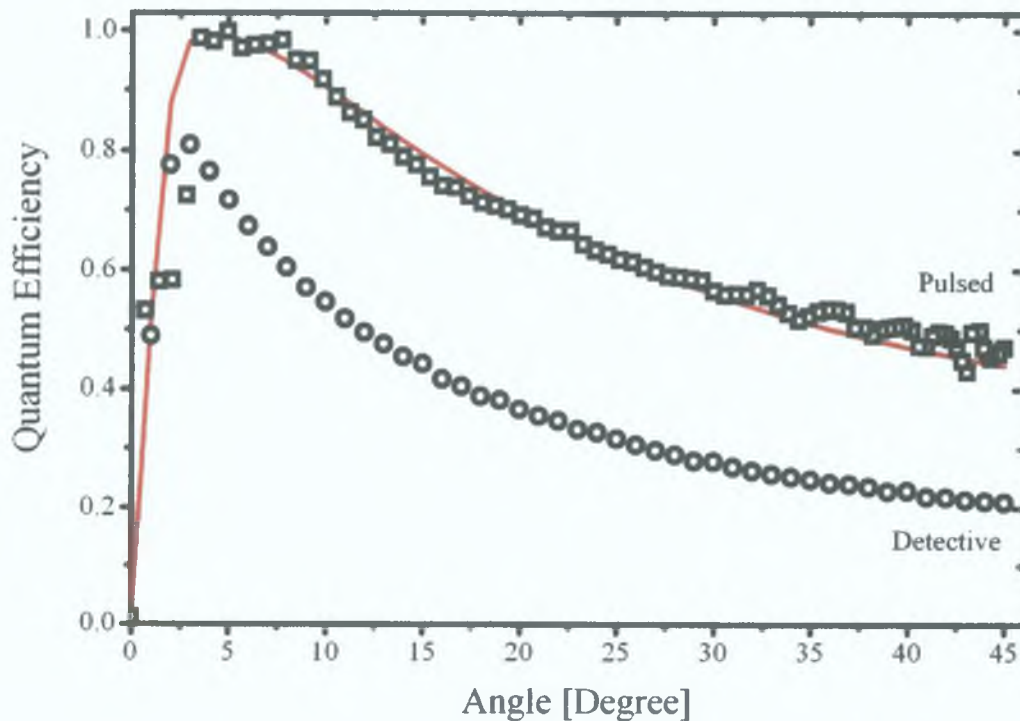
Figure 2.7: Pulsed quantum efficiency and detective quantum efficiency of a 1000 Å thick CsI photocathode excited by (a) 500 eV and (b) 1 keV photons. The theoretical pulsed quantum efficiency (solid lines) were calculated analytically using Fraser's model and the detective quantum efficiency was calculated by Monte Carlo simulation.
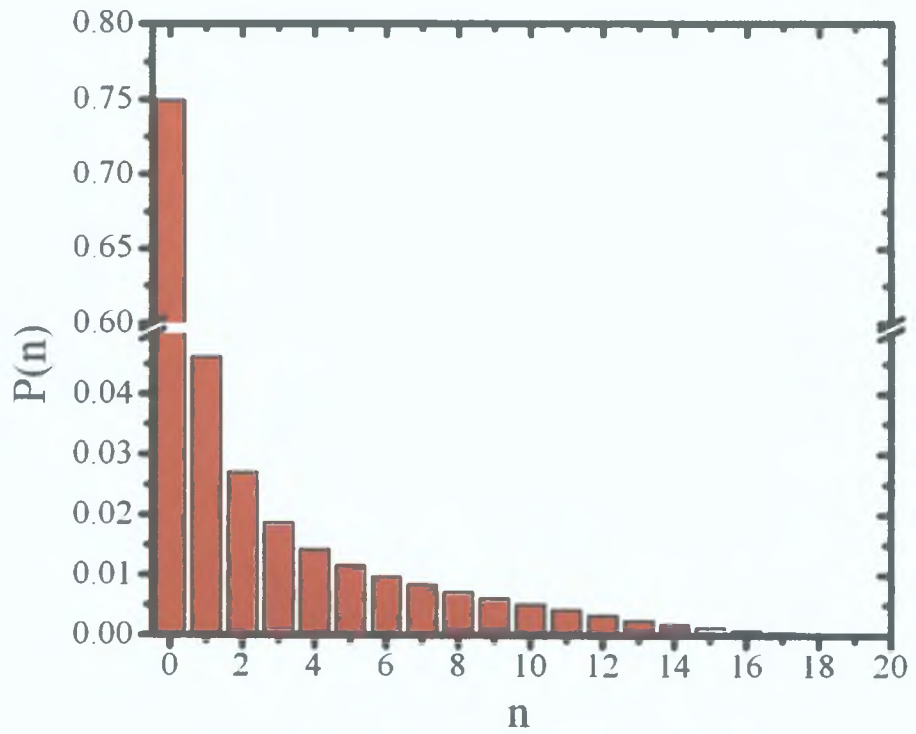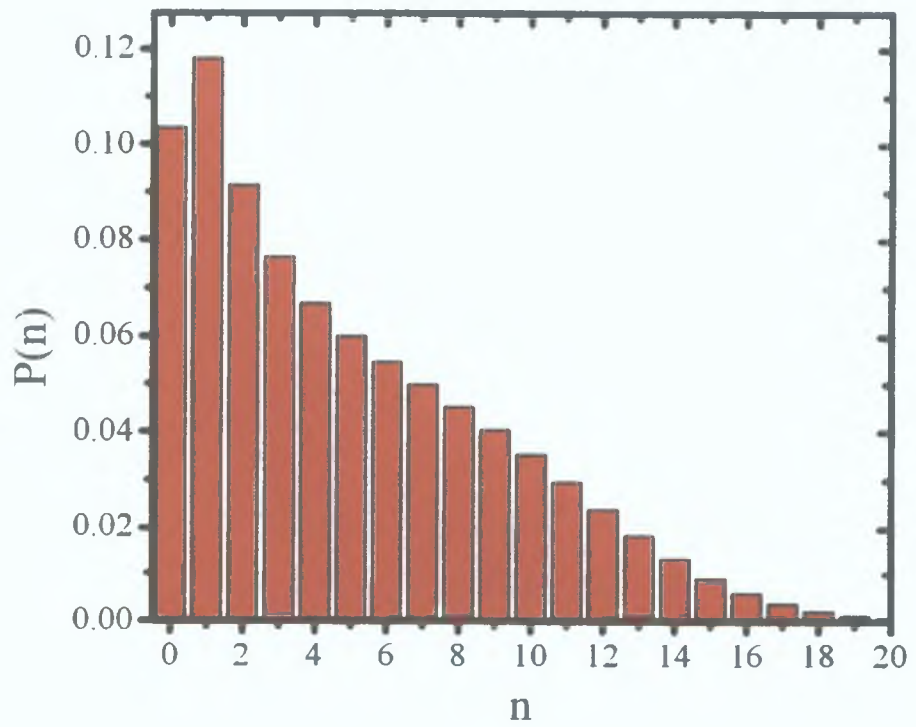
Figure 2.8: Calculated probability distribution of n electron emission for a 1000 Å CsI photocathode excited by 500 eV photons incident at (a) 45° and (b) 5°.

The theory outlined in Section 2 2 can be easily adapted to the case of transmission cathodes [114] Comparison of the detective quantum efficiency for transmission and reflection geometries shows that at 500 eV for example, exciting a 1000 Å thick CsI photocathode at 4° in the reflection geometry is approximately 11 times more efficient than its normal incidence transmission counterpart Also it is worth noting for intensity limited applications, that the mean number of electrons per batch emitted in the reflection case is greater than the transmission case In principle, one can optimize the thickness of the transmission cathode to improve its performance but our analysis has shown that the reflection cathode is always more efficient

The results presented here may also be extrapolated to the hard x-ray regime For example, at 8 keV using a 1000 Å thick CsI photocathode, a 17 fold increase in the normal incidence pulsed quantum efficiency is obtained by exciting the cathode at 3°

2.5 Conclusion

CsI photocathodes have been characterized in a reflection geometry with soft x-rays An increase in the total electron yield, pulsed quantum efficiency and detective quantum efficiency was observed with decreasing incidence angle Unity pulsed quantum efficiency has been demonstrated at 1 keV photon energy and near unity efficiency with 500 eV photons The increase with electric field in the total yield data can be explained through a reduction in the electron affinity An excellent agreement between Fraser's model and experimental data has been obtained Our theoretical analysis has shown that reflection cathodes excited in a grazing incidence geometry are more suitable than normal incidence transmission cathodes in streak camera applications coupled to low intensity sources

Acknowledgments

Chapter 3

Development of an Ultrafast Grazing Incidence X-ray Streak Camera

3.1 Introduction

Recently a novel technique for producing femtosecond pulses of synchrotron radiation has been developed at the Advanced Light Source (ALS), Lawrence Berkeley National Laboratory Commonly referred to as the "slicing" technique, first proposed in 1996 by Zholents and Zolotorev [19] and realised in 2000 by Schoenlein et al [20], the scheme employs a high power femtosecond laser system to modulate an electron bunch within a synchrotron storage ring The energy modulated electrons, with duration comparable to the laser pulse duration ($\sim$100 fs), are spatially separated from the main $\sim$100 ps electron bunch The electron bunch is passed through a dispersive region of the storage ring and the resulting synchrotron radiation consists of a sliced femtosecond pulse spatially separated from the intrinsic picosecond synchrotron pulse Physical aperturing of the synchrotron radiation can help discriminate sliced photons from the unsliced background A schematic of the laser slicing method is shown in Figure 3 1 The streak camera described in this chapter was designed specifically for the slicing beamline at the ALS
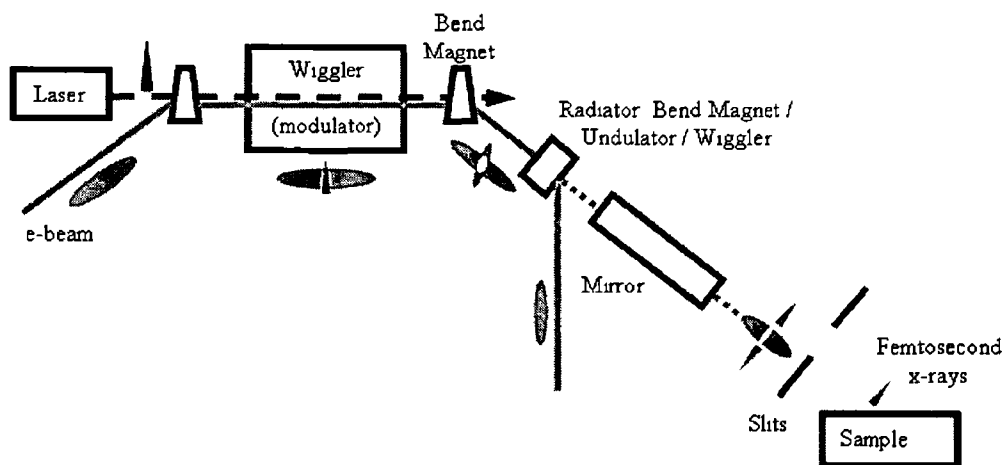
Figure 3 1   Schematic of the laser slicing method to generate femtosecond pulses of synchrotron radiation

29

The slicing technique has a number of advantages that make it a unique tool for the ultrafast scientist The optical pump pulse used to excite the sample under investigation is derived from the laser beam used for modulating the electron bunch Thus, the pump and probe beams are completely synchronised with respect to one another The source has a broad tunable spectrum extending from the infrared to hard x-ray regime Therefore one can perform classical synchrotron measurements such as diffraction and absorption spectroscopy albeit on a femtosecond timescale An inherent by-product of the slicing scheme is the production of coherent synchrotron radiation in the Terahertz region [115, 116] Essentially, the femtosecond modulation of the electron bunch in the temporal domain corresponds to spatial alterations in the electron bunch longitudinal distribution with very short characteristic length As the wavelength of the Terahertz synchrotron radiation is comparable to this longitudinal spatial distribution, the radiation from multiple electrons adds coherently This radiation is employed as an optimisation monitor for the slicing process

For all its utility, slicing is not without an Achilles heel Slicing is an inherently inefficient process Only a fraction of the electrons within the bunch possess the requisite phase to interact with the laser beam, the laser pulse duration is significantly shorter than that of the paternal electron bunch and the repetition rate of the laser is orders of magnitude lower than the synchrotron Process efficiencies on the order of 10^{-9} to 10^{-10} are typical Thus, for a typical third generation synchrotron soft x-ray beamline producing 10^{15} photons per second in 0 1% bandwidth, one could expect a slicing yield of 10^6 photons per second in the same bandwidth For photon intensive measurements such as time-resolved near edge x-ray absorption spectroscopy (XANES) it quickly becomes apparent that one must strive to maximise detection efficiency to achieve realistic integration times For example, in a recent femtosecond NEXAFS measurement of electron dynamics in VO_2 a detector incorporating a grazing incidence CsI photocathode was employed [10] The detector whose design is intimately linked to the pulsed quantum efficiency experimental setup shown in Figure 2 2 on page 20 provided near unit detection efficiency, offering a significant improvement in the signal to noise ratio over a conventional avalanche photodiode

The aperturing slits that pass the sliced photons also pass background scatter from the beamline optics associated with the picosecond pulse For an integrating detector such as an x-ray avalanche photodiode whose response time is typically a few nanoseconds, it is challenging to seperate the femtosecond photons from the picosecond background Thus, the signal which is already quite weak, suffers further degradation However, if a detector with temporal resolution on the order of a picosecond is used one can readily discriminate the sliced photons from the co-propagating ~100 ps background scatter An x-ray streak camera is such a detector As highlighted in chapter 2, an x-ray streak camera operating in a grazing incidence geometry can achieve unit or near-unit quantum efficiency without

30

compromising temporal resolution For an x-ray streak camera with ∼ 1 ps instrument resolution, one could expect an increase in the sliced signal to background by a factor of ∼ 70 compared to a conventional integrating detector A further signal increase can be anticipated through the enhanced detection efficiency offered by the grazing incidence geometry The camera itself fills a temporal niche between the truly ultrafast measurements requiring slicing and those with relatively slow dynamics that can be probed with the intrinsic pulse duration of the ALS (70 ps) Thus, the ability to detect sliced photons and having an x-ray detector possessing picosecond temporal resolution are equal motivations for the streak camera With the addition of the streak camera to the slicing program one can probe all timescales greater than 100 fs in a self contained experimental setup

In this chapter we outline the specific operational requirements of the streak camera to be used at the dedicated slicing beamline under construction at the ALS Whilst the discussion is specific, generalised extrapolations to other synchrotron beamlines and differing experimental geometries should be straightforward A design utilising analytical and simulation paradigms is discussed Analytically we predict operational parameters such as the sweep speed and temporal resolution We present a full simulation of the electron trajectory through the streak camera Starting with electrons liberated from the photocathode and accelerated by the anode-photocathode electric field, the simulation tracks their path through the meander sweep plates (with fixed bias applied) and their imaging onto the detector by the Glaser lens At the time this work was undertaken, this model represented to the best of the authors knowledge, the first simulation of a streak camera with all sub-system components incorporated into a single model in a self consistent manner Close agreement between the analytical and empirical models is found The final mechanical design of the camera is presented Commissioning results of the streak camera performance with ultraviolet and soft x-ray photons are discussed We clearly demonstrate that the grazing incidence streak camera is viable tool for the detection of sliced x-ray photons

3.2   Design Considerations and Specification

To appreciate the design specification for the grazing incidence x-ray streak camera a greater understanding of the constraints imposed by the ALS slicing beamline is required Hence a brief overview of beamline 6 0 [117], undergoing its commissioning phase at the time of writing, is requisite The femtosecond laser system produces a 1 5 mJ pulse with temporal duration of 50 fs and central wavelength of 800 nm for interaction with the storage ring electrons Slicing occurs inside a wiggler with $M_W = 19$ periods, wiggler period $\lambda_W = 11$ cm and with the gap adjusted to provide a deflection parameter $K \approx 13$

This ensures the optimal interaction condition is satisfied, namely that the spontaneous emission from an electron passing through the wiggler has the same wavelength as the modulating laser photons The sliced electrons are then radiated by a 1 5 m long in-vacuum insertion device with $M_W = 48$ periods, $\lambda_U = 3$ cm and peak magnetic field $B_0 = 1\ 5$ T The gap is variable so the device can operate as a wiggler or as an undulator as desired by the experimentalist The result is sliced photons with temporal duration of 170 fs The duration of the sliced pulse is slightly larger than the laser pulse due to different electrons experiencing a different time of flight between the modulator and the radiator For sample excitation, the femtosecond laser system also provides a 1 mJ pulse with the same characteristics as the electron modulating pulse If desired, this pulse can be routed through an optical parametric amplifier (OPA) to produce light at different wavelengths The pump pulse has a variable delay up to 500 ns relative to the probe pulse arriving at the sample location

A pictorial view of the beamline downstream of the radiator is shown in Figure 3 2 on page 33 The beamline consists of two branches, individually optimised for operation in the hard x-ray (2 to 10 keV) and soft x-ray (150 eV to 2 keV) spectral ranges The synchrotron radiation from the in-vacuum insertion device is collected by a mirror optimised for a given branch The nominal source size is 710 μm (horizontal) × 72 μm (vertical) The mirrors provide about a 1 1 intermediate focus of the source downstream on slits used to discriminate against the picosecond background With the slits 200 μm vertically displaced from the maximum intensity of the picosecond pulse, background suppression is estimated to be at $\sim 10^{-4}$ The sliced photons which pass through the slits are further imaged by the optics of the respective branch In its present embodiment the slicing is set to operate at a repetition frequency of 20 kHz (the laser repetition rate) Water cooled choppers running at 20 kHz are used to remove the high average power associated with photons not participating in the pump-probe experiment that could otherwise destroy the sample under investigation

The radiation at the intermediate focus that passes through the slits on the hard x-ray branch is imaged through a Ge(111) double crystal monochromator using a series of mirrors The resulting monochromatic flux ($\sim 8 \times 10^2$ photons/pulse/0 1% bandwidth at 8 keV) is focused on the sample in a spot size measuring 110 μm (horizontal) × 100 μm (vertical) For energies greater than 3 keV the insertion device can only operate in wiggler mode Therefore one can can perform x-ray diffraction (XRD) experiments by setting the monochromator to diffract a specific wavelength of the wiggler radiation Alternatively one can perform extended x-ray absorption fine structure (EXAFS) measurements by scanning the monochromator over the desired energy range

The soft x-ray branch is designed for x-ray absorption spectroscopy measurements Radiation from the insertion device operating in an undulator configuration passes through
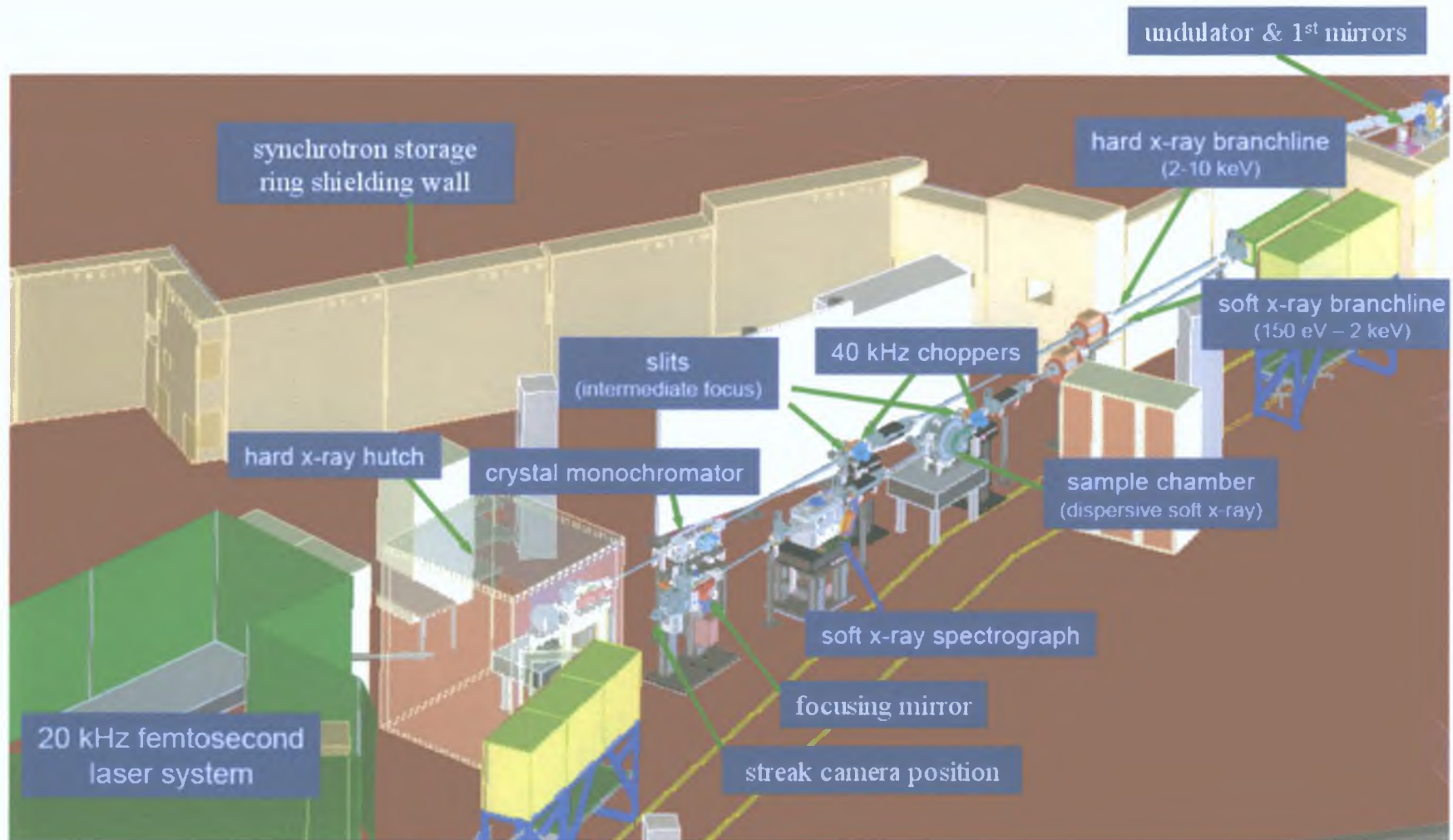
Figure 3.2: Pictorial view of the slicing beamline at the Advanced Light Source depicting the hard and soft x-ray branches. The location of the streak camera on the soft x-ray branch is indicated.

the sample under study. By accepting a relatively large angular aperture (0.5 mrad × 0.5 mrad), the undulator harmonics are broad enough to collect a near edge spectrum at one time. Nominal sliced photon fluxes incident on the sample are 2×10^3 photons/pulse/0.1% bandwidth at 800 eV. The transmitted x-rays are imaged onto a detector by a variable line spacing grating spectrograph with a specified energy resolution of $\Delta E / E = 5 \times 10^{-4}$ (at the Ni L-edge) and an energy range of 60 eV (at the C K-edge). The resulting dimensions of the focused spectrum on the detector are 50 μm (horizontal) × 10 mm (vertical).

For the streak camera the horizontal beam size has direct implication on the camera's temporal resolution and the photon flux on the signal to noise ratio. The salient parameters of both beamline branches are summarised in Table 3.1. It was desired that the streak camera have an instrument resolution of approximately 1 ps, thus increasing the sliced signal to unsliced background contrast by a factor of ~ 70 compared to a slow integrating detector.

Branch	Spot Size [μm (h) × μm (v)]	Photons/s
Soft X-ray	50×10^4	1×10^6 @ 300 eV in 0.1 % BW
Hard X-ray	110×100	1×10^5 @ 5 keV

Table 3.1: Beam size and sliced photon flux parameters for the Advanced Light Source slicing beamline. The picosecond background photon flux transmitted through the aperturing slits is of the same order as the sliced photon flux.

For typical applications on the hard x-ray branch, monochromatic radiation will be incident on the detector. To minimise the contribution to the imaging resolution due to the finite width of the unswept image w_{dc}, the horizontal spot size on the photocathode needs to be preserved in accordance with Equation (1.1). In contemporary normal incidence x-ray streak cameras used for hard x-ray applications ($E \approx 10$ keV) [118], a photocathode structure consisting of 1000 Å CsI on a 300 Å thick Au conduction layer is used. Mechanical support is offered to the photocathode by a 1000 Å thick Si_3N_4 or polyimide layer. Bonding the Au layer to the Si_3N_4 is accomplished using a 50 Å Ti wetting layer. The whole structure is supported on a 300 μm Si frame. These photocathodes are primarily inefficient due to transmission of over 95 % of the incident photons through the entire photocathode structure. Therefore a normal incidence configuration is unsatisfactory for our photon hungry application. To increase detection efficiency the photocathode can be placed at grazing incidence with respect to the vertical (unswept) axis. From the data shown in Figures 2.5 and 2.7 in Chapter 2, and simulation results obtained using Fraser's model, it was decided to set the incidence angle at 5° for monochromatic applications. Thus the effective spot size on the photocathode will measure ~ 100 μm (horizontal) ×
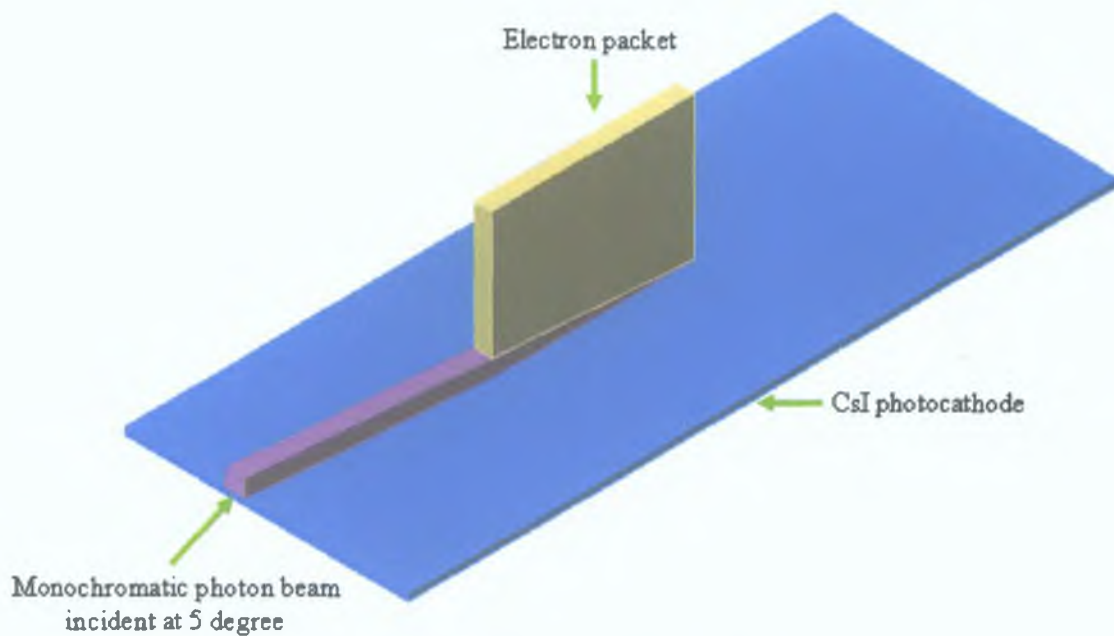
(a) Monochromatic cathode configuration.
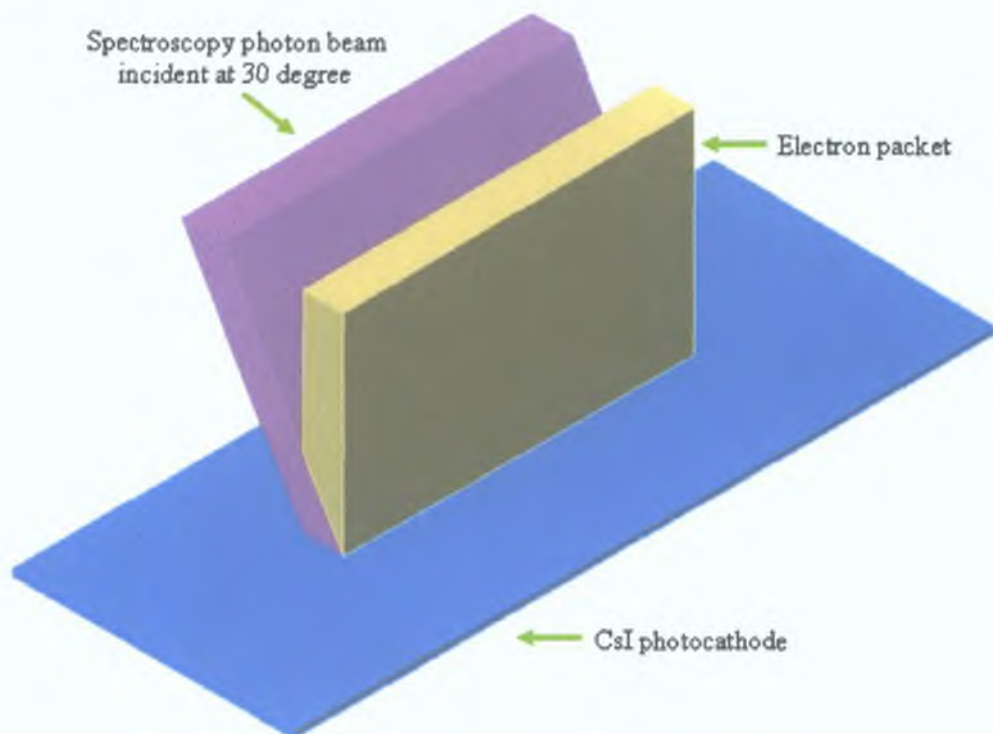
(b) Spectroscopic cathode configuration.

Figure 3.3: Cathode configuration for (a) monochromatic and (b) spectroscopic measurements. Not drawn to scale.

1 mm (vertical) An illustration of the cathode configuration for monochromatic applications is shown in Figure 3 3 (a) on page 35

Design constraints differ for the soft x-ray branch of the beamline Now the vertical axis must be preserved as it contains the spectroscopic information Examining normal incidence x-ray streak cameras used for soft x-ray ($E \approx 100$ eV) applications one observes that a slightly different photocathode structure is employed [119, 120] These photocathodes consist of a 500 Å CsI polycrystalline layer on a 300 Å Al conduction layer, supported by a 500 Å thick polyimide layer Mechanical support is provided by a Si_3N_4 substrate For this configuration only 30 % of the photons incident on the structure are absorbed within the CsI layer Efficiency in this geometry is primarily comprimised by photon absorption in the support structures The situation is compounded further when one realises that only electrons generated within a mean free path of the photocathode exit surface contribute to the measured signal Therefore a reflection geometry is favoured by detective quantum efficiency considerations As the vertical axis must be preserved one can only increase efficiency by placing the photocathode at grazing incidence with respect to the temporal (horizontal) axis Referring to Chapter 2 at 500 eV one can see that the electron yield increases as the cosecant of the incidence angle and the detective quantum efficiency demonstrates a commensurate though less dramatic increase For the spectroscopic configuration described here, one can operate at a grazing angle of $30°$ and only broaden the temporal axis by a factor of 2 The temporal resolution deteriorates by the same factor compared to normal incidence However, the increase in the detective efficiency offered by the reflection geometry coupled with the greater absorbed photon flux by the photocathode warrents a comprimise The effective spot size on the photocathode will measure ~ 100 μm (horizontal) $\times$ 10 mm (vertical) An illustration of the cathode configuration for polychromatic applications is shown in Figure 3 3 (b) on page 35

For a given sweep speed the temporal resolution will be the same in the soft x-ray spectroscopic and hard x-ray monochromatic configurations as the unswept horizontal image size is now identical A microchannel plate (MCP) mounted in close proximity to a fast phosphor that is in turn fibre coupled to a CCD detector will constitute the imaging detector at the back end of the streak camera This detection scheme has been chosen as one can gate the gain on the MCP by pulsing the bias voltage, eliminating the background contribution from x-ray pulses not coinciding with the laser pulses Typically MCPs possess a pore size of ~ 12 μm However the spatial resolution of the combined MCP, phosphor and CCD detector is ~ 100 μm Therefore it is desirable to magnify the image of the source, ~ 100 μm in our case, by a factor of ~ 2 to facilitate data centroiding With a desired temporal resolution of 1 ps and an unswept static image on the detector of 200 μm, this implies our camera should have a sweep speed of 2×10^8 m/s The camera should also possess a timing window of sufficient extent to resolve dynamics occurring on timescales

comparable to the intrinsic ALS pulse duration ($\geq$ 100 ps) The camera should also incorporate a capability for in-situ characterisation of the temporal resolution This can be achieved using an auxiliary port on the camera to admit an ultraviolet pulse train with a known inter pulse delay

For both geometries a 1000 Å CsI photocathode on an optically polished Al blank will constitute the photocathode This structure is both elegant and much more robust than normal incidence photocathodes that are susceptible to catastrophic failure through rupture caused by electric arcing and vacuum fluctuations Though the pulsed MCP detection scheme proposed above will work whilst the slicing scheme is operating on the ALS camshaft pulse, it will be appreciated that in the future slicing may be performed in the multi-bunch section of the ring fill pattern also Please refer to Appendix A for more details of the ALS time structure In the multi-bunch each bucket is separated by 2 ns Fast high voltage pulsers typically have rise and fall times on the order of tens of nanoseconds It will not be possible to gate the MCP on a timescale shorter than the inter bucket duration Therefore the streak camera should be upgradeable in the future with a mechanism wherein the photocathode can be biased on and off on a sub 2 ns timescale A microstripline photocathode similar to that used in the MCP design of [121] proffers a potential solution

Certain mechanical considerations need to be factored into the design specification For the soft x-ray branch, the photocathode needs to be located within the image plane of the spectrometer final focusing mirror Thus the distance between the photocathode and the mirror center should be 470 mm, or the photocathode center should be 240 mm from the exit port of said mirror housing This places stringent constraints on the floor plan of the camera All optical elements of the beamline are specified to operate in a UHV environment Thus a gate valve, isolating the beamline proper from the camera, along with a bellows to allow motion of the camera during alignment, has to be incorporated between the camera entrance port and the final mirror exit port

Mounting of the camera also requires some consideration The camera should be supported in a such a manner that it can be quickly interchanged between the spectroscopic and monochromatic configurations as required by the different beamline branches Thus the camera should be portable All sub-systems i e the photo-conductive switch and the optical elements used to generate the timing fiducials should be placed on the same mounting as the camera The mounting should incorporate translation in the $x-$, $y-$, $z-$ and $\theta-$ directions to facilitate accurate alignment of the photocathode with respect to the incident x-ray beam These specifications can be met by mounting the streak camera system on an optical breadboard attached to an ALS strut system [122] To fit on a standard optical breadboard of dimension 0 6 m $\times$ 0 9 m, the camera itself should be compact Thus the photocathode to detector distance should not exceed 50 cm

This completes the discussion of design related considerations for the grazing incidence x-ray streak camera A summary is provided in Table 3 2

Parameter	Soft X-ray branch	Hard X-ray Branch
fs signal ps background	~ 70	
Photocathode configuration	30° w r t swept axis	5° w r t to unswept axis
Spot sizes on photocathode	100 μm (h) x 10 mm (v)	110 μm (h) x 100 um (v)
Photocathode structure	1000 Å CsI on optically polished Al blank	
Gatable detection	MCP back coated with phosphor, fibre coupled to CCD Upgradeable to RF modulation of photocathode	
Lens magnification	~ 2	
Sweep speed	2 x 10^8 m/s	
Temporal resolution	~ 1 ps In-situ fiducials	
Timing window	$\geq$ 100 ps	
Vacuum	5 x 10^{-8} Torr or better	
Mechanical constraints	Photocathode located within 240 mm of final mirror exit port	
	Interchangeable between geometries Portable 3-axis plus angular alignment	
	Photocathode to detector distance less than 50 cm	

Table 3 2 Grazing incidence streak camera specifications

3.3   Modeling the X-ray Streak Camera

At the time of writing, a physical model incorporating all streak camera components does not exist To date, streak camera design has developed in an ad hoc manner with modeling of the sweep plates carried out to some extent separate of the camera imaging optics [123] To break the 100-fs barrier an integrated model incorporating all aspects of the streak camera, namely, the photocathode electron dynamics, acceleration by the anode-photocathode electric field, space charge effects, time-dependent sweep plate electrodynamics and the imaging optics, is necessary Here we pursue and make some modest progress toward this goal A semi-empirical model is used to determine the performance of the camera for a given sweep plate configuration Space charge and electron chromatic-

ity effects are treated analytically Magnetic field simulations for the Glaser lens with magnification determined by the design specification and static electric field simulations for the sweep plate configuration proposed by the semi-empirical model are performed with Poisson Superfish [124] The resulting camera model, incorporating electrostatic anode-photocathode and sweep plate fields, in conjunction with the magnetostatic field of the lens, is simulated using the linear accelerator modeling code PARMELLA [125]

We commence with photoemission of the secondary electrons from a 1000 Å thick CsI photocathode Temporal dispersion of the emitted electron bunch occurs between the anode and photocathode due to the combined influences of space charge and the secondary electron energy distribution, the effects of which can be reduced using large extraction fields For high intensity photonic signals occurring on a sub-picosecond timescale, space charge and self-field effects dominate the evolution of high density electron packets Using the photon fluxes specified earlier with quantum efficiency parameters from Chapter 2, nominal secondary electron densities were calculated Electron pulse broadening due to space charge was calculated to be negligible for an extraction field of 40 MV/m using the experimentally validated space charge models of Elsayed-Ali and Miller [126, 127] For two electrons instantaneously liberated from the cathode surface with energy difference ΔE, this initial kinetic energy difference in the presence of the photocathode-anode electric field translates into a time dispersion approximated by

$$\tau_{pc-a} = \frac{\sqrt{2m_e \Delta E}}{e\mathfrak{E}_{pc-a}} \quad , \tag{3 1}$$

where m_e and e are the mass and charge of the electron, respectively, ΔE is approximated by the full width at half maximum of the secondary electron energy distribution curve (1 6 eV for CsI) and $\mathfrak{E}_{pc-a}$ is the anode-photocathode electric field Calculated chromatic dispersion leads to an increase in the pulse duration by 0 1 ps for an acceleration potential of 10 kV To maximise sweep speed, whilst minimising transit-time dispersion and space charge effects in the field free region, contemporary ultrafast x-ray streak cameras situate the sweep plates upstream of the imaging optics as close to the anode as possible [123] Similar analysis shows that the anode to sweep plate transit-time dispersion can be approximated by

$$\tau_{a-sp} = \frac{t_{a-sp}}{2} \frac{\Delta E}{E_0} = \frac{d_{a-sp} \Delta E \sqrt{m_e}}{(2E_0)^{\frac{3}{2}}} \quad , \tag{3 2}$$

where E_0 is the mean electron energy at the anode Transit-time dispersion and space charge effects are insignificant for sweep plates situated within $d_{a-sp} \leq 1$ cm of the anode

Imaging of the electron bunch leaving the photocathode onto the detector is achieved with a Glaser magnetostatic lens Basically a Glaser lens is a solenoidal magnet consisting

of an iron yoke and pole pieces. A Glaser lens is superior to the double electrostatic quadrupole lens arrangement used in some ultrafast streak cameras [28] as the strong axial magnetic field focuses in all meridian planes, the lens itself is more compact and does not have to be placed in vacuum. The focal power of a Glaser lens is greater for off-axis particles; thus an intrinsic spherical aberration exists [128]. To reduce the spherical aberration the pole pieces in our design are tapered [129, 130]. A cross-section view of the magnetic lens constructed from 1006 hot rolled steel and the resulting field simulated with Poisson Superfish is shown in Figure 3.4.
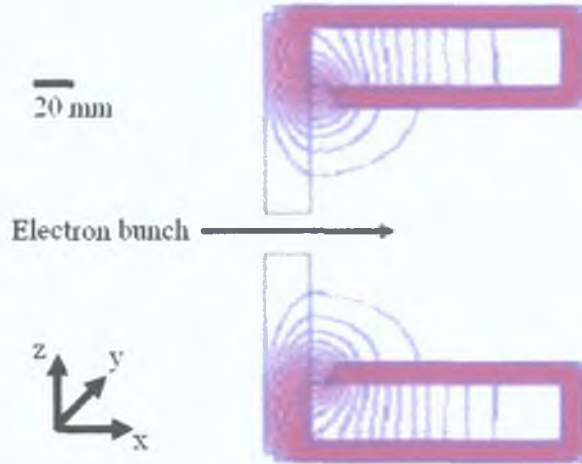
Figure 3.4: Cross-section view of Glaser lens. Lines of constant magnetic flux density are shown with the electron packet propagating through the lens.

Characterisation of the lens was performed before insertion into the streak camera. Measurement of the on-axis $\mathfrak{B}$-field was made using a DTM-151 Digital Teslameter. The detector head was mounted on-axis in the field using a micrometer translation stage. The results, which show excellent agreement with simulation, are shown in Figure 3.5 on page 41. Electron motion through the lens is described by the Lorentz equation. In the paraxial limit one can show that the magnetostatic field behaves as a thin lens with focal length f described by Busch's formula [128]

$$\frac{1}{f} = \frac{e}{8m_e V_{pc-a}} \int_{-\infty}^{+\infty} B_x^2 dx \quad .$$ (3.3)

Thus a complicated problem in electrodynamics has been reduced to a very tractable problem within the gamut of paraxial ray theory. Using the thin lens formula

$$\frac{1}{u} + \frac{1}{v} = \frac{1}{f} \quad ,$$ (3.4)

where u and v are the object and images distances, respectively; one can set the requisite
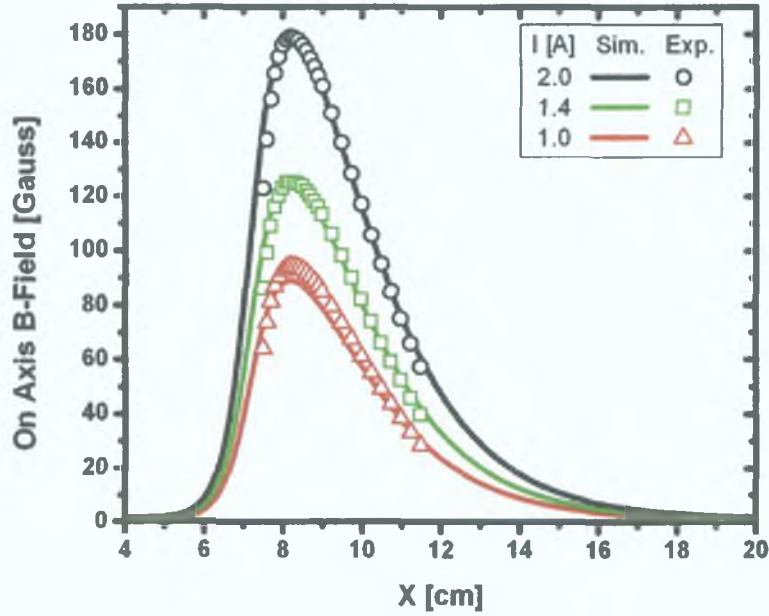
Figure 3.5: Glaser lens on-axis magnetic field $\mathfrak{B}_x$ as a function of lens current.

lens magnification $m = v/u = 2$ and seperately constrain the total photocathode to detector distance $l_{camera} = u + v \leq 50$ cm in accordance with the design specification. From Ampere's law, the strength of the magnetic field is linearly dependent on the current flowing through the coil wound around the pole pieces. Having decided upon u, v and m, one can set the focal length via the lens current to ensure the cathode image is in-focus in the detector plane.

A consequence of the radial magnetic field and the Lorentz equation is rotation of the image by an amount

$$\theta = \sqrt{\frac{e}{8m_e V_{pc-a}}} \int_{-\infty}^{+\infty} B_x dx \quad . \tag{3.5}$$

The rotation is uniform over the vertical spatial extent of the electron packet, thus the spatial and temporal axes of the camera remain linear.

To generate the linear ramp for the sweep plates a photo-conductive (PC) switch as shown in Figure 3.6 on page 42 is used. 800 nm photons ($E = 1.55$ eV $> E_g(GaAs)$) with ~ 100 fs duration, derived from the sample excitation pump beam, produce electron-hole pairs within a penetration depth of the GaAs surface. Thus a thin conductive layer effectively shorts the sweep electrodes. This rapid change in voltage on one side of the capacitors by an amount $|kV|$ leads to a change from $\pm kV/2$ to $\mp kV/2$ on the other side of the capacitors. For the PC switch used with the camera, several hundred volts can be switched within a rise time $t_r = 100$ ps onto the respective sweep plate. Due to the Gigahertz scale bandwidth associated with the signal, transmission line considerations are appropriate for the printed circuit board to which the GaAs switch is bonded. The board

has been designed with a characteristic impedance of 50 Ω. The sweep ramp pulse at the plate output can be terminated in a high power 50 Ω terminator or a sampling scope with sufficient input attenuation for diagnostic purposes. Electron-hole pair recombination returns the system to its initial state on a nanosecond timescale.
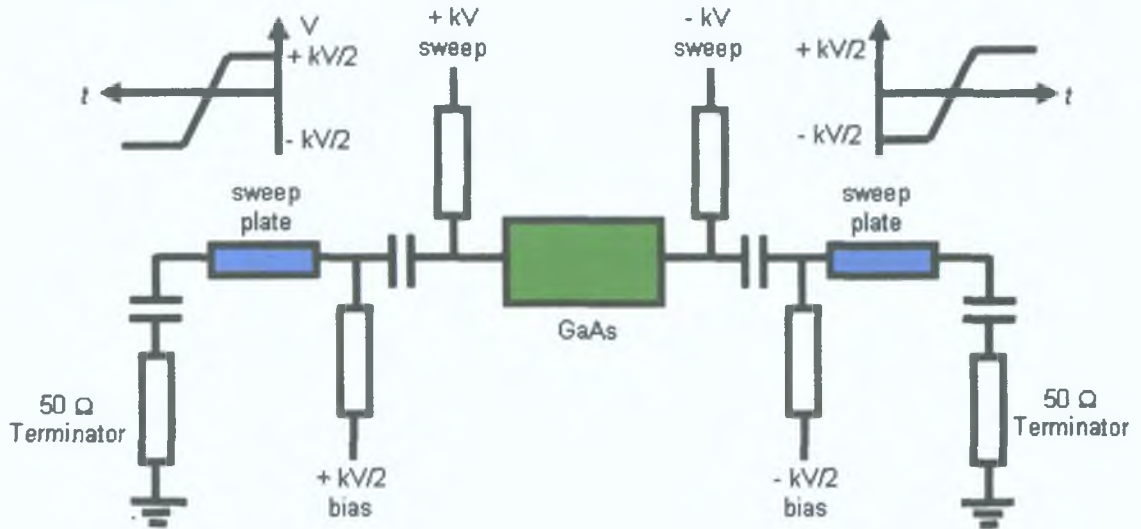
Figure 3.6: Photo-conductive (PC) switch used to generate sweep pulse.

For measurements performed in accumulation mode, fluctuations in the laser intensity cause variations in the amplitude of the sweep ramp. This corresponds to sweep speed variations and thus is a source of timing jitter. The timing jitter of the switch can be expressed as

$$\tau_{jitter} = 0.5 t_r \frac{\Delta V}{V_a} \quad , \tag{3.6}$$

where $\Delta V/V_a$ is the RMS fluctuation in the shot-to-shot switch output voltage. Generally, the switch is operated in saturation mode to minimize the effect of laser intensity fluctuations. Near jitter-free streak camera operation in accumulation has been demonstrated [23, 28]. However, for conventional PC-switches such as the one described here, intensity fluctuations on the order of 1 % cause timing jitter $\tau_{jitter} \approx 0.5$ ps. This is acceptable for our application.

The temporal resolution of a streak camera is inextricably linked to the sweep plate design. Consider a rectangular meander (serpentine) plate as shown in Figure 3.7 on page 43. It is assumed that the electrical pulse travels along the center of the meander. For the electrons to experience constant deflection, the velocity of the electrons through the sweep plate in the x−direction must match the velocity of the electrical pulse propagating around the meander.

This implies that per meander, the electron bunch with velocity $v_x = \sqrt{2E_{k_x}/m_e}$ tra-

42
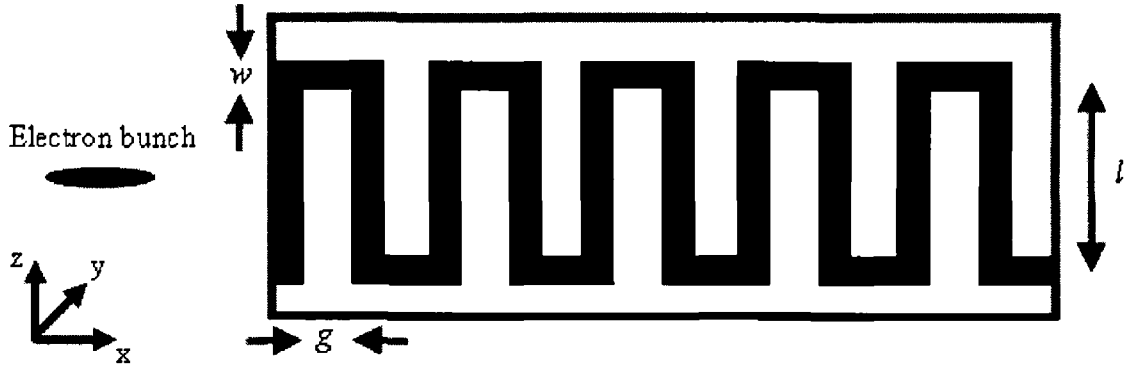
Figure 3 7   Meander sweep plate with square corners w is the track width, g is the gap between tracks and l the length of a meander leg

verses

$$l_e = w + g \quad , \tag{3 7}$$

whilst the electron pulse with velocity $v_p = c/\sqrt{\epsilon_{eff}(f)}$ travels a distance

$$l_p = l + g + w \quad , \tag{3 8}$$

where E_{k_x} is the electron kinetic energy in the x—direction and c is the speed of light It is necessary to consider an effective dielectric constant $\epsilon_{eff}(f)$ as wave fields exist in both dielectric media (the substrate and vacuum) and the conductor Thus hybrid modes propagate on the microstrip line and the wave velocity is frequency dependent [131]

For the electron bunch and sweep ramp to stay in phase the following condition must be satisfied

$$l_p = \left(\frac{v_p}{v_x}\right) l_e \tag{3 9}$$

Thus a relationship is established between the propagation speed of the sweep ramp, the kinetic energy of the electrons and the geometry of the meander plate

$$l = \frac{(w + g)}{c} \sqrt{\frac{2E}{m_e \epsilon_{eff}(f)}} - (2w + g) \tag{3 10}$$

Impedance matching places a constraint on the width of the meander trace w, whilst phase matching of the electron pulse to the sweep signal dictates the meander path length l and the spacing between meander legs g A cross-section view of the microstrip environment is shown in Figure 3 8 on page 44

A characteristic impedance $Z_0 = 50\ \Omega$, at a frequency that will support a sweep pulse with rise time $t_r = 100$ ps, is found for $w = 1\ 65$ mm using the expression derived by
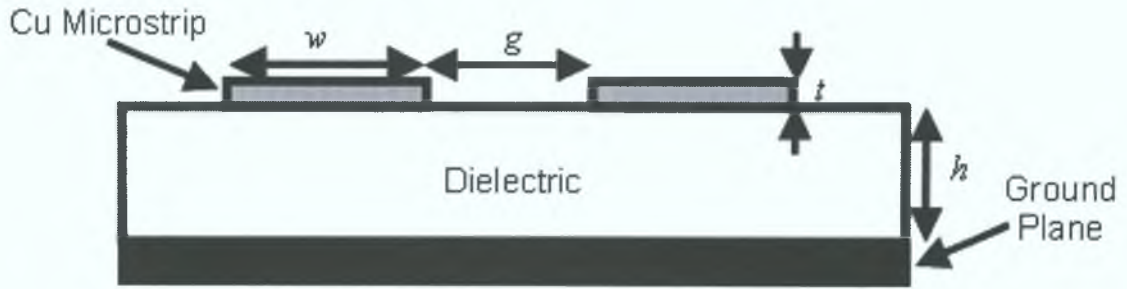
Figure 3.8: Cross-section view of microstrip environment. w is the track width, g is the gap between tracks, t is the copper track thickness and h is the thickness of the dielectric.

Wheeler [132] for an isolated track

$$
Z_0 = \frac{\eta_0}{2\sqrt{2}\pi\sqrt{\epsilon_{eff}+1}} \times
$$

$$
\ln\left\{1 + \frac{4h}{w'}\left[\frac{14 + 8/\epsilon_{eff}}{11}\frac{4h}{w'} + \sqrt{\left(\frac{14 + 8/\epsilon_{eff}}{11}\right)^2\left(\frac{4h}{w'}\right)^2 + \frac{1 + 1/\epsilon_{eff}}{2}\pi^2}\right]\right\} \quad ,
\tag{3.11}
$$

where η_0 is the vacuum impedance and w' is the equivalent width of a track of zero thickness due to a track of rectangular profile, width w and thickness t. We use an effective dielectric constant proposed by Kirschning and Jansen [133]

$$
\epsilon_{eff}(f) = \epsilon_{eff}(0)\frac{1 + K_7 P}{1 + P} \quad ,
\tag{3.12}
$$

with the zero-frequency dielectric constant proposed by Hammerstad and Bekkadal [134]

$$
\epsilon_{eff}(0) = \frac{\epsilon_r + 1}{2} + \frac{\epsilon_r - 1}{2}\left[\left(1 + \frac{12h}{w}\right)^{-0.5} + 0.04\left(1 - \frac{w}{h}\right)^2\right] \quad ,
\tag{3.13}
$$

where the parameters K_7 and P are defined in [133].

The meander leg length l must be greater than the vertical dimension of the electron packet leaving the photocathode. To satisfy the spectroscopic configuration requirements this implies $l \geq 10$ mm. As the track width w is now fixed, one can see from Equation (3.10), that any variation in the meander length l must be compensated by the inter-track spacing g to maintain the phase matching condition. For time-resolved measurements that will be made using the ALS intrinsic pulse duration (~ 70 ps), the resulting electron bunch length in the camera is approximately 4 mm. Thus the head of the packet will experience a deflection from track n and the tail from track $n - 1$ for gap spacings less than the electron bunch length. It will be appreciated that forward and backward coupling of the

propagating sweep pulse between tracks can occur [135,136]. This crosstalk may increase or reduce the uncoupled inter-plate electric field strength leading to an inhomogeneous sweep.

Therefore two operational limits place bounds on the meander length l. First, as the fringe field dimension at the end of the meander leg will be of the order g, the meander length must exceed the largest vertical beam dimension on the photocathode by a few inter-track spacings. This will reduce electric field aberrations at the electron packet vertical extremities. Second, crosstalk and unfortunately the sweep speed, can be reduced by increasing the inter track spacing. Therefore a design compromise must be found that provides a balance of satisfactory sweep speed with minimal inter-track coupling.

The coupling constant between two parallel microstrips is defined as

$$k = \frac{Z_{0,e} - Z_{0,o}}{Z_{0,e} + Z_{0,o}} \quad , \tag{3.14}$$

where $Z_{0,e}$ and $Z_{0,o}$ are the even-mode and odd-mode impedances presented to the signal [137]. $Z_{0,e}$ occurs when both tracks are at a positive potential with respect to the ground plane, and $Z_{0,o}$ when the tracks are at opposite potentials with respect to the ground plane. The characteristic impedance is related to the even- and odd-mode impedances as follows

$$Z_0 = \sqrt{Z_{0,e} Z_{0,o}} \quad . \tag{3.15}$$

We use the even- and odd-mode impedances for a coupled microstrip environment suggested by Kirschning and Jansen [138, 139]

$$Z_{L_o}(f_n) = Z_L(f_n) + \frac{\left\{ Z_{L_o}(0) \left[\frac{\epsilon_{eff_o}(f_n)}{\epsilon_{eff_o}(0)} \right]^{Q_{22}} - Z_L(f_n)Q_{23} \right\}}{\left\{ 1 + Q_{24} + Q_{25} \left(\frac{0.46g}{h} \right)^{2.2} \right\}} \quad , \tag{3.16}$$

$$Z_{L_e}(f_n) = Z_{L_e}(0) \frac{\left\{ 0.9408 \left[\epsilon_{eff}(f_n) \right]^{C_e} - 0.9603 \right\}^{Q_o}}{\left\{ [0.9408 - d_e] \left[\epsilon_{eff}(f_n) - 0.9603 \right]^{C_e} \right\}^{Q_o}} \quad , \tag{3.17}$$

where the normalised frequency $f_n = (f/GHz)(h/mm)$ and $Z_L(f_n)$ is the frequency-dependent characteristic impedance of a single microstrip with width w as defined in [140]. All other parameters are defined in [138, 139] and the references contained therein. The microstrip environment and in particular the track spacing g is explicitly and implicitly encapsulated in Equations (3.16) and (3.17). Iterative design has shown that an inter-track spacing $g = 1.4$ mm leads to a coupling of ~ 7.5 % with satisfactory sweep speed as estimated with the proceeding analysis.

45

Poisson Superfish was used to simulate the electrostatic field between the sweep plates The equipotential surface is shown in Figure 3 9 on page 47 with a close-up shown in Figure 3 10 on page 48 Significant fringe fields can be seen at the entrance and exit of the sweep plate system, whilst moderate fringing is observed in the inter-track region These fringe fields will obviously effect the electron trajectory However, particle trajectory simulations of a full camera are somewhat laborious and therefore a simplified analytical model incorporating the sweep plate structure can be advantageous until one is close to the final specification

Before a calculation of the sweep speed is presented, it is first appropriate to attempt to gain some appreciation for the effect of crosstalk on the linear ramp Constrained by our software limitations, we model a single sweep plate meander as a series of coupled lossy transmission lines with PSpice A representation of the meander and its corresponding equivalent electrical circuit is shown in Figure 3 11 on page 49 Each part of the meander between corners has been modeled as a transmission line, with an appropriate distributed coupling capacitance and inductance included The discontinuities at the corners have been modeled by an L-C circuit after [141] For square corners the capacitance and inductance are given as

$$C[\text{pF}] = 0\ 001h[\text{mm}] \left[(10\ 35\epsilon_r + 2\ 5) \left(\frac{w}{h}\right)^2 + (2\ 6\epsilon_r + 5\ 64) \left(\frac{w}{h}\right) \right] \quad , \qquad (3\ 18)$$

$$L[\text{nH}] = 0\ 22h[\text{mm}] \left[1 - 1\ 35 \exp\left(-0\ 18 \left(\frac{w}{h}\right)^{1\ 39} \right) \right] \qquad (3\ 19)$$

For a chamfered microstrip right-angle bend

$$C[\text{pF}] = 0\ 001h[\text{mm}] \left[(3\ 93\epsilon_r + 0\ 62) \left(\frac{w}{h}\right)^2 + (7\ 6\epsilon_r + 3\ 80) \left(\frac{w}{h}\right) \right] \quad , \qquad (3\ 20)$$

$$L[\text{nH}] = 0\ 44h[\text{mm}] \left[1 - 1\ 062 \exp\left(-0\ 177 \left(\frac{w}{h}\right)^{0\ 947} \right) \right] \qquad (3\ 21)$$

To accentuate the salient crosstalk features we first apply a linear piecewise pulse changing from -250 V to +250 V during a rise time of 100 ps The results are shown in Figure 3 12 (a) and (b) on page 51 for square and mitred corners, respectively Referring to Figure 3 11, as the signal propagates along the meander leg AB (the aggressor line), electrons in the leg CD (the victim line) experience repulsion via capacitive crosstalk Thus victim line electrons will move toward point C (forward capacitive crosstalk, referred to as XC_F in figure) and point D (backward capacitive crosstalk, referred to as XC_B in figure) The current flow due to the pulse moving along the leg AB has an associated magnetic field This field will intersect the victim line and generate a current flow (via inductive crosstalk) in the direction opposite to the pulse propagation i e toward corner D (back-
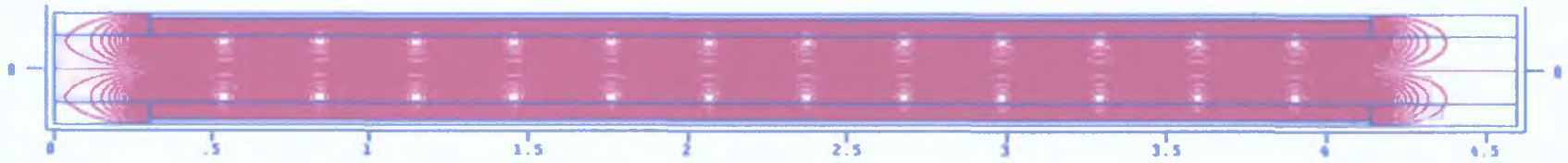
Figure 3.9: Simulated electric field between sweep plates. Simulation parameters: applied bias voltage of ± 35 V, track width $w = 1.65$ mm, inter-track spacing $g = 1.4$ mm and an inter-plate spacing of $d = 3$ mm.
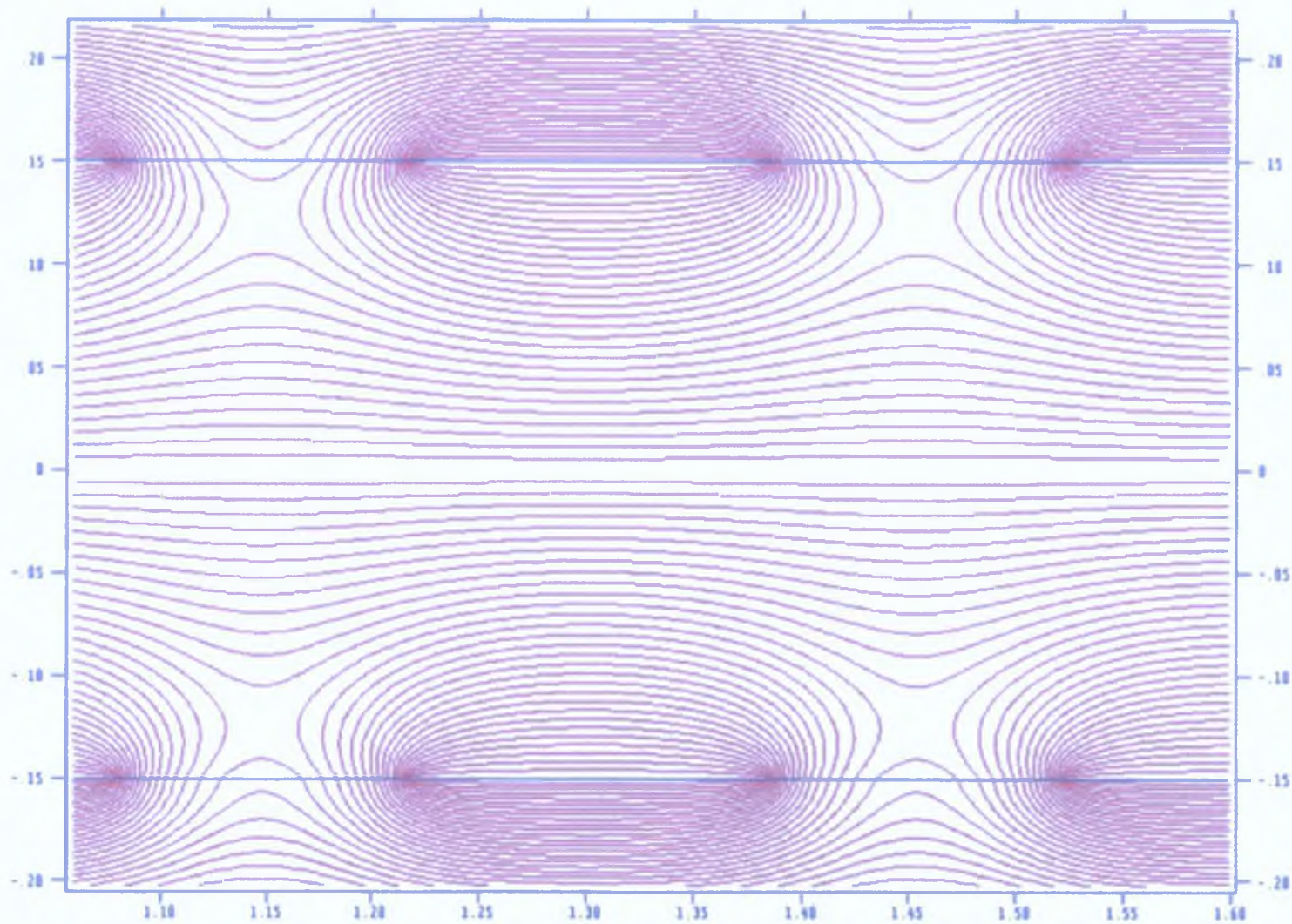
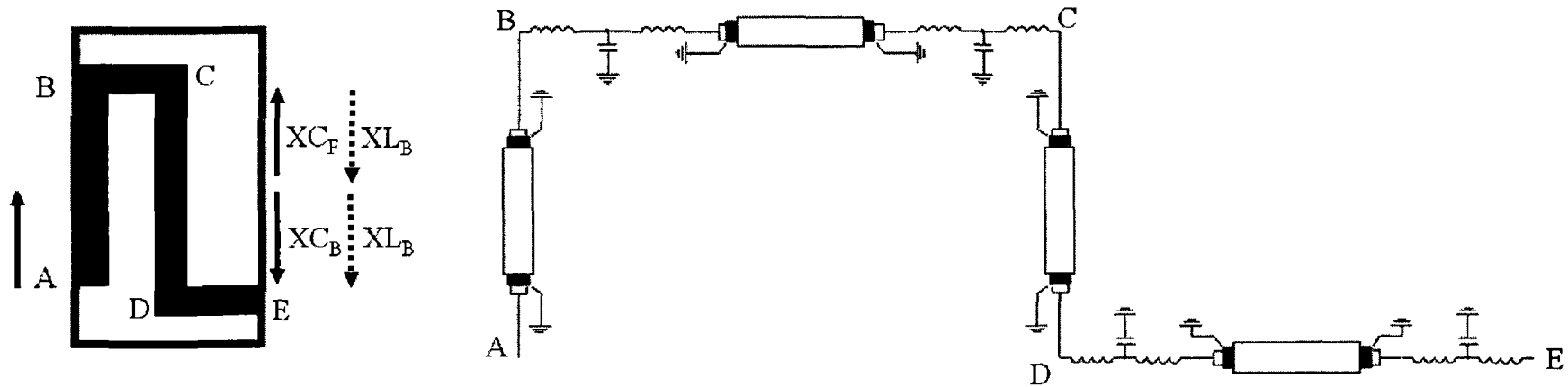Figure 3.10: Close-up view of the sweep plate electric field simulated in Figure 3.9.

XC$_F$ XL$_B$

XC$_B$ XL$_B$

Figure 3 11 Model of coupling in a single meander The meander and its electrical equivalent are depicted

ward inductive crosstalk, referred to as XL_B in figure) For a microstrip environment, the forward capacitive crosstalk (XL_F) is cancelled by the backward inductive crosstalk (XL_B) In the backward direction, the two signals reinforce one another [135, 136] Thus as the pulse progresses from A toward B a backward crosstalk component in leg CD will move ahead of the pulse toward the meander output E This component of the pulse is denoted by X and Y in Figure 3 12 As the sweep pulse rounds the corner of the meander and progresses from C toward D, a backward crosstalk component is generated in the leg AB As the signal progresses, it will continue to couple into leg AB producing a crosstalk signal behind the main signal If there were no discontinuities i e corners in the structure, the crosstalk dynamics in both legs would be perfectly symmetrical However, the backward crosstalk signal in leg AB now experiences four corners B, C, D and E, whereas, the component that propagates ahead of the signal only propagates through corners D and E This explains the different structure presented in the pre-trace and retrace segments of the linearised sweep pulse Comparing Figures 3 12 (a) and (b) one can see that mitred corners clearly present a smaller discontinuity to the propagating signal and should be employed where possible

To conclude our analysis of crosstalk in serpentine traces, a pulse, similar to that observed from the output of the photoconductive switch discussed previously, is applied to a single mitred corner meander Initially the pulse grows exponentially, before entering a linear region of duration $\sim$ 100 ps that is used for streaking (see Figure 3 13 on page 52) Electron-hole pair recombination in the GaAs switch causes decay of the pulse back to its initial value One can see that the linear portion of the sweep signal remains unaffected during propagation through the meander The pre-trace and re-trace portions of the pulse are affected by the crosstalk processes previously discussed

Thus within the bounds of our model we can see that the linear ramp is not affected by crosstalk and we can consider the sweep to be linear with respect to the electron motion through the meander structure We are now in a more favorable position to calculate the sweep speed analytically The timing window is set by the linear portion of the sweep pulse rise time $t_r = 100$ ps To compute the sweep speed we follow the motion of an individual electron through the meander field using elementary kinematics By finding the position of the deflected electron on the detector at the start and end of the sweep, one can ascertain the sweep speed as this motion occurs during the rise time of the pulse We neglect space charge and fringe field effects as these are more appropriately treated in the simulation discussed below Relativistic and crosstalk effects are also neglected Differences in the propagation speed about a meander for square and mitred corners can be neglected and a meander structure with square corners as depicted in Figure 3 7 on page 43 is assumed for simplicity Consider a linearised sweep trace model shown in Figure 3 14 on page 52
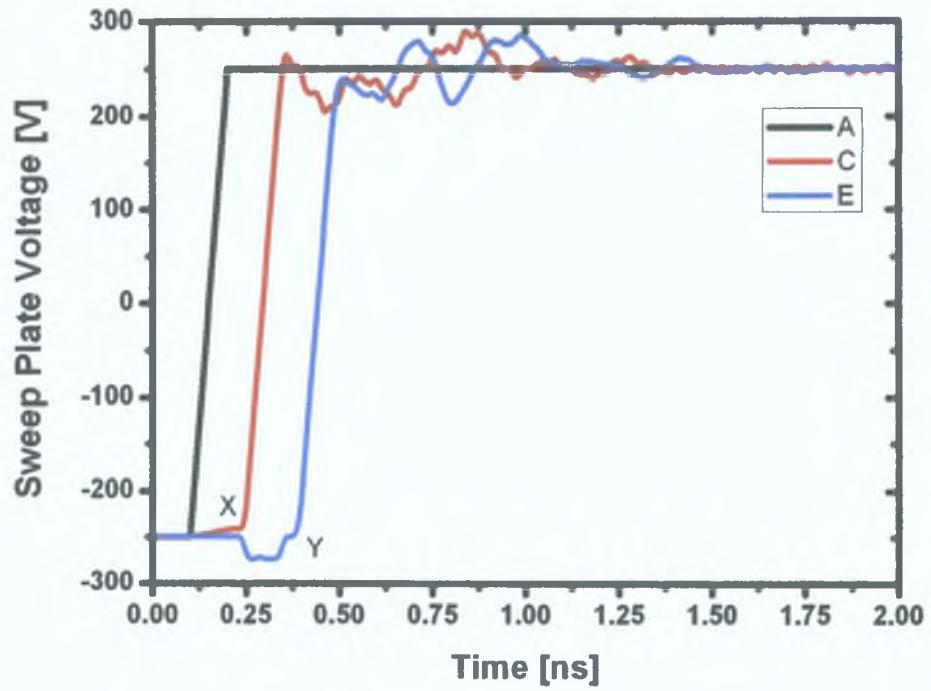
(a) Square corners.
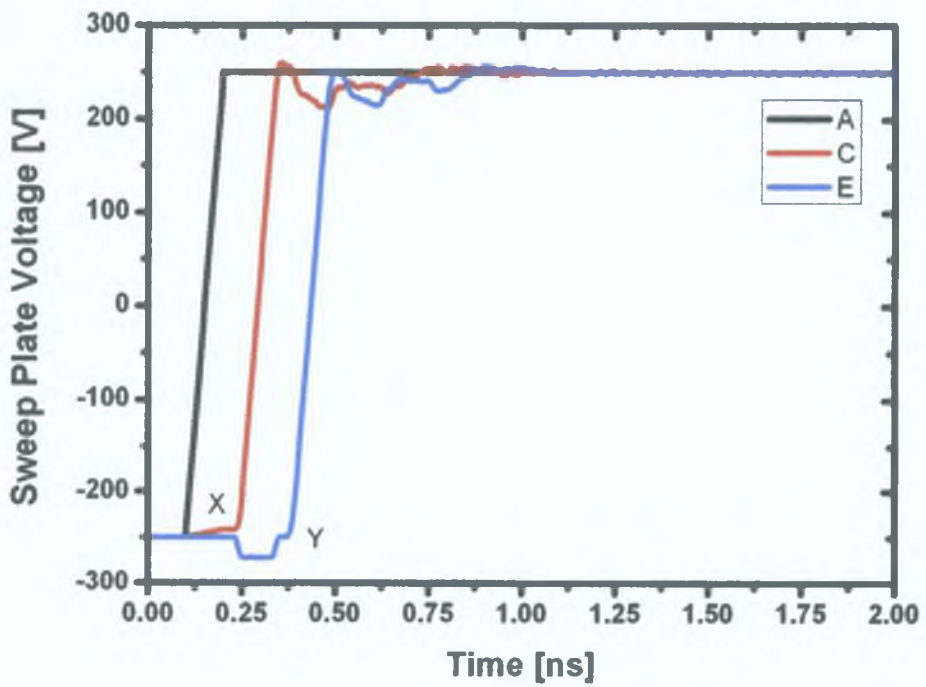
(b) Mitred corners.

Figure 3.12: Output from single meander of a coupled microstrip environment with (a) square corners and (b) mitred corners for linearised sweep pulse. The legend corresponds to the points shown on the meander of Figure 3.11.
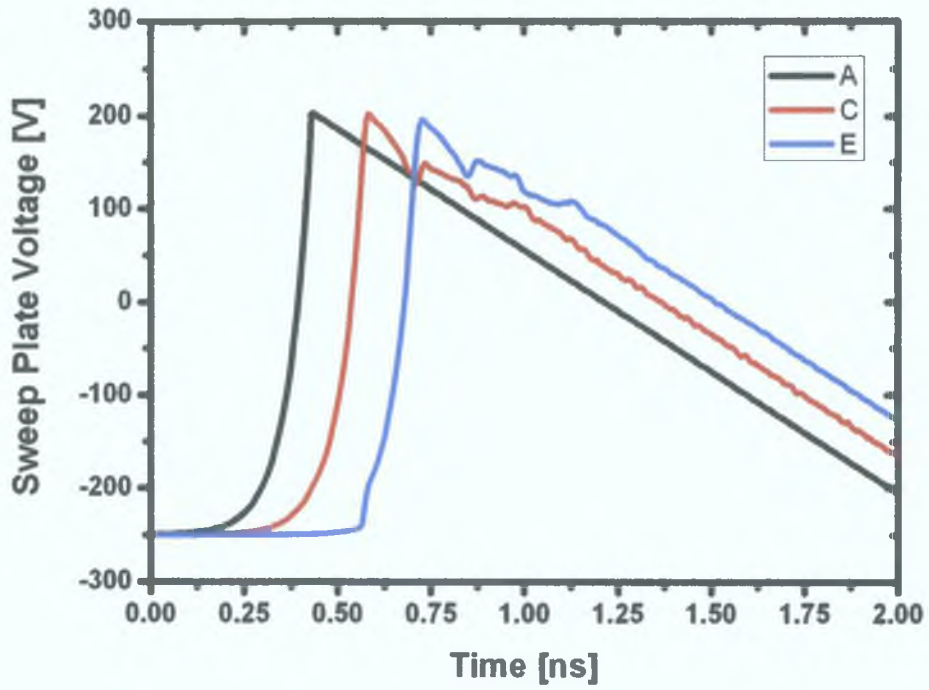
Figure 3.13: Output from single meander of a coupled microstrip environment with mitred corners for typical sweep pulse generated by PC switch. The legend corresponds to the points shown on the meander of Figure 3.11.
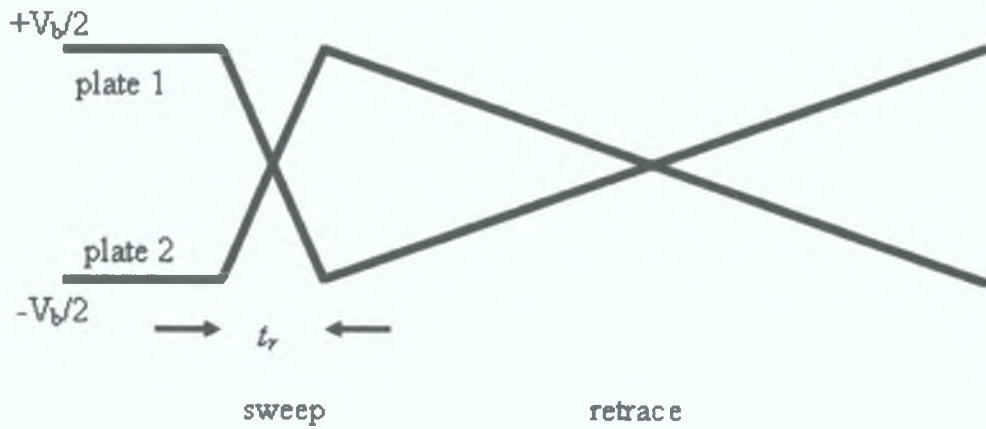
Figure 3.14: Linearised sweep trace. Voltages on plates switch by twice the bias voltage V_b during rise time t_r, producing the deflection field. The sweep plates are separated from one another by a distance d.

The sweep field $\mathcal{E}_y(t)$ as a function of time may be written as

$$\mathcal{E}_y(t) = \mathcal{E}_{max} - t\left(\frac{2\mathcal{E}_{max}}{t_r}\right) \quad , \qquad (3.22)$$

where the maximum field between the plates occurring at the start and end of the trace is

$|\mathcal{E}_{max}| = |V_b|/d$ An electron will take a finite amount of time $\tau_w = w/v_x$ to traverse the track w During this period the electron will sample a finite portion of the time varying field and experience a deflection force

$$F_y(t) = -e\mathcal{E}_y(t) \tag{3 23}$$

Thus the electrons initial lateral velocity upon entering the track u_y will change to

$$
\begin{aligned}
v_y(\tau_w) &= u_y - \frac{e}{m} \int_0^{\tau_w} \mathcal{E}_y(t')dt' \\
&= u_y - \frac{e\mathcal{E}_{max}}{m_e}\frac{w}{v_x} + \frac{e}{m_e}\frac{w^2}{v_x^2}\frac{\mathcal{E}_{max}}{t_r}
\end{aligned} \tag{3 24}
$$

at the exit of the track Similarly, the electrons initial lateral displacement y_0 will change to

$$
\begin{aligned}
y_y(\tau_w) &= y_0 + \int_0^{\tau_w} v_y(t')dt' \\
&= y_0 + u_y\tau_w - \frac{e\mathcal{E}_{max}\tau_w^2}{2m_e} + \frac{e}{m_e}\frac{\mathcal{E}_{max}\tau_w^3}{3t_r}
\end{aligned} \tag{3 25}
$$

During the electrons' motion through the inter-track field free region, the $y-$ displacement will change by a further amount

$$y_g = \frac{v_y(\tau_w)}{v_x}g \tag{3 26}$$

For each meander in the sweep plate system one iterates through Equations (3 24), (3 25) and (3 26) to find the resulting displacement of the electron at the output Due to the small angles involved, this displacement is back-propagated to the anode as a virtual source for the Glaser lens Using the lens magnification one can then forward propagate this virtual source as a real image corresponding to the physical displacement of the electron in the detector plane The maximum displacement at the start and end of the sweep occurs at $\pm i_d$, respectively Thus the sweep speed is

$$v_{sweep} = \frac{2i_d}{t_r} \tag{3 27}$$

Using the sweep plate geometry defined above and the lens magnification we find a sweep speed $v_{sweep} = 7 \times 10^7$ m/s For a 100 μm image on the photocathode, this corresponds to a single shot temporal resolution of $\tau_{dc} = 2$ 9 ps

The temporal response of the streak camera $\tau_{instrument}$ is the quadrature sum

$$\tau_{instrument} = \sqrt{(\tau_{dc})^2 + (\tau_{pc-a})^2 + (\tau_{a-sp})^2 + (\tau_{sc})^2 + (\tau_{jitter})^2} \quad , \qquad (3.28)$$

where τ_{dc}, τ_{pc-a}, τ_{a-sp}, τ_{sc} and τ_{jitter} are the instrumental contributions due to the finite slit width, the photocathode-anode dispersion, the anode-sweep plate dispersion, space charge broadening and jitter in the photoconductive switch, respectively [142]. Combining these effects in quadrature is only approximate, as Equation (3.28) assumes Gaussian energy distributions and independent contributions from the various broadening mechanisms. For the camera design described previously $\tau_{instrument} = 2.95$ ps. Given the modeling simplifications this is sufficiently close to the design specification to assume satisfactory agreement.

The linear accelerator code PARMELLA [125] was used to simulate the camera design illustrated above. An electron packet of dimension ~ 100 μm $\times$ 1 mm, consisting of 10^7 electrons, with temporal duration 70 ps was accelerated away from the photocathode by an extraction potential of 10 kV. This is representative of a monochromatic configuration at 1 keV. Secondary electrons emitted from the CsI photocathode were modeled by assigning an initial secondary electron energy of 1.5 eV (the mean secondary electron energy) and randomising these electrons with an energy of 1.3 eV (close to the FWHM of the secondary electron energy distribution curve) [91]. Thus the effect of electron chromaticity was incorporated. The simulation was run with space charge effects included. The two dimensional electrostatic field of the sweep plates shown in Figure 3.9 on page 47 was extrapolated into three dimensions and incorporated. The radial field of the magnetic lens was inserted downstream of the sweep plates.

In the first simulation the plates were unbiased to allow investigation of the imaging optics. An image of the electron packet as it leaves the photocathode is shown in Figure 3.15 (a) on page 55. Lineouts in the horizontal and vertical dimension are shown in Figure 3.15 (b). The evolution of the electron bunch is tracked via the RMS bunch size as it propagates through the camera. The focus point is determined to occur at a distance $l_{camera} = 43$ cm from the photocathode. This is within the requirements of the design specification. An image of the focused beam on the detector is shown in Figure 3.16 on page 56 along with the corresponding lineouts allowing for the 52° rotation due to the magnetic lens. Comparing the lineouts of Figures 3.15 and 3.16 one can see that the lens magnification is $m_h = 2.3$ and $m_v = 2.5$, in the horizontal and vertical directions, respectively. The magnification, which is within the design specification requirement, implies the focal length of the lens $f_{sim} = 8.8$ cm. A focal length $f_{theory} = 8.2$ cm was found using Equation (3.3) for the on-axis $\mathcal{B}$-field produced by Poisson Superfish. The non-paraxial nature of the simulation may account for the slight discrepancy between theory and simulation as
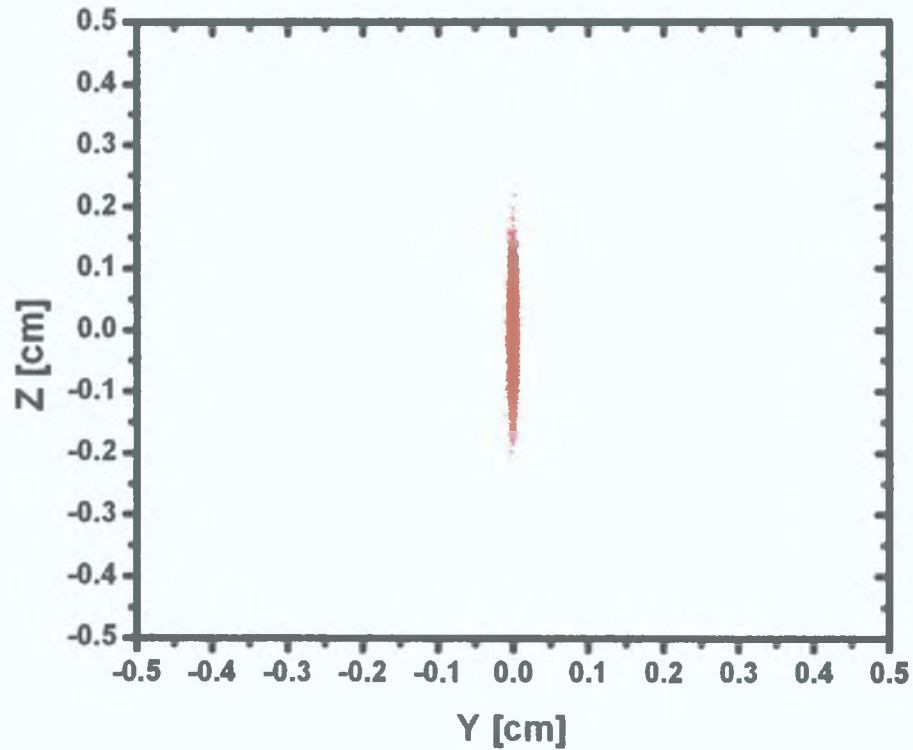
(a) Image.
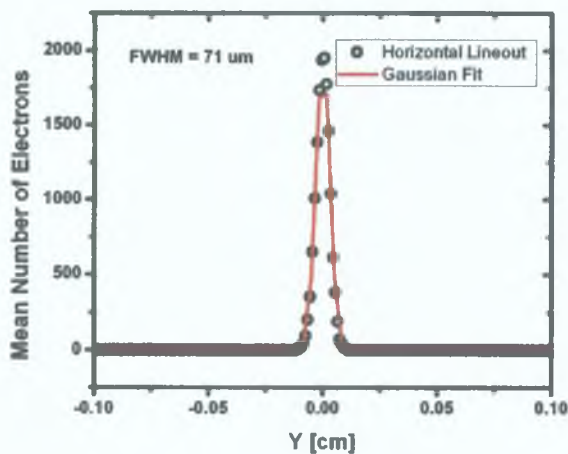
(b) Horizontal lineout.
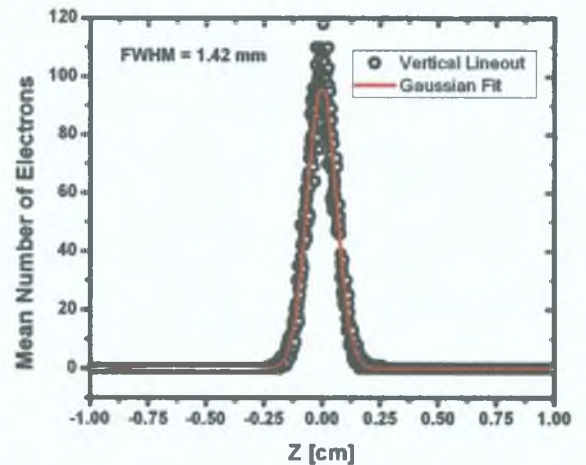
(c) Vertical lineout.

Figure 3.15: (a) Image of initial electron packet emitted from CsI photocathode. (b) Horizontal and (c) vertical lineouts measuring 71 μm × 1.42 mm, respectively.

the secondary electrons possess finite momentum in the direction perpendicular to the image plane. The $\theta = 52°$ rotation caused by the lens is in perfect agreement with the theoretical value calculated using Equation (3.5). Thus the detector should be rotated by $\theta = 52°$ so the vertical axes of the detector and the swept beam are parallel.

A simulation with a bias voltage of ±35 V applied to the sweep plates was performed.
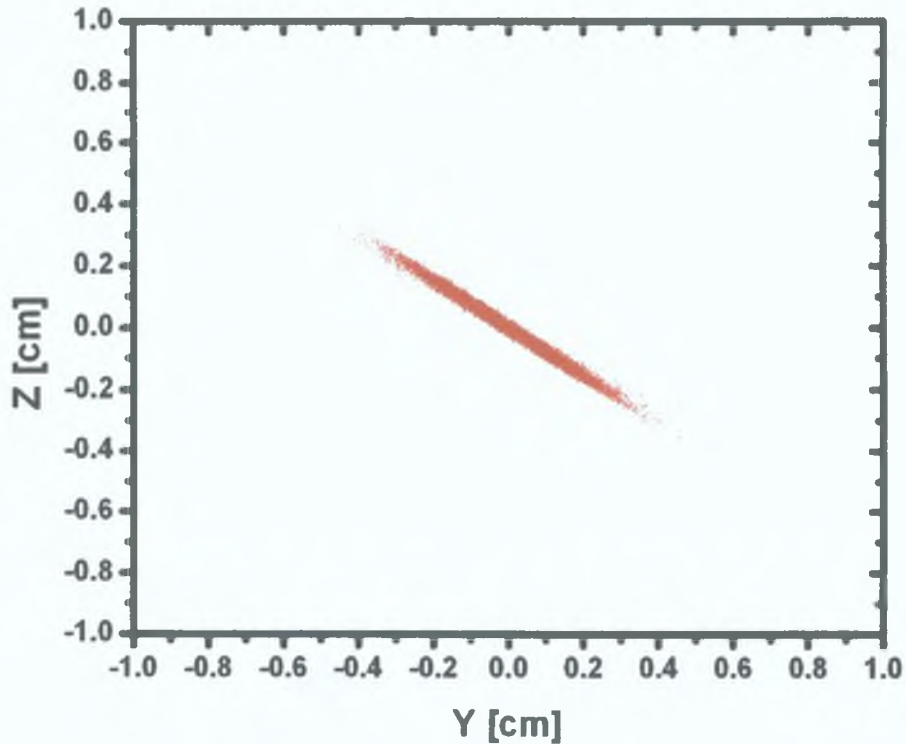
(a) Image.
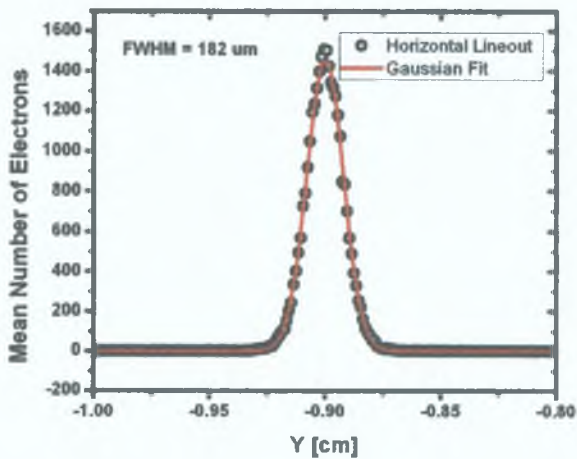
(b) Horizontal lineout.
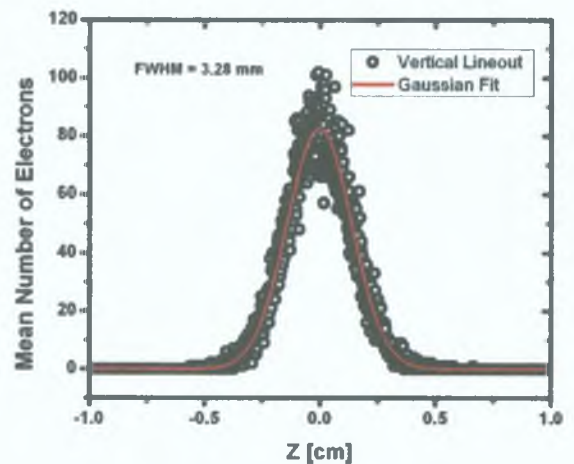
(c) Vertical lineout.

Figure 3.16: (a) Unswept image of electron packet in detector plane. The electrons have undergone a rotation of $\theta = 52°$ about the x-axis due to the Glaser lens. (b) Horizontal and (c) vertical lineouts measuring 182 μm $\times$ 3.28 mm, respectively.

This corresponds to the electrons being deflected close to the output of the sweep plate without being clipped. Thus the position of the electrons at the extremity of the sweep can be ascertained and in turn the temporal resolution via the rise time of the sweep ramp. The results are shown in Figure 3.17 on page 58. One can see that image size in the vertical dimension is preserved but significant scatter in the horizontal plane occurs. This is

directly attributable to the fringe fields in the sweep plate sub-system This was confirmed by replacing the plates with a parallel plate capacitor-type structure with constant electric field applied The electron packet was horizontally displaced without any manifestation of electron optical aberrations Referring to the close-up view of the sweep plate region (see Figure 3 10 on page 48), one can clearly see that the fringing effects are more pronounced at the edges of the plates in contrast to the central region Thus, the fringe field effects can be reduced by increasing the inter-plate spacing Comparable sweep speed can be maintained by increasing the bias and sweep potentials on the photoconductive switch For the data presented here, the scatter has been fitted with a double Gaussian peak The position of the most deflected peak occurs at $y \equiv i_d = -2\ 75$ mm Equation (3 27) yields a sweep speed $v_{sweep} = 5\ 5 \times 10^7$ m/s The corresponding single shot and instrument resolution are $\tau_{dc} = 3\ 3$ ps and $\tau_{instrument} = 3\ 35$ ps, respectively Close agreement between the simulation and the analytical model is found Within the limitations of our models, these results are close enough to satisfy the design specification

\
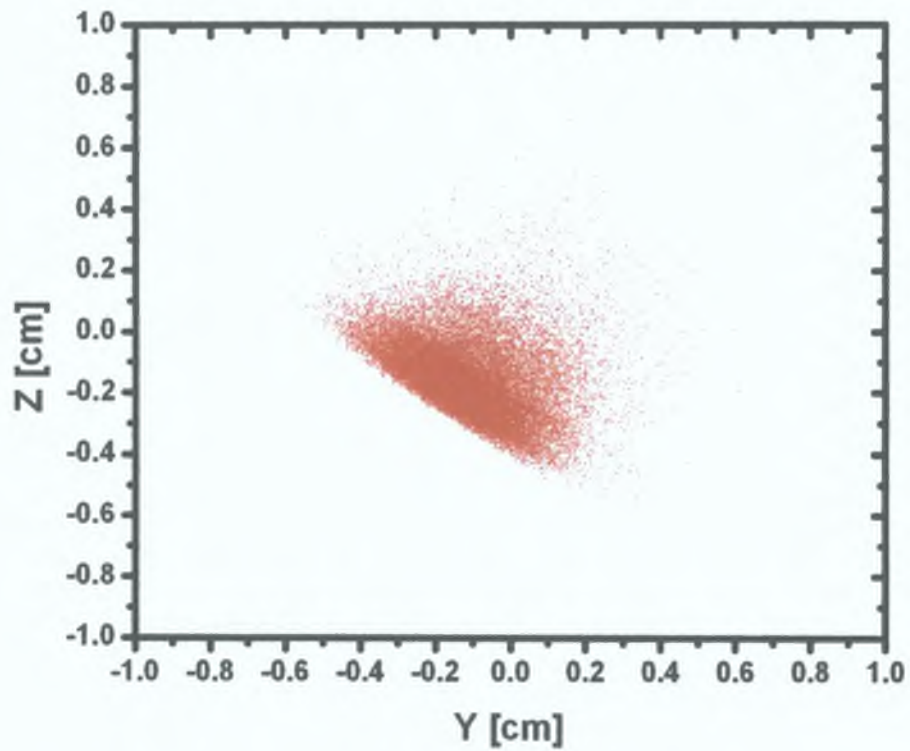
(a) Image.
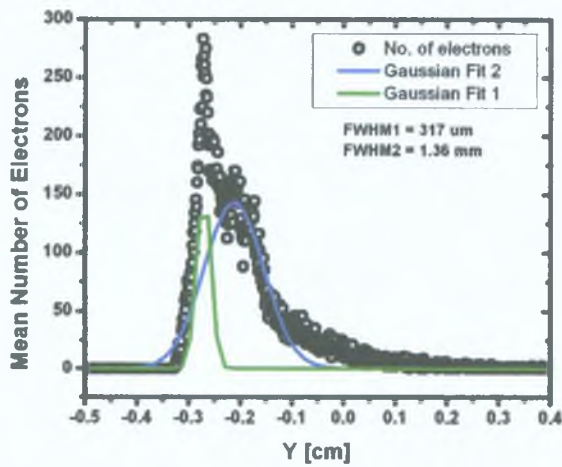
(b) Horizontal lineout.
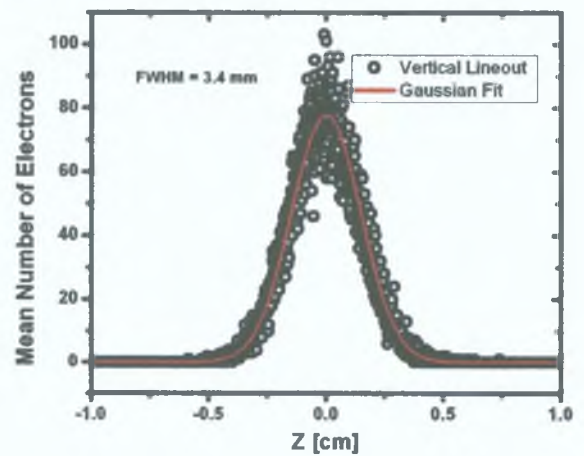
(c) Vertical lineout.

Figure 3.17: (a) Image of electron packet in detector plane after propagating through fixed bias sweep plates. (b) Horizontal and vertical lineouts measuring 317 μm $\times$ 3.4 mm, respectively.

3.4 Mechanical Construction

Having specified the internal components of the streak camera, it is necessary to house them within a structure that is compatible with the mechanical constraints of the design specification Figure 3 18 on page 60 illustrates the design of the camera Two x-ray entrance ports are present in the camera The first, aligned at 30° with respect to the photocathode surface is for spectroscopy applications, whilst the second at 5°, is for single wavelength setups Special emphasis was placed on the design of the spectroscopy port as this had to mate to the beamline such that the photocathode center was 240 mm from the exit of the mirror chamber The complete camera system shown in Figure 3 19 on page 61 was incorporated into the slicing beamline design to verify this specification was met The streak camera also has two laser entrance ports situated on the opposite side of the camera to the x-ray ports These are to facilitate timing fiducials provided by UV pulses derived from the sample pump beam The remaining two ports are mounted at 180° to the x-ray entrance ports By removing the anode-photocathode structure, these ports allow the x-ray beam to propagate through the camera during x-ray alignment procedures One can see that it is relatively easy to change from the spectroscopy configuration to the monochromatic configuration by rotating the camera 90° about the y-axis A high voltage electrical feedthrough is provided for the high voltage photocathode bias An input and an output feedthrough is present for each sweep plate deflection signal The remaining electrical feedthroughs are to facilitate development of a transmission line photocathode structure in the future for sub-2 ns gating The vacuum requirements are satisfied by a vacuum turbo pump / roughing pump combination As the Glaser lens was made from low carbon steel, it was powder coated on the outside to prevent corrosion

The camera was mounted on an optical breadboard as shown in Figure 3 19 The breadboard also provides a mounting base for the photoconductive switch and its associated delay line for timing the sweep pulse to the arrival of the x-rays at the photocathode A Michelson interferometer, with variable delay lines in both arms, enables the production of two pulses with a fixed inter-pulse delay These 800 nm pulses are then converted to 266 nm using standard BBO crystal based tripling optics Thus two timing fiducials can be used in real-time to calibrate the sweep speed and temporal resolution of the camera

The breadboard was mounted on an ALS six strut system (see Figure 3 20, page 62) This system provides kinematic support that enables the detector to be positioned precisely with respect to its six degrees of freedom, translational - x, y, z, and angular - pitch, roll and yaw The struts have ball and socket end connections, and are arranged orthogonally to simplify position adjustments The six struts working together provide very solid support of the equipment They can be easily adjusted and provide positional accuracy in all six degrees of freedom with $\sim 10 \ \mu m$ sensitivity over a generous range of travel [122]
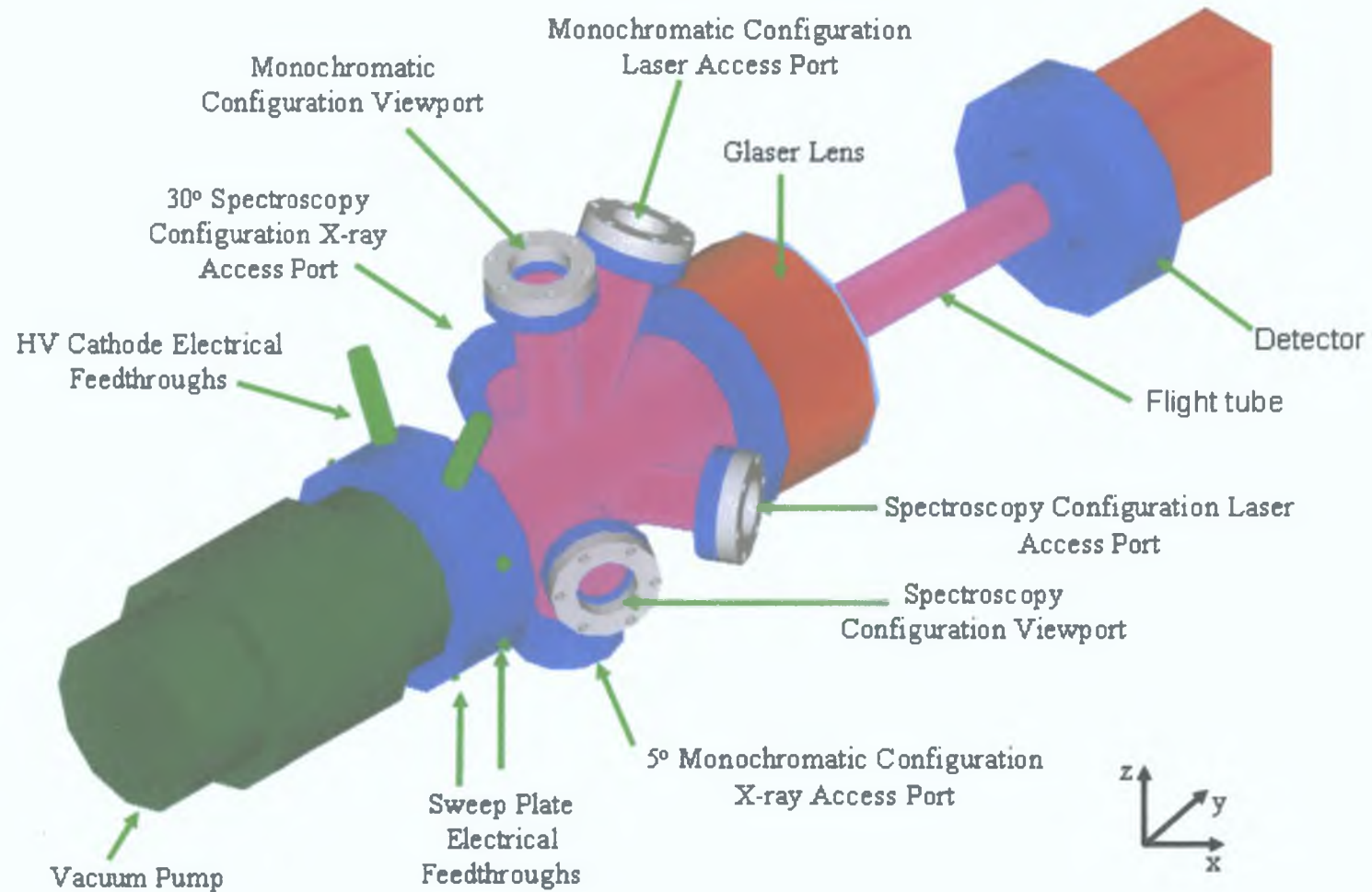
Figure 3.18: Pictorial view of the Grazing Incidence X-ray Streak Camera. Rotating the camera about the y-axis allows rapid change from the 30° spectroscopic configuration to the 5° monochromatic setup. Fixing bolts have been omitted for clarity.
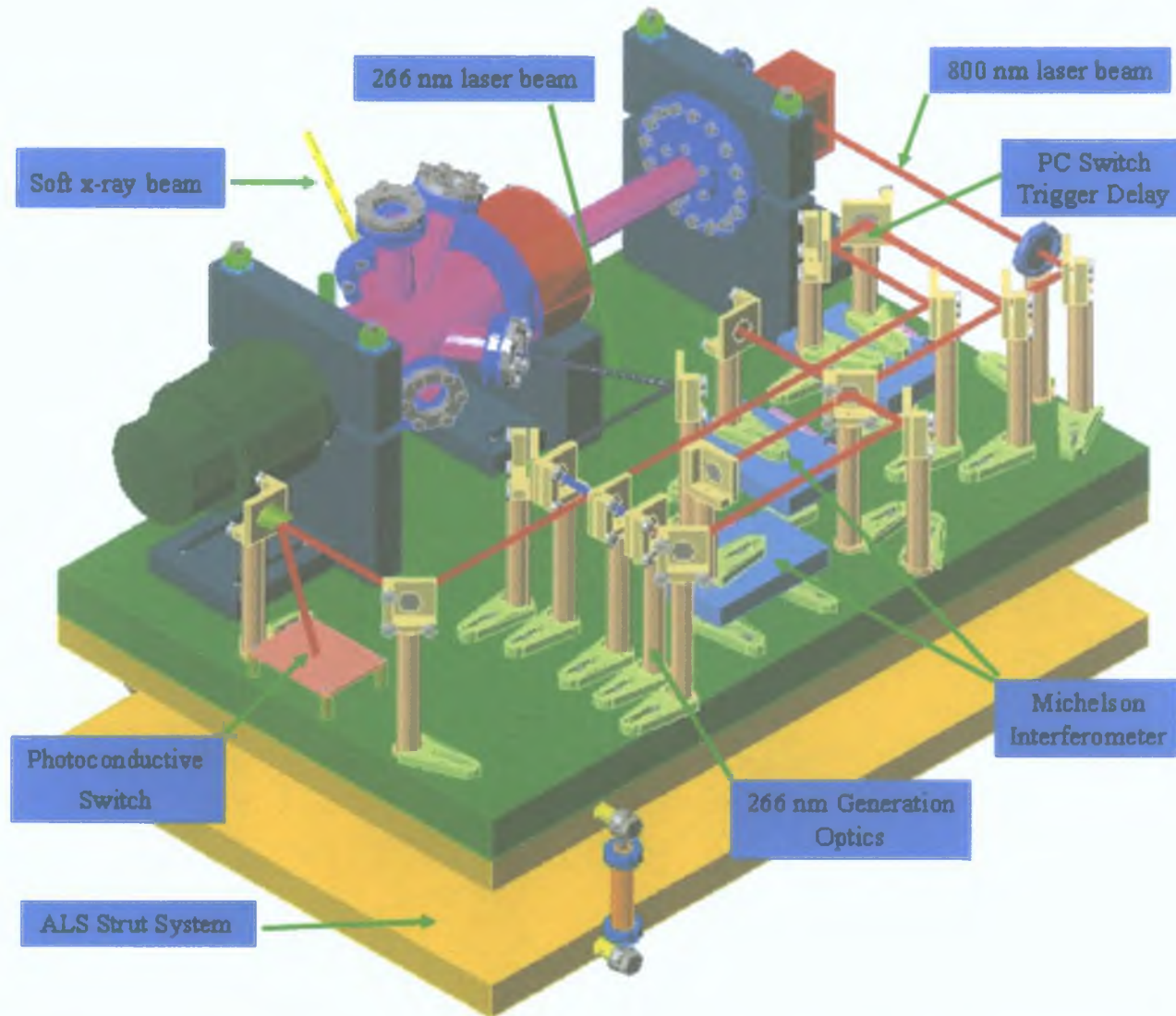
Figure 3.19: Pictorial view of the Grazing Incidence X-ray Streak Camera System mounted on an ALS strut system. Laser and x-ray beam paths are indicated for the spectroscopy configuration. Timing fiducials are generated using a Michelson interferometer.
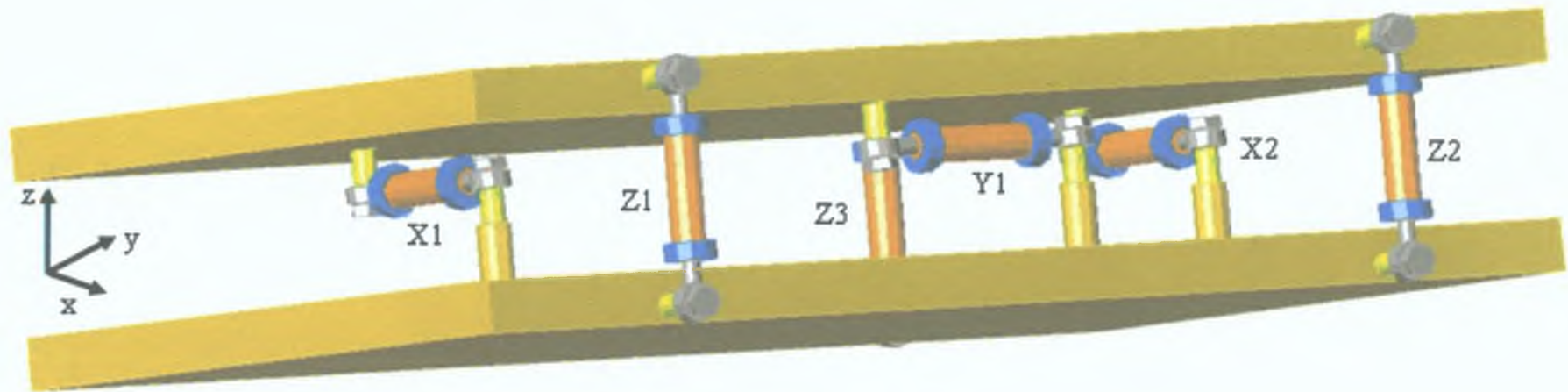
Figure 3.20: ALS 6-strut system. Motion in three dimensions with rotation about all axes is possible by suitable adjustment of the struts.

3.5 Commissioning Experiments

A series of measurements were undertaken to characterise the temporal resolution of the grazing incidence streak camera at ultraviolet and soft x-ray photon wavelengths. The camera tested here deviates slightly from the design model presented earlier. The magnification of the camera was set to 1 55, by shortening the length of the flight tube. Sweep plates with mitred corners optimised for 8 keV electrons were used. When the new geometry was incorporated into the models described earlier, a sweep speed of $v_{sweep} = 2\ 8 \times 10^7$ m/s and temporal resolution of $\tau_{instrument} = 3\ 6$ ps were calculated.

3.5.1 Ultraviolet measurements

Preliminary measurements, specifically aimed at characterising the camera sweep speed and temporal resolution, were performed by exciting a gold cathode with the third harmonic of a Ti Al_2O_3 laser system (266 nm or 4 66 eV). A schematic of the experimental setup is shown in Figure 3 21 on page 64. A $\sim$ 100 fs pulse, with energy $\sim$ 1 mJ and a central wavelength of 800 nm from a Ti Al_2O_3 laser system was incident on a 50/50 beam-splitter. The reflected beam which was passed through a variable delay line was used to trigger the photoconductive switch. The transmitted beam passed through a Michelson interferometer with the delay adjusted to create two pulses separated by 33 ps. To ensure efficient UV generation a telescope was used to match the beam size of the light output from the interferometer to the acceptance aperture presented by the tripling optics. Two BBO crystals either side of a half-wave plate produce the second and third harmonic. A prism, in series with dielectric mirrors optimised for reflection at 266 nm, collected the third harmonic light. This was focused and reflected onto the gold photocathode through the 30° spectroscopy port. To minimise light and electron scatter within the camera a 100 μm slot was inserted after the anode. This also provided a clear aperture to define the static image. The sweep speed and temporal resolution of the camera were measured in accumulation mode taking an average of 100 shots at 1 kHz repetition rate. An Andor Peltier-cooled back illuminated CCD with a pixel size measuring 13 μm by 13 μm was used for direct detection of the electron bunch.

The result of the measurement is shown in Figure 3 22 on page 65. A sweep speed $v_{sweep\,UV} = 3\ 5 \times 10^7$ m/s and a temporal resolution $\tau_{instrument\,UV} = 5$ ps was recorded. Gold has a work function $\phi_{Au} \approx 4\ 5$ eV, thus single photon electron emission is possible with 266 nm laser light. In contrast, cesium iodide, with a work function of $\phi_{CsI} \approx 6\ 1$ eV, requires multi-photon excitation. As the electrons are being promoted from the Fermi level, the energy distribution will be on the order kT, where k is Boltzmann's constant and T the cathode temperature. This is significantly smaller than the secondary electron
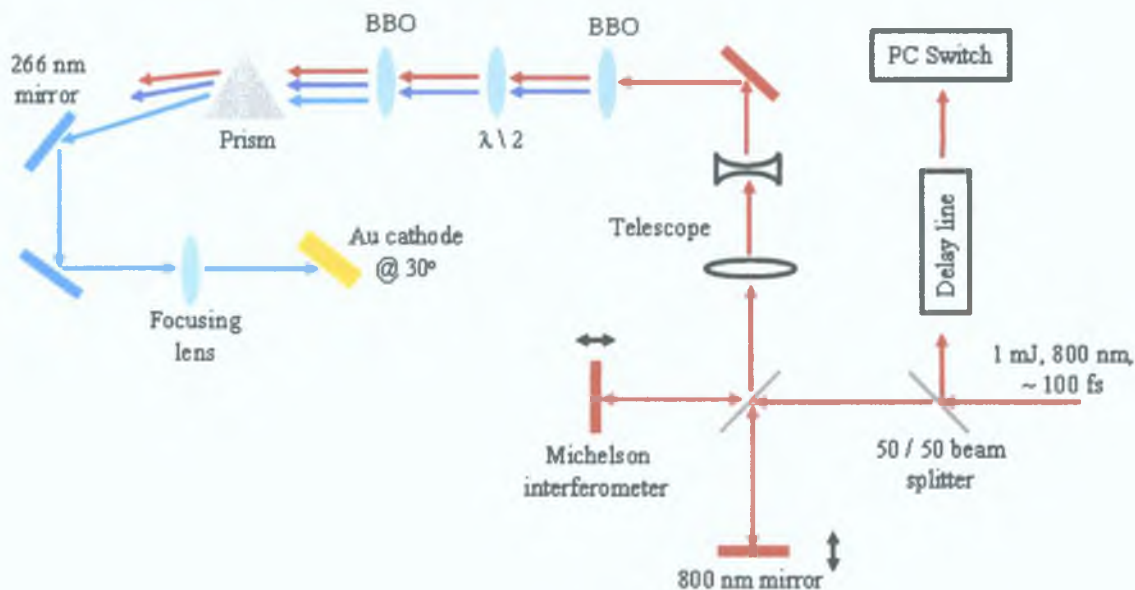
Figure 3.21: Experimental setup to test the camera sweep speed and temporal resolution using the third harmonic of a Ti:Al$_2$O$_3$ laser.

energy distribution resulting from excitation with x-rays; for gold this is typically 3.8 eV [91]. Thus the measured temporal resolution is not affected by electron chromaticity induced temporal dispersion. Measurements were performed over a range of incident laser intensities. No difference in the temporal resolution was observed, indicating that space charge contributions were also negligible. The timing jitter for the photoconductive switch used in this measurement was estimated to be $\tau_{jitter} \approx 1$ ps. Performing a quadratic deconvolution of the timing jitter from the measured temporal response still yields a single shot resolution $\tau_{dc\,UV} \approx 5$ ps. This implies the sweep speed is the limiting factor. Given the relative simplicity of the analytical models employed in the camera design and the lack of a full time-dependent simulation, remarkable agreement between model/simulation and measurement has been obtained.

3.5.2   Soft x-ray measurements

Characterisation of the streak camera, setup in a spectroscopy configuration, with sliced femtosecond and unsliced picosecond x-ray pulses was performed at beamline 5.3.1 at the Advanced Light Source [143]. The general configuration of the beamline for this measurement is similar to the soft x-ray branch of the slicing beamline under development. An overview of the setup is shown in Figure 3.23 on page 66. Radiation was collected from a bend magnet source by a platinum-coated toroidal mirror set at a grazing angle of 5 mrad. A 1:1 image of the source, measuring 170 μm horizontally and 250 μm vertically, was formed 24 m downstream. The high average power of the x-ray beam was
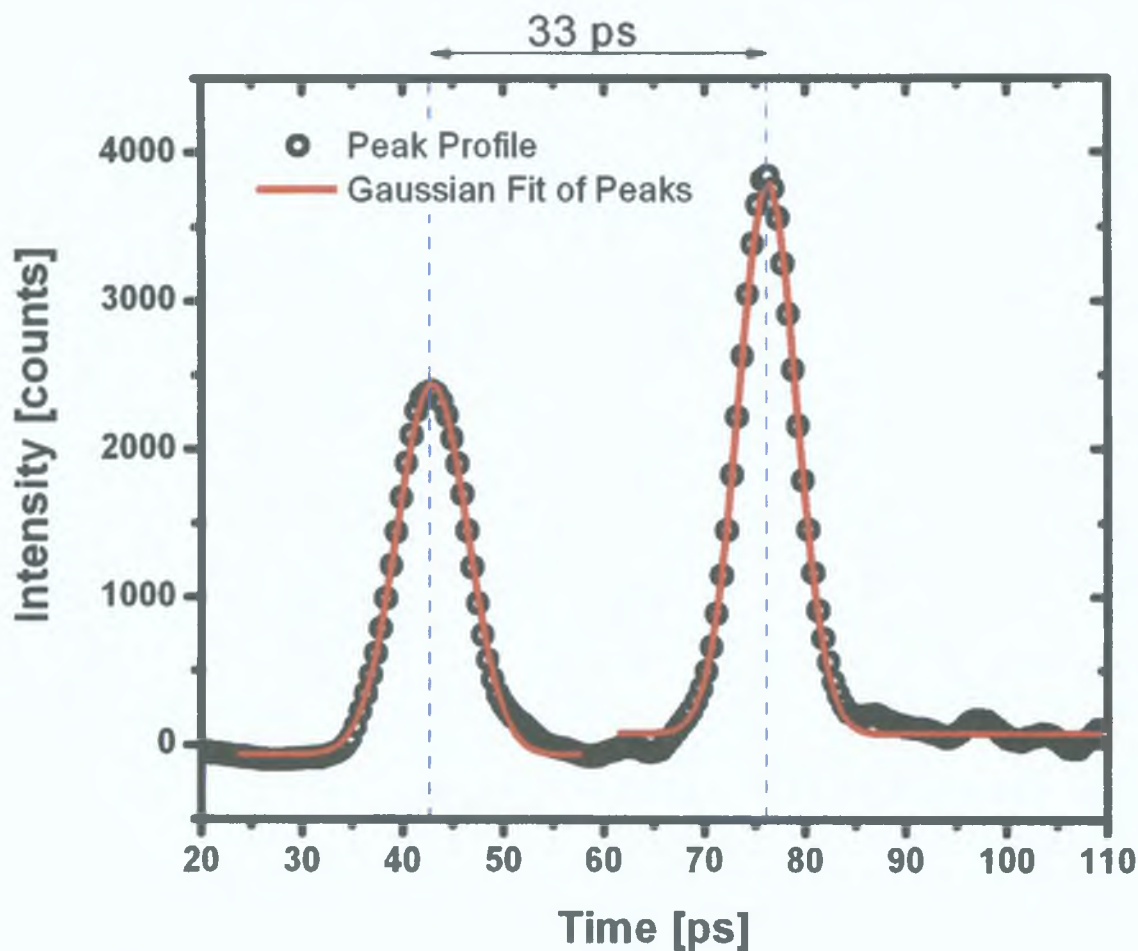
Figure 3.22: Sweep speed and temporal resolution of streak camera characterised with UV pulses: $v_{sweep\,UV} = 3.5 \times 10^7$ m/s and $\tau_{instrument\,UV} = 5$ ps. The difference in the intensity in the two pulses is due to a lower reflectivity from one of the mirrors in the Michelson interferometer.

removed using a chopper running at 1 kHz. A pair of slits were placed at the x-ray beam focus. These served the dual purpose of acting as the entrance slit to the spectrometer and discriminating the unsliced picosecond background during the slicing measurements. A careful measurement of the x-ray beam profile in the horizontal plane was undertaken as background scatter from beamline optics needs to be sufficiently suppressed to obtain a measurable sliced signal. The spectrometer, employing a 600 line/mm gold coated variable line spacing grating and two curved refocusing mirrors, formed an erect image of the slit spectrum on the streak camera photocathode. No harmonic suppression mirrors were used in the setup. Thus the energy spectrum passed by the spectrometer contains the fundamental plus harmonics with photon energy less than 2 keV, the upper limit being set by the reflectivity of its constituent mirrors. A cesium iodide cathode was used for these measurements as it has superior efficiency and secondary electron energy distribution characteristics over gold for soft x-ray applications. The cathode was aligned to the

incident x-ray beam using the ALS strut system. A single microchannel plate was used to single out and amplify the electrons associated with the camshaft pulse. The MCP was triggered by a DEI PVM-4140 high voltage pulser at -1 kV with a 60 ns gate width. Electrons emerging from the rear of the MCP were accelerated toward and impacted upon a phosphor screen biased at +2.5 kV with respect to the grounded MCP output. The resulting photons were fibre coupled to an optical water-cooled Photometric CH350 CCD with a pixel size of 19 μm. To further improve signal to noise, data binning with a 2 $\times$ 2 superpixel was used. All data presented here was collected in accumulation at mode 1 kHz repetition rate. The photoconductive switch was triggered with pulse energies of 40 μJ. Timing of the sweep to the x-ray pulse arrival was accomplished with a variable optical delay line. Having described the general experimental configuration, details of the specific characterisation measurements and their results follow.
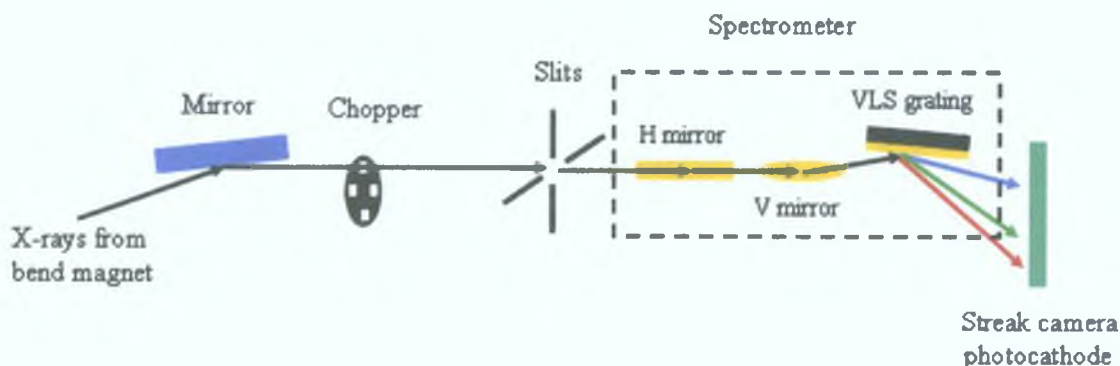
Figure 3.23: Experimental setup to test the grazing incidence x-ray streak camera at the ALS beamline 5.3.1.

The streak camera imaging optics were tested statically by imaging the electron beam passing through a 100 μm slit downstream of the anode. The slit provides a defined aperture for the electron beam, thus facilitating accurate determination of the camera lens magnification. This measurement was performed with the spectrometer first set to zero order. The entrance slits were set to 250 μm $\times$ 250 μm and centered on the picosecond intensity maximum. At zero order, the grating behaved like a plane mirror, projecting an incident spot on the cathode measuring 540 μm along the vertical axis. The magnification of the vertical entrance slit by $m_{spec\,v} = 2.16$ is due to the vertical spherical refocusing mirror. The recorded static image, of dimension 152 μm horizontal by 836 μm vertical, is shown in Figure 3.24 on page 67. This implies a camera lens magnification $m = 1.52$, which is in excellent agreement with theory.
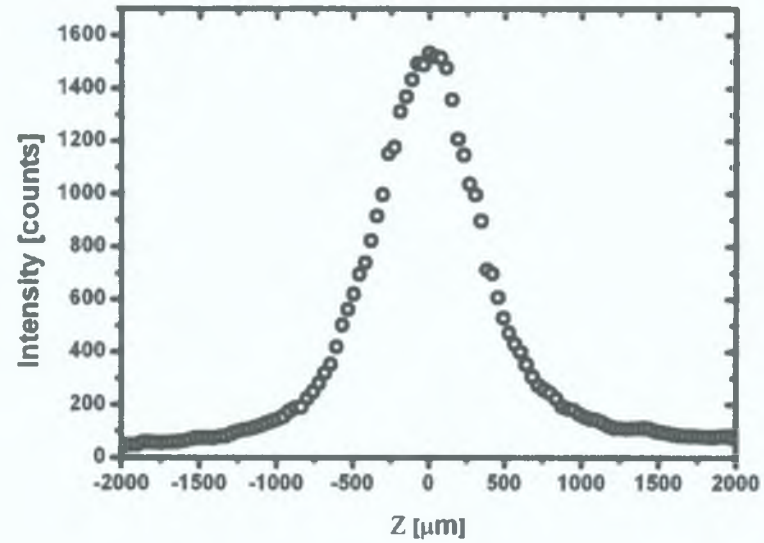
(a) Vertical lineout.
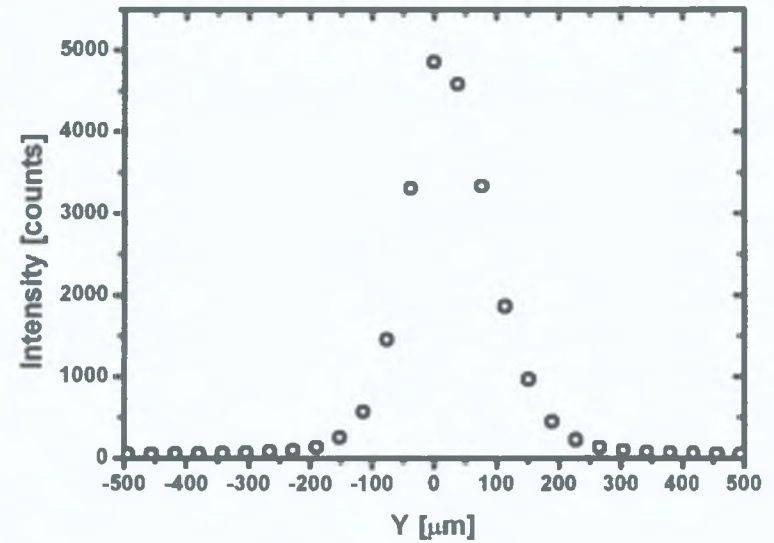
(b) Image.

(c) Horizontal lineout.

Figure 3.24: Static image of 100 μm slit with photocathode illuminated by zero order light from spectrometer. Horizontal and vertical lineouts of the image, measuring 836 μm by 152 μm, respectively. Data shown is the average of 3×10^4 shots.

A first order static spectrograph of the beamline intensity incident on the cathode at the cesium M_4 edge (740 5 eV), with an energy resolution $\Delta E = 12\ 8$ eV, can be seen in Figure 3 25 on page 69 Sharp energy resolution was forgone in favour of increased photon throughput One can see that the image remains in focus over most of the spectral range, whose dimension on the CCD measured ~ 11 mm Thus off-axis spherical aberrations caused by the Glaser lens are minimal In the unswept direction, the horizontal lineout measures 152 μm as expected

Streaking was also carried out with zero and first order images projected onto the cathode The data is shown in Figures 3 26 on page 70 and 3 27 on page 71, respectively For the zero order data the spatial axis remained in focus over the sweep duration and it measures the same extent as in the unswept image (cf Figures 3 24 (a) and 3 26 (a)) However, imaging deviations are observed for the swept spectrum (cf Figures 3 25 (b) on page 69 and 3 27 (b) on page 71) This has been attributed to slight defocussing of the lens over the duration of the exposure It is also possible that an inhomogeneous sweep field is exacerbating this problem However, if the sweep field alone were responsible for the poor image quality, then one would expect to see a region in the image center exactly in focus (similar to Figure 3 25 (b)) as this corresponds to the zero field crossing That this is not the case, emphasises the lens defocusing hypothesis Spectrograph lineouts at two different time delays are presented in Figure 3 27 (a) A lower intensity, attributable to the intensity temporal profile of the camshaft pulse, is observed at $t = 25$ ps compared to $t = 0$ ps Both spectra show the same features within the noise level of the data

Whilst the imaging inhomogeneities complicate the fit for the spectroscopy data, with respect to the temporal axis both data sets measure the duration of the camshaft pulse $\tau_{camshaft} = 70$ ps FWHM The sweep speed was calibrated directly from the swept zero order image As the duration of the camshaft pulse ($\tau_{camshaft} = 70$ ps) is significantly greater than the temporal resolution of the camera, $\tau_{instrument\,UV} = 5$ ps from the UV measurement, to first order the temporal resolution is given by

$$\tau_{instrument} = \frac{w_{unswept}}{w_{swept}} \tau_{camshaft} \quad , \tag{3 29}$$

where $w_{unswept}$ and w_{swept} are the measured widths of the unswept and swept images on the detector, respectively This analysis yields a temporal resolution of $\tau_{instrument\,x-ray} = 6$ ps For the anode-photocathode configuration used, the secondary electron chromaticity temporal dispersion contribution has been estimated at $\tau_{pc-a} = 1\ 2$ ps Photoconductive switch related jitter is $\tau_{jitter} \approx 1$ ps Neglecting space charge contributions due to the low x-ray fluxes involved and performing a quadrature subtraction, the measured instrument resolution implies a single shot temporal resolution $\tau_{dc\,x-ray} = 5\ 8$ ps The corresponding sweep speed is $v_{sweep\,x-ray} = 2\ 7 \times 10^7$ m/s Whilst these figures are close to the values

68
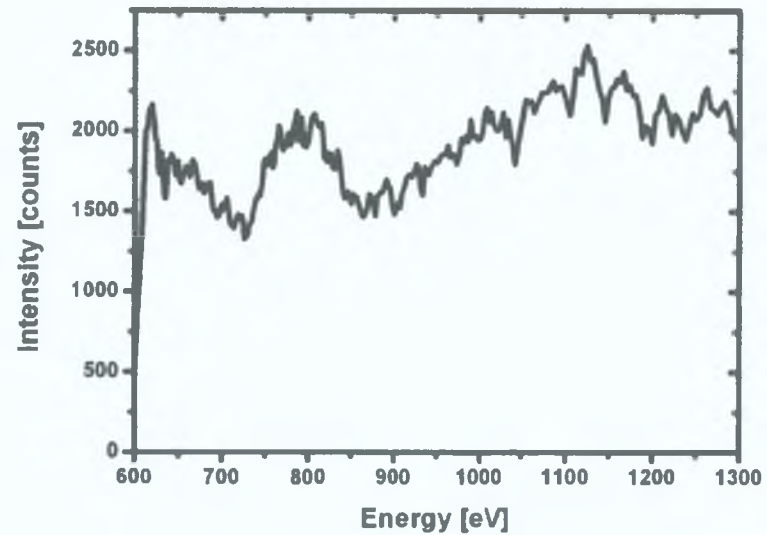
(a) Vertical lineout.
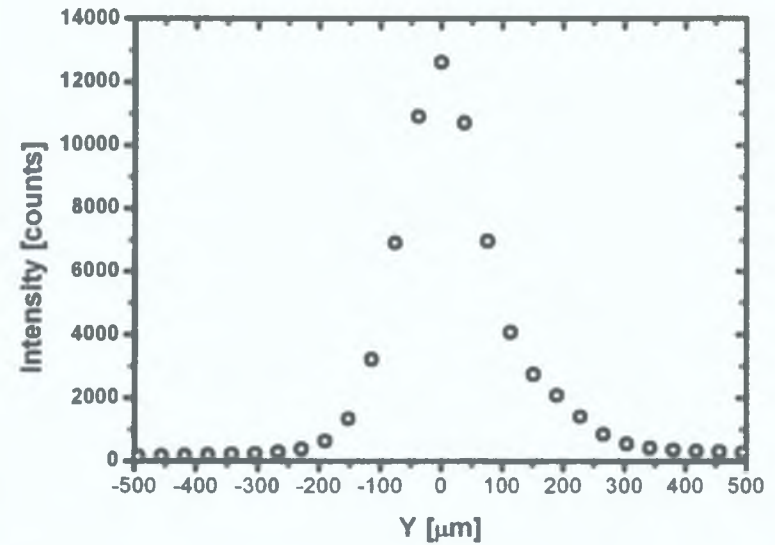
(b) Image.

(c) Horizontal lineout.

Figure 3.25: Static spectrograph about Cs M_4-edge (740.5 eV) and lineouts of the image along the energy and unswept axes. Data shown is the average of 2×10^5 shots.
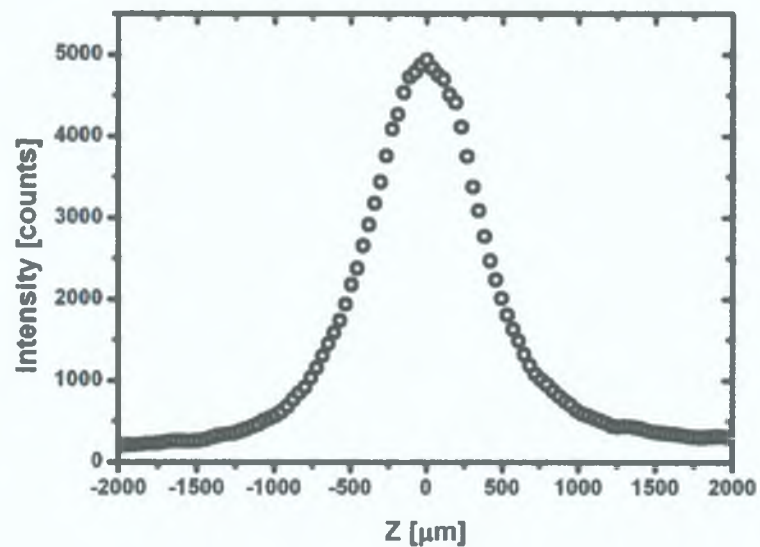
(a) Vertical lineout.
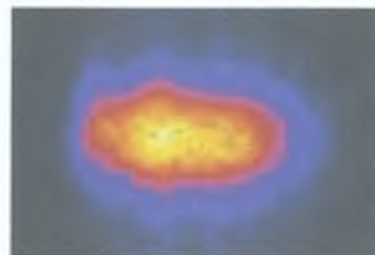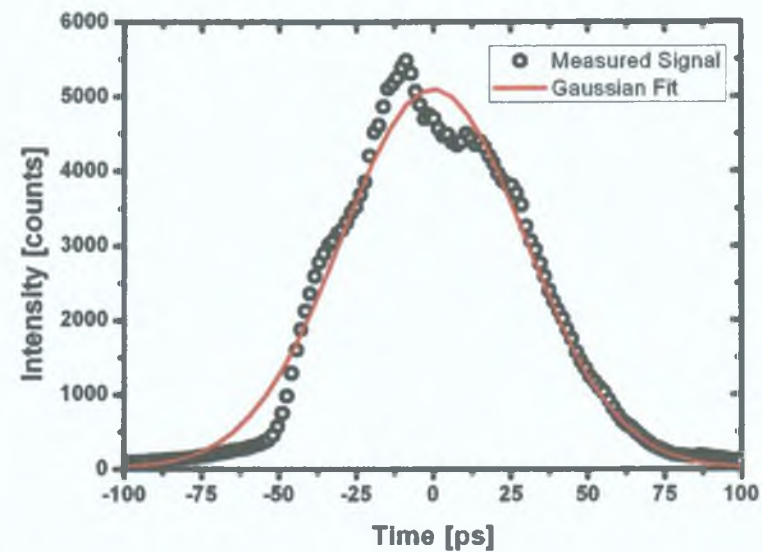
(b) Image.

(c) Temporal lineout.

Figure 3.26: Swept image of spectrometer zero order output and lineouts of the image along the spatial and temporal axes. The vertical lineout measures 836 μm. Data shown is the average of 6×10^4 shots.
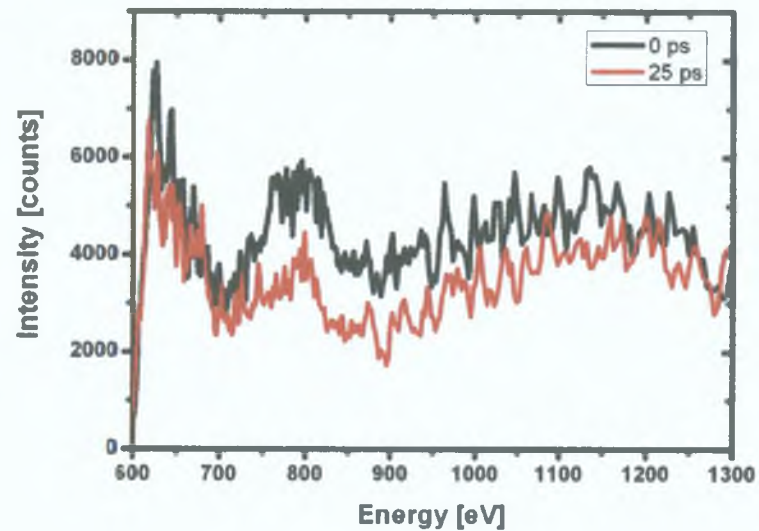
(a) Energy lineout.
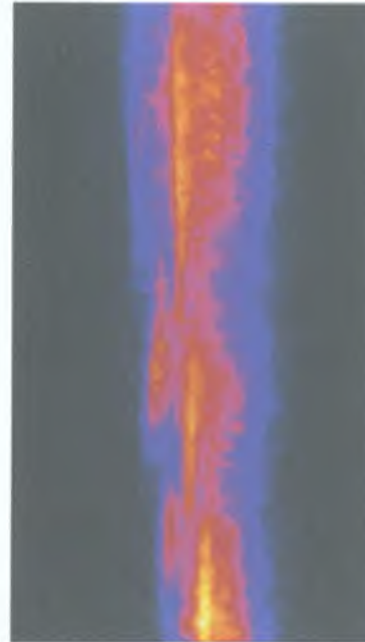
(b) Image.
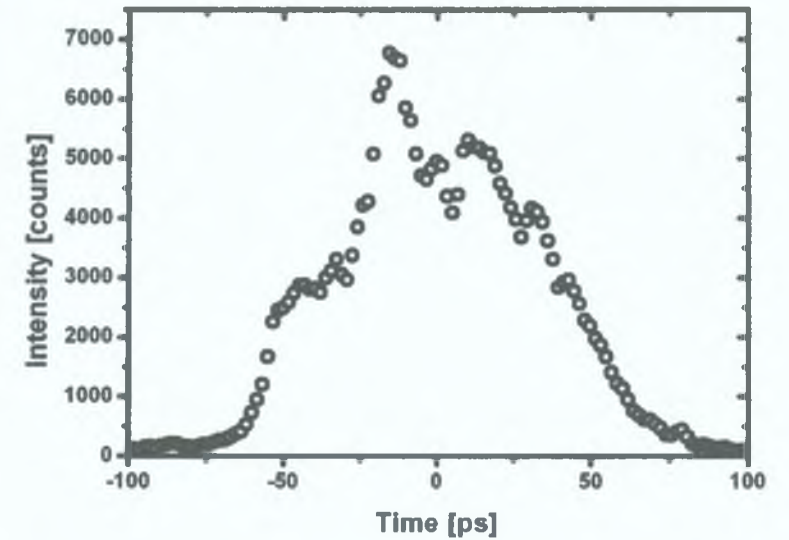
(c) Temporal lineout.

Figure 3.27: Swept spectrograph about Cs M_4-edge. Lineouts of the image at an energy $E = 1100$ eV and times $t = 0$ ps, $t = 25$ ps. Data shown is the average of 3×10^5 shots.

reported for the ultraviolet measurement, they do not agree precisely. The difference may be attributed to differences in the photoconductive switch used for the two measurements.

It was not possible to generate UV timing fiducials in-situ during the measurement due to low laser output power. However, a second measurement was undertaken to attempt to calibrate the temporal resolution. The delay line upstream of the photoconductive switch was changed by an amount corresponding to 10 ps. The resulting displacement of the swept image peak was measured. From this a sweep speed $v_{sweep\,x-ray} = 3.6 \times 10^7$ m/s was ascertained. Even though this value agrees with the value obtained from the UV measurements, some caution should be exercised as the shape of the streaked image changed with the time delay. A reduction in peak height was noticed, suggestive of electron beam clipping at the sweep plate output. Thus the true displacement could have been somewhat larger, implying a slower sweep speed. The data, shown in Figure 3.28, was recorded during the slicing measurements explained below, hence the reason for the poorer signal to noise ratio.
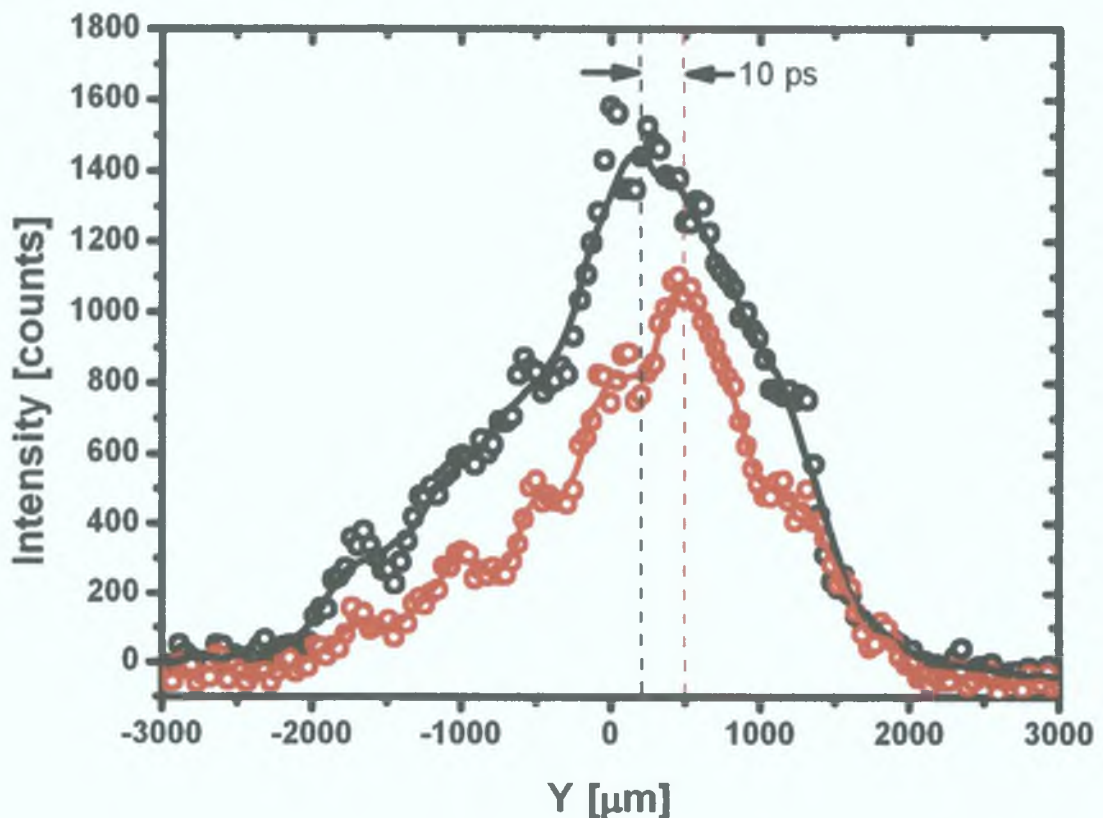
Figure 3.28: Sweep speed calibration by delaying sweep with respect to x-ray pulse arrival. A 10 ps delay of the sweep trigger caused a displacement of the peak by 360 μm. The experimental data has been smoothed with a 10 point adjacent averaging filter.

Sliced photons with duration $\sim$ 170 fs were produced in the manner described earlier The slicing process was optimised and the pulse duration inferred by monitoring the resulting coherent synchrotron radiation Sliced photons were collected by displacing the slits, with a 100 μm opening, 400 μm from the picosecond maximum The spectrometer was set to zero order to increase throughput A difference measurement was performed to clearly accentuate the detection of sliced photons with the camera A swept image was first recorded with the modulating laser beam blocked by a beam dump and immediately followed with a slicing exposure Temporal lineouts of the individual exposures and the difference signal can be seen Figure 3 29 (a) and (b) on page 74, respectively The slicing on lineout clearly shows increased intensity over the unsliced signal As the slicing data was recorded after the unsliced data, intensity differences due to the decay of the storage ring current cannot be attributed to the enhanced difference signal shown Therefore the camera clearly resolves the presence of sliced photons The ratio of sliced photons to unsliced photons should be $\sim$ 3 1 with the slicing process occurring at the intensity maxmimum of the camshaft pulse Whilst the difference signal is centered on the maximum at $t = 0$ ps, an integrated intensity ratio of 0 14 1 (sliced to unsliced) was recorded An even more worrying feature of the recorded data is the measured difference signal FWHM of 20 ps Based upon the previous measurements, one would have expected the impulse response of the camera to measure $\tau_{instrument\ sliced} \approx 6$ ps However, our result clearly shows an additional broadening mechanism of duration $\sim$ 19 ps

To date we have attempted unsuccessfully to clearly ascertain the source of the broadening mechanism From the coherent synchrotron radiation spectral measurements, we believe the slicing interaction was correct Our current hypothesis attributes the poor temporal resolution to misalignment of the x-ray optics Figure 3 30 on page 75 depicts the measured horizontal spatial profile of the x-ray beam at the entrance slits to the spectrometer For a perfect mirror the scatter should be Gaussian in nature However, surface roughness causes deviations from ideal behaviour For the Pt-coated mirror used to image the synchrotron radiation, one would have expected the normalised scatter to be 10^{-4} the peak value, 400 μm from the peak A slightly higher value of 5 6 $\times$ 10^{-4} has been measured In principle, this should have only reduced the sliced to unsliced contrast, a point borne out in the experimental data Temporal resolution should not have been affected The photocathode was situated approximately 1 m downstream of the grating and this lead to a magnified image of the spectrometer source In previous streak camera measurements, the detector was situated closer to the grating resulting in a demagnified image [119] Thus a combination of the mirror scatter and spectrometer magnification may account for some of the measured dispersion Another source of broadening may have come from the photocathode itself If the cathode were tilted about the unswept axis, then sliced photons produced at the same instant in time but spatially separated in the same plane would
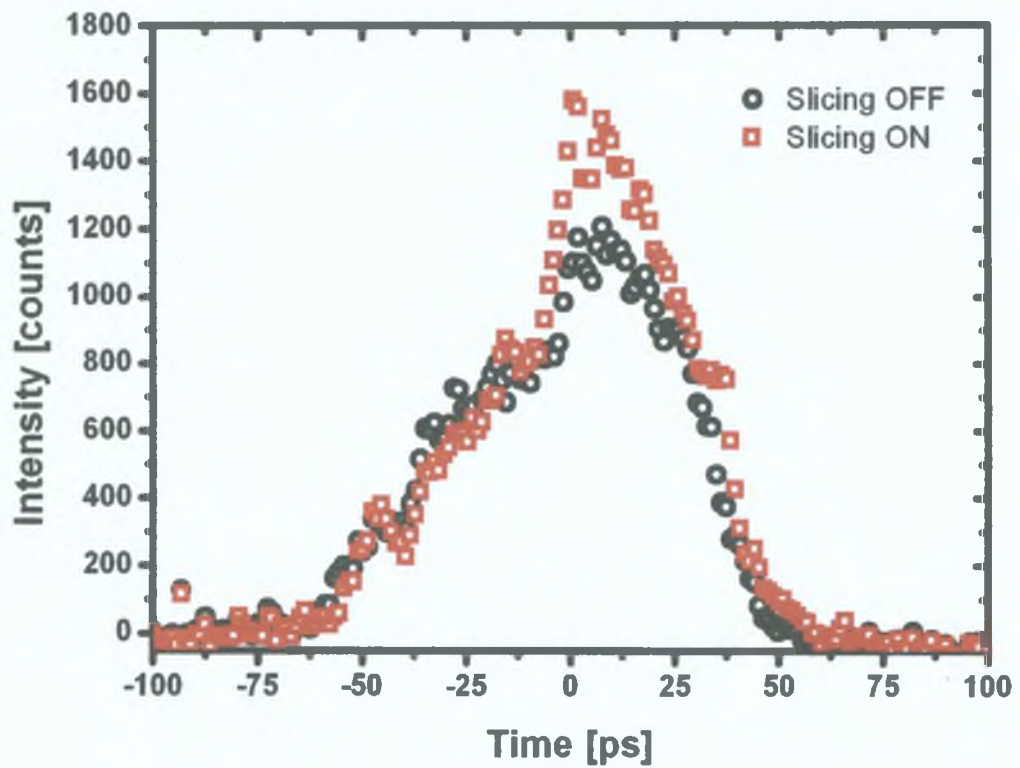
(a) Temporal lineouts.
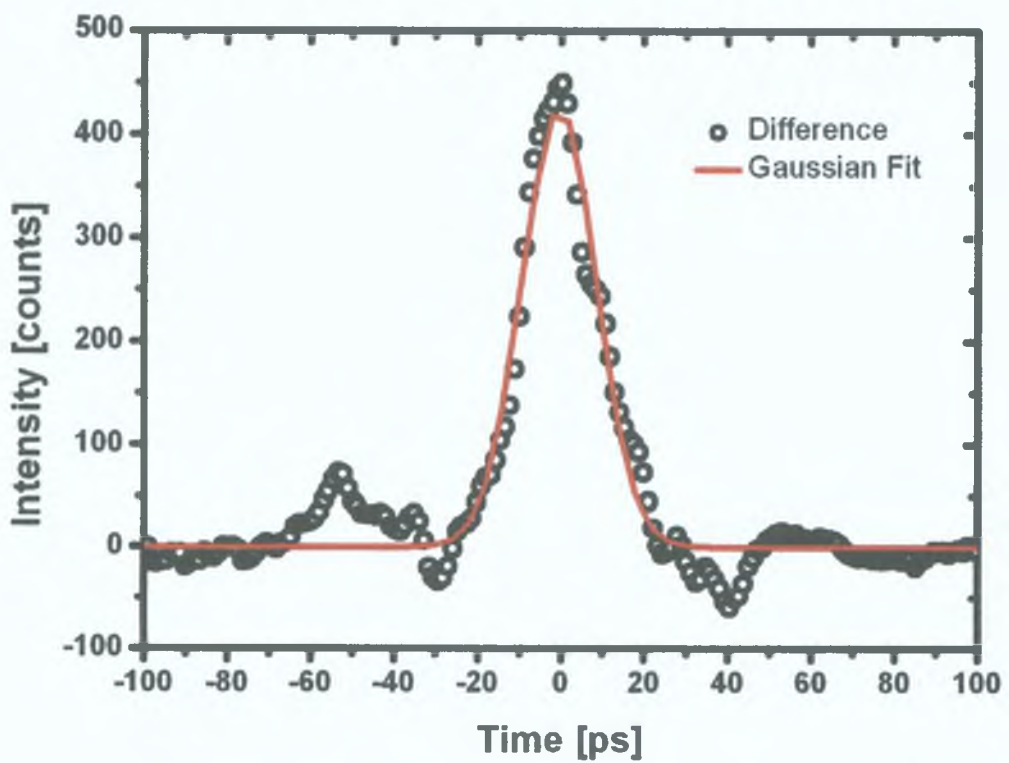
(b) Difference signal.

Figure 3.29: Slicing data recorded at 4σ with 100 μm slit. (a) Temporal lineouts with slicing on and off. (b) Difference signal measuring 20 ps FWHM.

strike the cathode at different times. For the geometry employed, this would suggest that the cathode was tilted 10° away from the perpendicular to the incident beam. Whilst an accurate measurement was not taken, visual inspection of the experimental setup would seem to discount this hypothesis. This theory is further supported by the experimental data. By examining the streaked data along subsets of the spatial axis, one would have expected to see a shift in the position of the sliced peak progressing from the top of the image toward the bottom. This is not observed indicating the cathode was normal to the x-ray beam. Further commissioning experiments with the slicing setup are necessary.
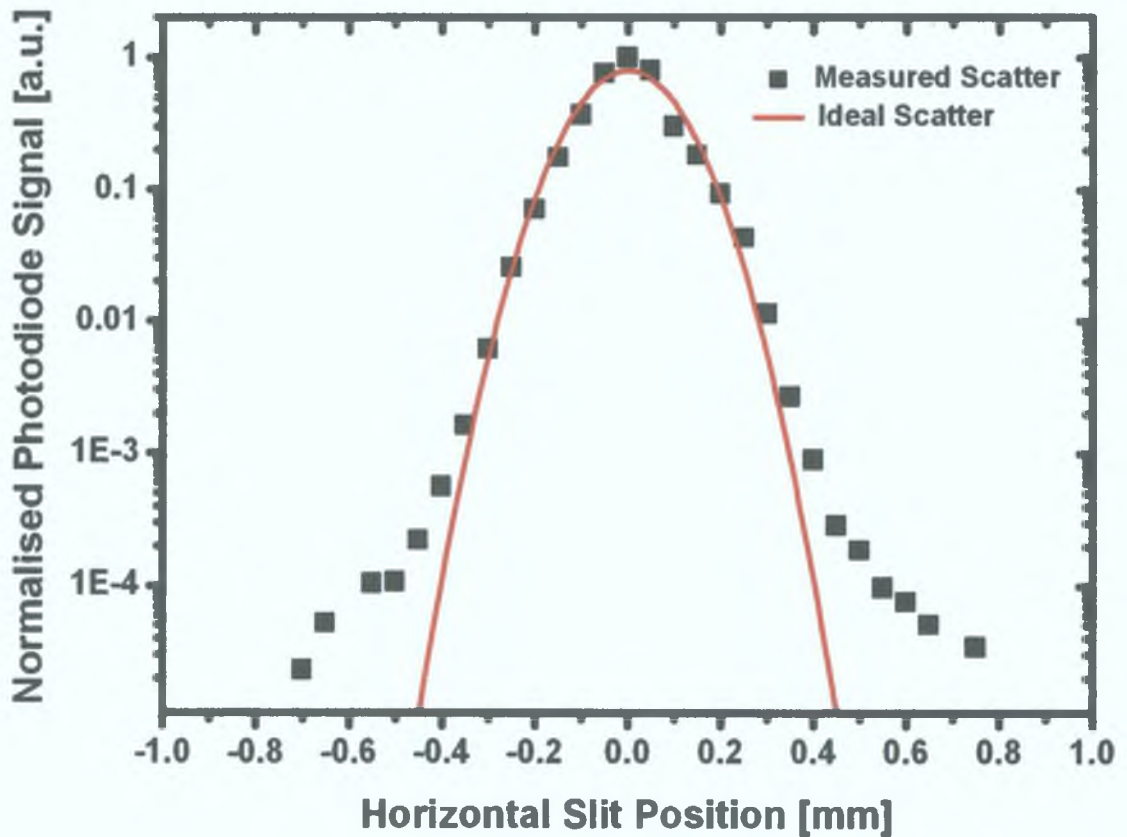
Figure 3.30: Horizontal spatial profile of x-ray beam. The ideal Gaussian measures 220 μm FWHM.

3.6 Conclusions

A grazing incidence streak camera has been developed to compliment the slicing program at the Advanced Light Source. A rigorous analysis of all camera sub-systems was undertaken. Given the level of simplification, the analytical model has demonstrated excellent agreement with the full particle simulation and all measurement results except slicing. The camera demonstrated a temporal resolution of $\tau_{instrument} = 6$ ps. Further improve-

ments to the camera are necessary to push this to the desired resolution of 1 ps The modeling strategy developed thus far will certainly be beneficial in this respect Obvious areas for improvement are the sweep plate design and the anode-photocathode electric field The camera clearly illustrated that it was sensitive to the slicing process Our ability to clearly distinguish difference signals with low contrast compared to that expected by an optimised slicing experiment should be viewed optimistically, as the UV measurements clearly confirm the camera can respond to femtosecond photonic signals Thus one can anticipate with confidence that the camera is capable of performing its intended function In conclusion, the constructed camera has come close to satisfying all the requirements of the design specification and the necessary improvements to achieve said aims should be realised in the near future

Acknowledgments

Chapter 4

Time-resolved measurements of the structure of water at constant density

4.1 Introduction

Liquid water undergoes continuous structural rearrangements on picosecond time scales, involving rapid breaking and reforming of the hydrogen bonds which make up the backbone of its structure [144, 145] The ability of water to form transient hydrogen bond networks is intimately tied to many of its most important properties, including many of its anomalous ones, becoming more compressible and expanding upon cooling and becoming less viscous under compression at low enough temperatures [146] The existence of a density maximum as a function of temperature, for example, may be interpreted as the result of competing effects between the normal tendency of liquids to expand on heating opposed by the breaking of hydrogen bonds associated with low-density "icelike" configurations [147]

As reviewed in Chapter 1 a wide range of experimental and theoretical techniques have been applied toward understanding the structural and dynamical effects which underly much of water's unusual behavior X-ray scattering techniques [45, 46, 48], through measurement of the liquid structure factor, may be used to extract pair correlation functions which describe the average local structure in the liquid state Here we describe first steps toward applying time-resolved diffraction techniques [85], with temporal resolution approaching that of the time scale for molecular rearrangement, to the problem of liquid water By comparison with static temperature-dependent measurements, it is shown that the observed short time-scale effects (times less than typical expansion times but greater than hydrogen-bond lifetimes) can be understood in terms of temperature-induced changes in the structure of water occurring at constant volume, before the system has had time to expand Before we describe the experiment and the results in more detail a brief digression is made to introduce a kinematical theory of x-ray scattering from liquids

77

4.2 X-ray Scattering from Liquids

The kinematical theory of x-ray diffraction is employed to determine the scattering of x-ray photons by a liquid The analysis presented here is principally derived from [148] and [149] It will be shown that the scattered signal consists of two components an intramolecular contribution from individual water molecules and an intermolecular component due spatial correlations in the liquid arising from density fluctuations Typical kinematical theory approximations are employed These are the plane wave approximation and an assumption of coherent small amplitude scattering [150] A kinematical treatment is sufficient for weakly scattering or disordered samples

Consider the interaction of a photon with an isolated electron with elemental charge e and mass m_e The photon is represented by a plane wave with wavelength λ, corresponding wavevector $|\vec{k_0}| = 1/\lambda$ and frequency ν_0 For simplicity, the electron is located at the origin of the co-ordinate system It is assumed that no forces act on the electron other than that arising from the photon electric field and this force is sufficiently weak that the particle does not move relativistically The oscillating electric field may be written as

$$\vec{E}(\vec{r}, t) = \vec{E_0} e^{i2\pi(\nu_0 t - \vec{k_0}\,\vec{r})} \tag{4 1}$$

Therefore, the electron is subject to a force

$$\vec{F}(\vec{r}, t) = -e\vec{E}(\vec{r}, t) \tag{4 2}$$

From Newton's laws of motion, the electron acquires an acceleration

$$\vec{a}(\vec{r}, t) = \frac{-e}{m_e}\vec{E}(\vec{r}, t) \quad , \tag{4 3}$$

and its displacement is given by

$$\vec{d}(\vec{r}, t) = \int \int \vec{a}(\vec{r}, t) dt = \frac{e}{4\pi^2 \nu_0^2 m_e}\vec{E}(\vec{r}, t) \tag{4 4}$$

The resulting dipole moment is

$$\vec{M_0} = -e\vec{d}(\vec{r}, t) = \frac{-e^2}{4\pi^2 \nu_0^2 m_e}\vec{E}(\vec{r}, t) \tag{4 5}$$

Such an oscillating dipole, according to classical electrodynamics, produces its own propagating electromagnetic wave i e the scattered wave At large displacements $\vec{R}$ from the

dipole, the electric field of the scattered radiation is given by [151]

$$\vec{E}_e(\vec{R}, t) = \frac{Z_0 \nu_0^2}{4\pi c |\vec{R}|} e^{-i2\pi(\nu_0 t - \vec{k} \cdot \vec{R})} \left[\left(\vec{n} \times \vec{M}_0 \right) \times \vec{n} \right] \quad , \tag{4 6}$$

where $Z_0 = \sqrt{\mu_0/\epsilon_0}$ is the impedance of free space, μ_0 is the permeability of free space, ϵ_0 the permittivity of free space, c the speed of light, $\vec{k}$ the wavevector of the scattered wave and $\vec{n} = \vec{k}\lambda$ is a unit vector in the scattering direction

The scattering from a single electron is now extended to an atom with Z electrons whose nucleus is assumed to be at the origin As only the Z electrons of the atom contribute significantly to the X-ray scattering process, by ignoring the interaction between the electrons, one can determine the total scattered electric field by simply adding the scattered fields from each of the individual electrons

$$\vec{E}_{at}(\vec{R}, t) = \frac{Z_0 \nu_0^2}{4\pi c} \sum_{j=1}^{Z} \frac{1}{|\vec{R}_j|} e^{-i2\pi(\nu_0 t - \vec{k}_j \cdot \vec{R}_j)} \left[\left(\vec{n}_j \times \vec{M}_j \right) \times \vec{n}_j \right] \quad , \tag{4 7}$$

where the index j refers to a particular electron within the atom The dipole moment from the jth electron, located at position $\vec{r}_j$ is given by

$$\vec{M}_j = \vec{M}_0 e^{-i2\pi \vec{k}_0 \cdot \vec{r}_j} \tag{4 8}$$

If the distance from the nucleus to the point of observation is much larger than that from the nucleus to any of the electrons, the distances $|\vec{R}_j|$ can be replaced by an average R, the wave vectors $\vec{k}_j$ with an average $\vec{k}_H$, and the unit vectors $\vec{n}_j$ with an average $\vec{n}$ In the exponential, the phase relationship must be preserved as the displacements $\vec{r}_j$ between electrons are of the order of the wavelength of the incident radiation Consequently, Equation (4 7) reduces to

$$\vec{E}_{at}(\vec{r}, t) = \vec{E}_e \sum_{j=1}^{Z} e^{-i2\pi(\vec{k}_H - \vec{k}_0) \cdot \vec{r}_j} \tag{4 9}$$

Due to the Heisenberg uncertainty principle, it is not possible to know the exact position of an electron at a specified time Therefore we should represent the presence of each electron in the atom by its probability density p_j so that $p_j d\tau$ represents the probability of finding the electron j within a volume $d\tau$ The scattering of the incident electromagnetic radiation by all the electrons in the atom may be characterised by the atomic form factor

$$f_0 = \sum_{j=1}^{Z} \int p_j e^{-i2\pi(\vec{k}_H - \vec{k}_0) \cdot \vec{r}_j} d\tau \tag{4 10}$$

It is known that x-rays have sufficient energy to excite inner shell electrons from one level to another The effect of the electronic resonances and absorption can be included by modifying the atomic form factor to include the anomalous dispersion (Honl) corrections f' and f'' Hence, for a given atom

$$f = f_0 + f' + i f'' \tag{4 11}$$

Thus the scattering from an atom may be written as

$$\vec{E}_{at}(\vec{r}, t) = f \vec{E}_e \tag{4 12}$$

Now consider a rigid m-atom molecule, located at the origin as shown in Figure 4 1, with fixed orientation relative to a photon with wavevector $|\vec{k}_0| = 1/\lambda$
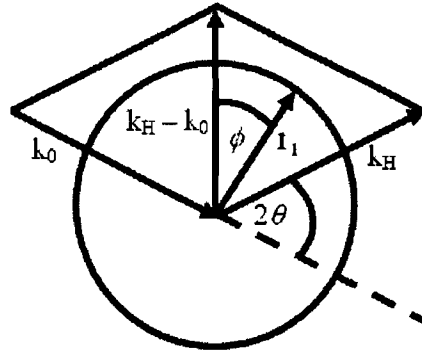
Figure 4 1 Scattering from an m-atom rigid molecule $\vec{r}_i$ is a vector from the scattering centre to atom i The molecule can take all possible orientations in space Thus the terminal point of the vector $\vec{r}_i$ has equal probability for all positions on the sphere of surface area $4\pi r_i^2$

The scattering amplitude from the molecule is

$$F = \sum_{i=1}^{m} f_i e^{-2\pi i (\vec{k}_H - \vec{k}_0) \cdot \vec{r}_i} \quad , \tag{4 13}$$

where f_i is the atomic form factor for atom i From Figure 4 1, it can be shown that

$$\left(\vec{k}_H - \vec{k}_0 \right) \cdot \vec{r}_i = 2 (r_i / \lambda) \sin \theta \cos \phi \tag{4 14}$$

Defining the momentum transfer as

$$Q = \frac{4\pi \sin \theta}{\lambda} \quad , \tag{4 15}$$

80

facilitates determination of the average molecular scattering amplitude over all possible orientations in space

$$\langle F \rangle = \sum_{i=1}^{m} f_i \left\langle e^{-2\pi i \left(\vec{k}_H - \vec{k}_0\right) \vec{r}_i} \right\rangle$$

$$= \frac{1}{4\pi r_i^2} \sum_{i=1}^{m} f_i \int_{\phi=0}^{\pi} \int_{\theta=0}^{2\pi} e^{-iQr_i \cos\phi} r_i^2 \sin\phi \, d\phi \, d\theta \qquad (4\ 16)$$

$$= \sum_{i=1}^{m} f_i \frac{\sin Qr_i}{Qr_i}$$

Therefore the intramolecular scattered intensity from one molecule with vibrational effects included is given by

$$\langle F(Q)^2 \rangle = \sum_{i=1}^{m} \sum_{l=1}^{m} f_i(Q) f_l(Q) e^{-b_{il} Q^2/2} \frac{\sin Qr_{il}}{Qr_{il}} \quad , \qquad (4\ 17)$$

where b_{il} is the variance of the bond length between atoms i and l The previous analysis employed the Debye approximation i e the scattering process could be represented as arising from independent neutral atoms possessing a spherical electron density For heavy atoms, wherein the dominant scattering comes from closed groups of inner electrons, spherical symmetry exists However, for water it should be pointed out that this assumption is not faithful to the true charge distribution As the hydrogen and oxygen atoms bond covalently, significant charge density is transferred from the hydrogen atoms to the oxygen resulting in broken symmetry In our data analysis the molecular form factor $\langle F(Q)^2 \rangle$ calculated by Narten and Levy [46] and shown in Figure 4 2 is used Sorenson et al [39] demonstrate that this form closely approximates gas-phase experimental measurements and recent self-consistent field-molecular orbital (SCF-MO) theoretical calculations to within $\sim 1\ \%$

The intermolecular contribution to the scattered intensity arises from density fluctuations in the fluid If these fluctuations were absent and a truly randomly oriented isotropic fluid existed then electromagnetic waves scattered by various molecules would possess random phase relationships No net scattering would occur due to destructive interference Consider an individual water molecule with some random orientation in the liquid By virtue of the specific random orientation of this molecule, it may not be possible for another molecule to occupy a truly random position Thus some correlation exists between the two molecules

Assume a fluid of volume V consisting of N particles may be described by a configura-
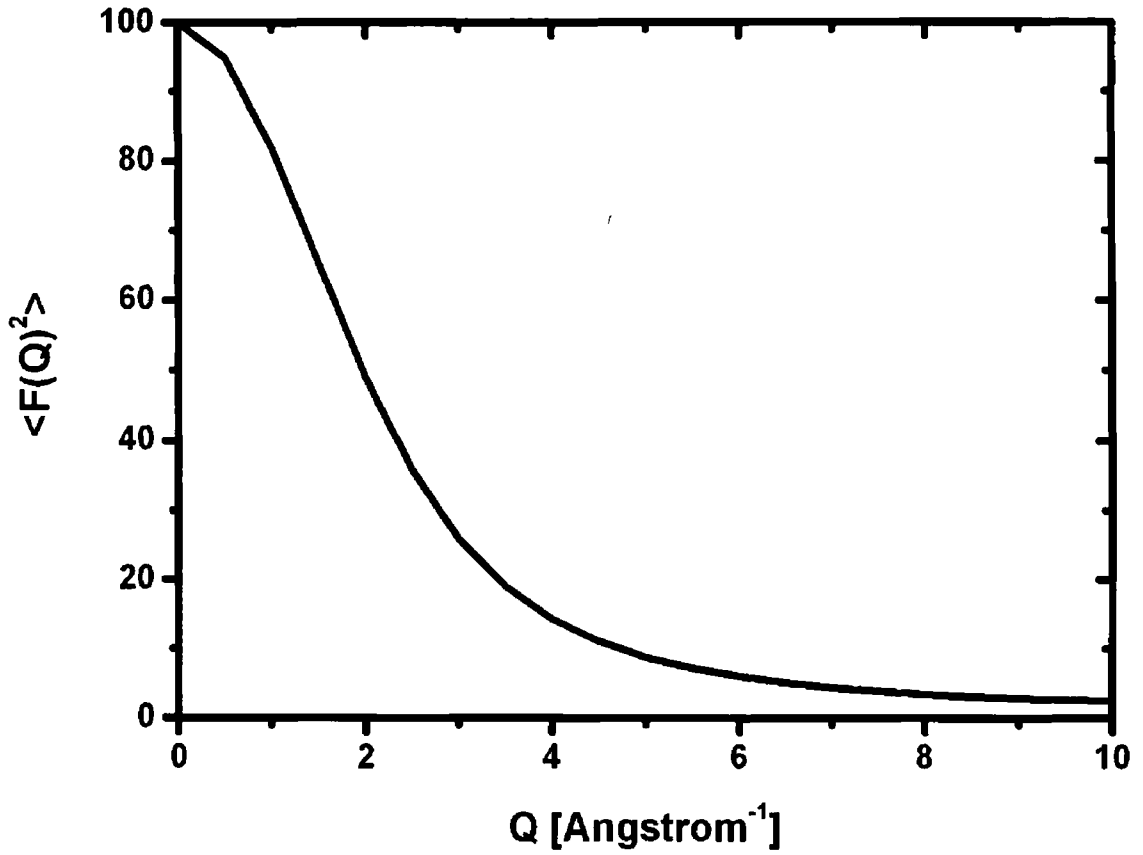
Figure 4 2 Molecular form factor $\langle F(Q)^2 \rangle$ for water calculated by Narten and Levy [46] using Equation (4 17)

tional distribution function $F_N(\vec{r}_1, \quad, \vec{r}_N)$ that satisfies the normalisation condition

$$\int_V F_N(\vec{r}_1, \quad, \vec{r}_N) d^3 r_1 \quad d^3 r_N = 1 \tag{4 18}$$

The particle density ρ_0 of a homogeneous medium at a point $\vec{r}_1$ may be obtained from a single-particle distribution function

$$\rho_0 = N \int_V F_N(\vec{r}_1, \quad, \vec{r}_N) d^3 r_2 \quad d^3 r_N = F_1(\vec{r}_1) \quad, \tag{4 19}$$

where $\int_V F_1(\vec{r}_1) d^3 r_1 = N$ The probability of finding a particle in a volume element $d^3 r$ given a particle exists at $\vec{r} = 0$ is given by the two-particle distribution function

$$F_2(\vec{r}_1, \vec{r}_2) = N(N-1) \int_V F_N(\vec{r}_1, \quad, \vec{r}_N) d^3 r_3 \quad d^3 r_N = \rho_0^2 h(\vec{r}_2 - \vec{r}_1) \tag{4 20}$$

For systems of non-interacting particles with no spatial correlations such as an ideal gas, the pair correlation function $h(\vec{r}) = 1$ However, for real liquids such as water $h(\vec{r}) \neq 1$

82

Thus the degree of correlation in the system may be expressed by the radial distribution function

$$g(\vec{r}) = h(\vec{r}) - 1 \tag{4 21}$$

Consider a macroscopic region of the fluid occupying a volume V_A. A function $\mu(\vec{r})$ is introduced such that

$$\mu(\vec{r}) = \begin{cases} 1 & \text{if } \vec{r} \text{ is inside } V_A \\ 0 & \text{if } \vec{r} \text{ is outside } V_A \end{cases} \tag{4 22}$$

The number of particles fluctuating in the volume V_A is given by

$$N_A = \sum_{i=1}^{N} \mu(\vec{r}_i) \tag{4 23}$$

It follows that

$$
\begin{aligned}
\overline{N_A} &= \sum_{i=1}^{N} \int_V \mu(\vec{r}_i) F_N\left(\vec{r}_1, \quad , \vec{r}_N\right) d^3 r_1 \quad d^3 r_N \\
&= N \int_V \mu(\vec{r}_1) d^3 r_1 F_N(\vec{r}_1, \quad , \vec{r}_N) d^3 r_2 \quad d^3 r_N \\
&= \int_V \mu(\vec{r}_1) F_1(\vec{r}_1) d^3 r_1 \\
&= \int_{V_A} F_1(\vec{r}) d^3 r \\
&= \rho_0 V_A
\end{aligned}
\tag{4 24}
$$

Realising that $\mu(\vec{r}_i)\mu(\vec{r}_i) = \mu(\vec{r}_i)$ enables us to write

$$N_A^2 = \sum_{i=1}^{N} \mu(\vec{r}_i) \sum_{j=1}^{N} \mu(\vec{r}_j) = \sum_{i \neq j} \mu(\vec{r}_i)\mu(\vec{r}_j) + \sum_i \mu(\vec{r}_i) \tag{4 25}$$

Thus

$$
\begin{aligned}
\overline{N_A^2} &= \overline{N_A} + \sum_{i \neq j} \int_V \mu(\vec{r}_i)\mu(\vec{r}_j) F_N(\vec{r}_1, \quad , \vec{r}_N) d^3 r_1 \quad d^3 r_N \\
&= \overline{N_A} + N(N-1) \int_V \mu(\vec{r}_1)\mu(\vec{r}_2) d^3 r_1 d^3 r_2 F_N(\vec{r}_1, \quad , \vec{r}_N) d^3 r_3 \quad d^3 r_N \\
&= \overline{N_A} + \int_V \mu(\vec{r}_1)\mu(\vec{r}_2) F_2(\vec{r}_1, \vec{r}_2) d^3 r_1 d^3 r_2
\end{aligned}
\tag{4 26}
$$

$$\overline{N_A^2} = \overline{N_A} + \rho_0^2 V_A \int\limits_{V_A} h(\vec{r}) d^3r \tag{4 27}$$

Using Equations (4 21), (4 24) and (4 27) the mean square fluctuation in the particle density is related to the space integral of the pair correlation function as follows

$$\frac{\overline{N_A^2} - \overline{N_A}^2}{\overline{N_A}} = 1 + \rho_0 \int\limits_{V_A} g(\vec{r}) d^3r \tag{4 28}$$

The total scattered intensity is given by the product of the number of scattering centres participating in the process and the scattering efficiency of each centre

$$\begin{aligned} I(Q) &= \left\langle F(Q)^2 \right\rangle \frac{\overline{N_A^2} - \overline{N_A}^2}{\overline{N_A}} \\ &= \left\langle F(Q)^2 \right\rangle + \rho_0 \left\langle F(Q)^2 \right\rangle \int\limits_{V_A} g(\vec{r}) d^3r \end{aligned} \tag{4 29}$$

Thus it can be seen that the scattered intensity depends on the intramolecular scattering as well as intermolecular correlations, the first and second terms in Equation (4 29), respectively Employing Equation (4 17) whilst neglecting vibrational effects for the moment yields

$$I(Q) = \sum_{il} f_i(Q) f_l(Q) \frac{\sin Q r_{il}}{Q r_{il}} + \rho_0 \sum_{il} f_i(Q) f_l(Q) \int\limits_{V_A} g(\vec{r}) \frac{\sin Q r_{il}}{Q r_{il}} d^3r \tag{4 30}$$

Integrating over the volume V_A in spherical co-ordinates yields

$$\begin{aligned} I(Q) &= \left\langle F(Q)^2 \right\rangle + \rho_0 \sum_{il} f_i(Q) f_l(Q) \int\limits_{r=0}^{\infty} \int\limits_{\theta=0}^{\pi} \int\limits_{\phi=0}^{2\pi} g(\vec{r}) \frac{\sin Qr}{Qr} r^2 \sin\theta dr d\phi d\theta \\ &= \left\langle F(Q)^2 \right\rangle + 4\pi\rho_0 \sum_{il} f_i(Q) f_l(Q) \int\limits_{r=0}^{\infty} g(\vec{r}) \frac{\sin Qr}{Qr} r^2 dr \end{aligned} \tag{4 31}$$

The final expression is

$$I(Q) = \left\langle F(Q)^2 \right\rangle + \left\langle F(Q) \right\rangle^2 \int\limits_{r=0}^{\infty} 4\pi\rho_0 r^2 g(\vec{r}) \frac{\sin Qr}{Qr} dr \tag{4 32}$$

The quantity $\left\langle F(Q) \right\rangle^2$ describes the average scattering from a molecule of random orientation with respect to any other molecule taken as the origin In general the simplification

84

$\langle F(Q)^2 \rangle = \langle F(Q) \rangle^2$ is made [46] enabling one to typically define the structure factor as

$$S(Q) = \frac{I(Q) - \langle F(Q)^2 \rangle}{\langle F(Q)^2 \rangle} \quad , \tag{4 33}$$

from which the radial distribution function can be directly obtained

$$g(r) = 1 + \frac{1}{2\pi^2 \rho_0 r} \int_0^\infty Q S(Q) \sin Q r \, dQ \tag{4 34}$$

In our measurement a difference signal $\delta I(Q, t) = \langle F(Q)^2 \rangle \, \delta S(Q, t)$ is recorded Therefore we may relate our difference signal to a change in the intermolecular radial distribution function by

$$\delta g(r) = \frac{1}{2\pi^2 \rho_0 r} \int_0^\infty \frac{\delta I(Q)}{\langle F(Q)^2 \rangle} Q \sin Q r \, dQ \tag{4 35}$$

4.3   Experimental Method

Experiments were carried out at the Advanced Light Source (ALS) synchrotron at the bend magnet beamline 5 3 1 A W/B$_4$C or W/Si multilayer mirror provided quasi monochromatic light with bandwidth $\Delta E/E \sim 2\,5\,\%$ This provided sufficient spectral resolution to observe changes in the broad diffraction peaks associated with the liquid state Experiments were carried out at photon energies of both 7 8 keV and 9 9 keV and in a variety of different excitation geometries Both two-photon excitation of pure water and single-photon excitation in water doped with the dye pyranine (8-hydroxy-1,3,6-pyrenetrisulfonate, obtained from Sigma-Aldrich) was employed A titanium-sapphire based femtosecond laser system, producing 150 fs pulses at 800 nm, 1 kHz repetition rate, and synchronized to individual x-ray pulses to ~ 2 ps accuracy, was used to generate excitation pulses at 266 nm for two-photon excitation of pure water or at 400 nm for single-photon excitation of pyranine in water Excitation intensities were 0 5 to 1 TW/cm^2, below the threshold for continuum generation The sample was a liquid jet producing a thin sheet of water 30 to 300 μm thickness, homemade following [152] or obtained from Kyburz Diffracted x-ray pulses were measured using a large area avalanche photodiode with a horizontal slit and scanned vertically (perpendicular to the incident x-ray polarization vector) to record the diffracted intensity over a range in $Q = 4\pi \sin \theta / \lambda$, where θ, λ are the diffracted angle and wavelength of the incident x-ray photons, respectively Calibration of the x-ray wavelength and detector distance was performed by measuring multiple diffraction orders from a diamond powder at two different sample-to-detector distances Calculations and measurements show that the loss of resolution due

to the finite height and width of the diode slit has only a small effect on measurement of the scattered intensity up to $Q = 4$ Å^{-1} A fast avalanche photodiode was used to electronically gate out a single x-ray pulse from the train of pulses typically produced by the synchrotron, and thus perform pump-probe measurements with time resolution set by the duration of the x-ray probe pulses ($\sim$ 70 ps) A schematic of the experimental setup can be seen in Figure 4 3 on page 87 Further details on the synchrotron-laser synchronisation mechanism and the time structure of the ALS can be found in Appendix A

A differencing data collection technique was applied in which the diffracted intensity $I(Q)$ was recorded at 2 kHz repetition rate, twice the repetition rate of the optical excitation source, on a shot by shot basis [143] This enables measurement of the transient change in diffracted intensity $\delta I(Q, t) = I(Q, t) - I(Q, 0)$ at 1 kHz and cancels out the effect of long time-scale drifts as well as background scattering effects which are time independent With an incident x-ray flux of order 10^6 photons/pulse and integration times of order 30 s per point, we are able to resolve changes in the liquid structure factor of order a fraction of a percent

4.4 Results and Discussion

Figure 4 4 on page 89 shows the measured (black line) static diffracted intensity as a function of Q for neat water, obtained by scanning over a range 1 5 to 4 9 Å^{-1} Each point corresponds to an average of about 3×10^4 shots or 30 s of integration The curve is normalized by comparing to previous static measurements of the structure factor of water and is in reasonable agreement with same (red line) [45, 46] Differences in the two data sets can be attributed to the loss in resolution due to the multilayer Also Hura *et al* [45] performed very detailed corrections to the data including precise removal of background scatter, applying geometric corrections to their detector configuration, as well as polarisation and absorption corrections Such detailed data manipulation was not necessary in this study as the difference signal naturally removes these experimental artifacts

Figure 4 5 on page 90 (black line) displays the transient change in the structure factor δS at $t = 700$ ps following excitation at 266 nm δS represents the change in the scattered intensity normalized by the Q-dependent scattering from a single H_2O molecule [46], denoted by $\langle F(Q)^2 \rangle$, i e , $\delta S = \delta I / \langle F(Q)^2 \rangle$ One observes an oscillatory difference signal, corresponding to a decrease near the peak of the structure factor at $Q = 2$ Å^{-1} and an increase near the shoulder region around 2 5 Å^{-1} This is interpreted as follows impulsive heating through femtosecond excitation leads to the generation of both temperature and pressure jumps These result in changes in the structure factor $S(Q)$, which may be
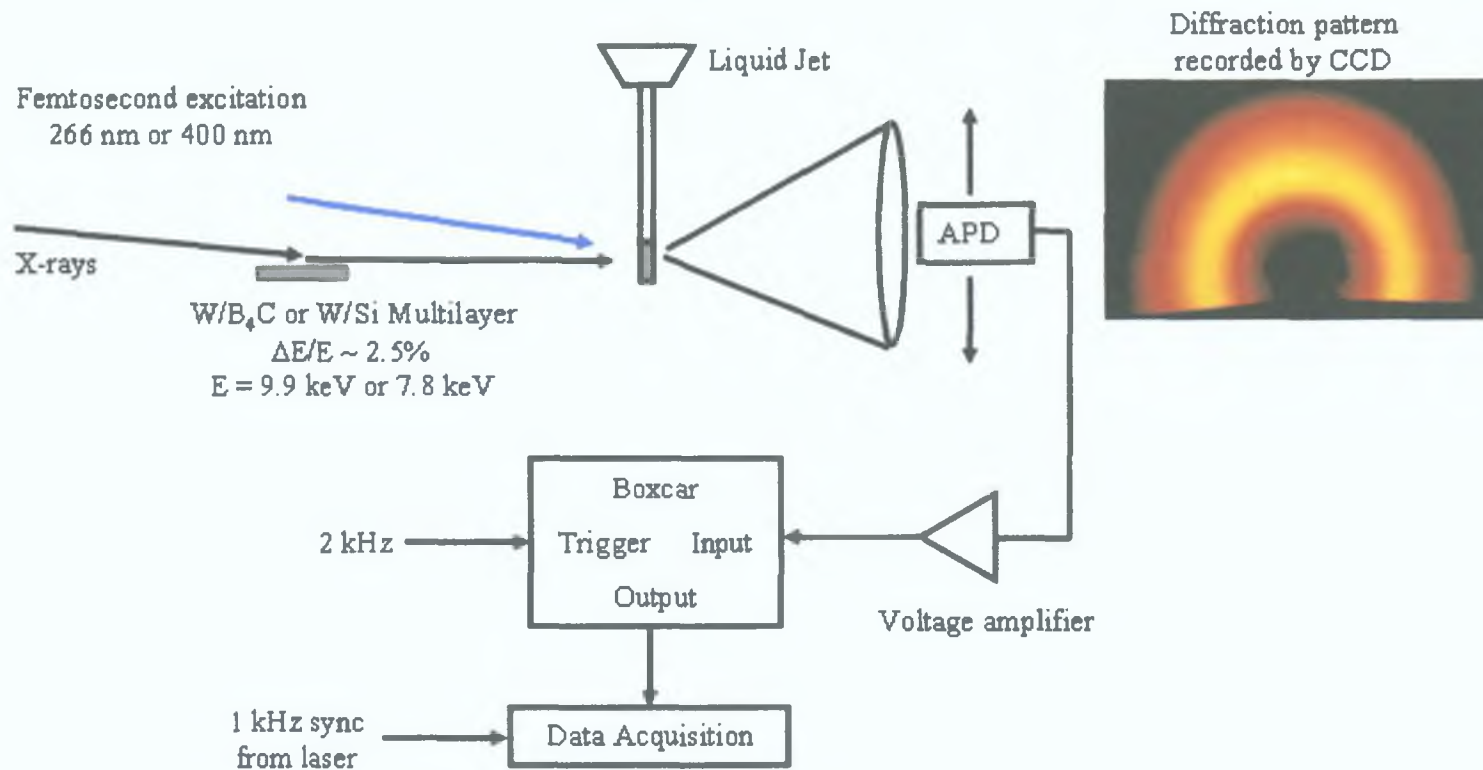
Figure 4.3: Experimental setup for laser-pump x-ray probe measurements.

written as [153]

$$\delta S = \left(\frac{\partial S}{\partial T}\right)_P \delta T + \left(\frac{\partial S}{\partial P}\right)_T \delta P \qquad (4\ 36)$$

On short time scales, before the system has time to expand, heating occurs isochorically, giving rise to a pressure jump $\delta P = \alpha/\chi\delta T$ where α is the thermal expansion coefficient and χ is the isothermal compressibility In this short-time-scale limit, the Equation (4 36) reduces to [153, 154]

$$\delta S = \left(\frac{\partial S}{\partial T}\right)_V \delta T = \frac{\chi}{\alpha}\left(\frac{\partial S}{\partial T}\right)_V \delta P \qquad (4\ 37)$$

Thus one directly measures the isochoric temperature differential, i e , the temperature-dependent change in the structure factor at constant volume, with amplitude set by the transient optically induced temperature or pressure increase (estimated to be of order 10 K and 40 Bar, respectively, using standard values for the thermal expansion coefficient, heat capacity and isothermal compressibility [87]) We estimate that the time for significant expansion to occur is of order the length scale for energy deposition divided by the speed of sound For the case of uniform excitation of the jet, this length scale is set by the laser spot size (300 μm) [85], corresponding to a time scale of roughly 300 ns This serves as an upper bound on the time scales on which the above approximations remain valid This time scale has been verified by Plech et al [85] in time-resolved work on liquid CCl_4

For the case of water, one may cancel the effects of volumetric changes to first order without employing time-resolved techniques Because liquid H_2O exhibits a density maximum at 4 °C at atmospheric pressure, one may choose pairs of temperatures for which the density is the same, and thus isolate the temperature-dependent effects on the hydrogen bond network [57,58,84] In the following, we compare our time-resolved measurements to the static measurements of Bosio et al [84] to support the interpretation that the observed transient changes in the water structure correspond to isochoric heating effects Figure 4 5 on page 90 shows the Q-dependent difference signal obtained for an 8° temperature differential about the temperature of maximum density, in comparison with our time-resolved measurement at $t = 700$ ps The time-dependent data has been scaled up by a factor of five for comparison The agreement between the two curves illustrates that the time-resolved techniques described here accurately record the isochoric temperature differential

Nonlinear absorption under multiphoton excitation conditions often leads to highly nonuniform excitation of the liquid jet [87, 155] and high concentrations (up to 10 mM) of solvated electrons and other photoproducts which may themselves perturb the local structure of water [156] Thus the transient structural changes which occur in water doped with the dye pyranine under single-photon excitation conditions at 400 nm were also measured for
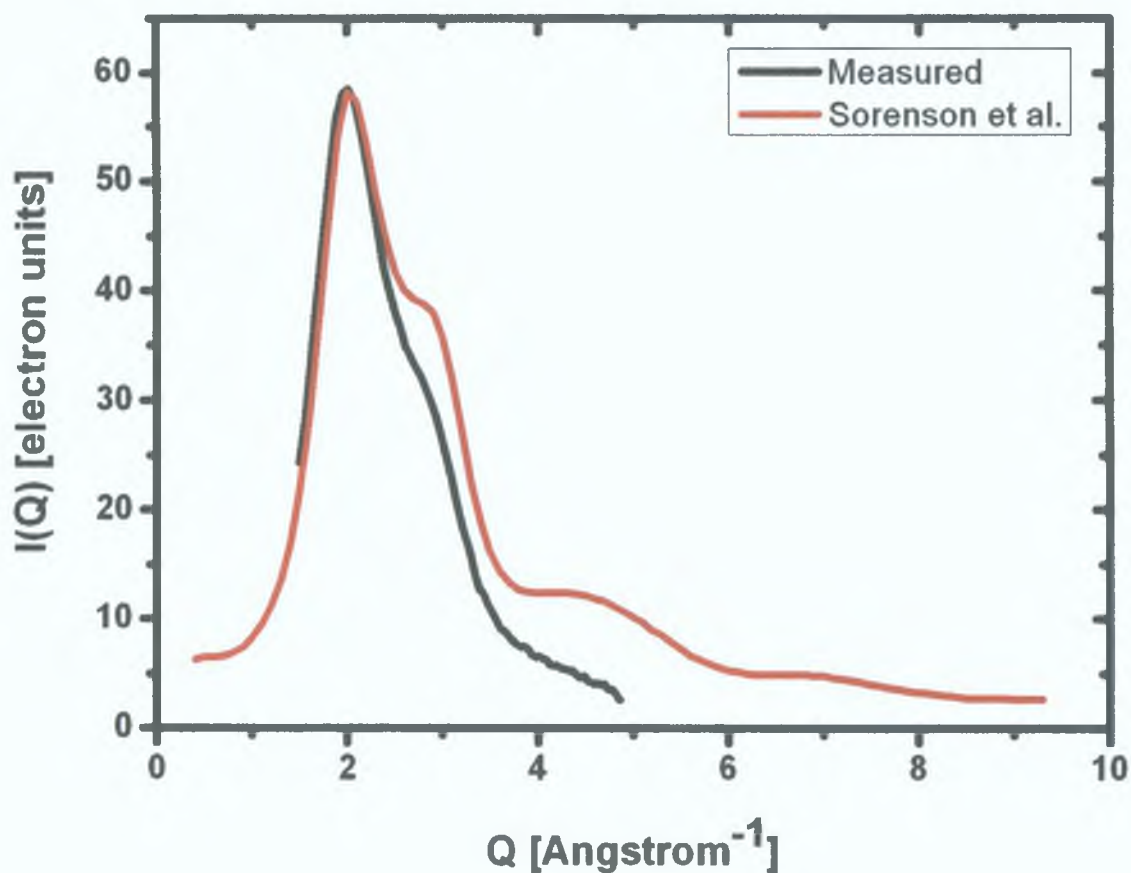
Figure 4.4: Static x-ray intensity as a function of Q through a 100 μm water jet obtained by scanning an avalanche photodiode across the diffraction ring. Shown for comparison is the data of Hura *et al.* [45].

comparison. Pyranine is well known to behave as a photon-initiated acid [68, 157–159] undergoing an excited-state proton transfer reaction upon optical excitation with an effective pH jump and ensuing hydrogen-bond rearrangements localized around the proton transfer event. Figure 4.6 on page 91 displays a comparison of the time-resolved effects observed for the case of neat water excitation versus pyranine-doped water at 5 mM concentration. We observe qualitative agreements for both excitation conditions, indicating that the changes in the structure factor are not directly related to charge transfer reactions. Because x-ray scattering probes the entire excited volume, structural effects due to solvation-induced rearrangements of the local oxygen environment are expected and confirmed to be small under these conditions. Recent measurements [87] have emphasized the importance of temperature-jump effects under similar excitation conditions with respect to studies of optically induced solvated electrons in water. For our experimental conditions, although the initial deposition of energy is highly nonuniform (for excitation in neat water at the highest intensities, corresponding to an average electron spacing of about 50 Å), the time for thermal diffusion to create roughly uniform conditions is only
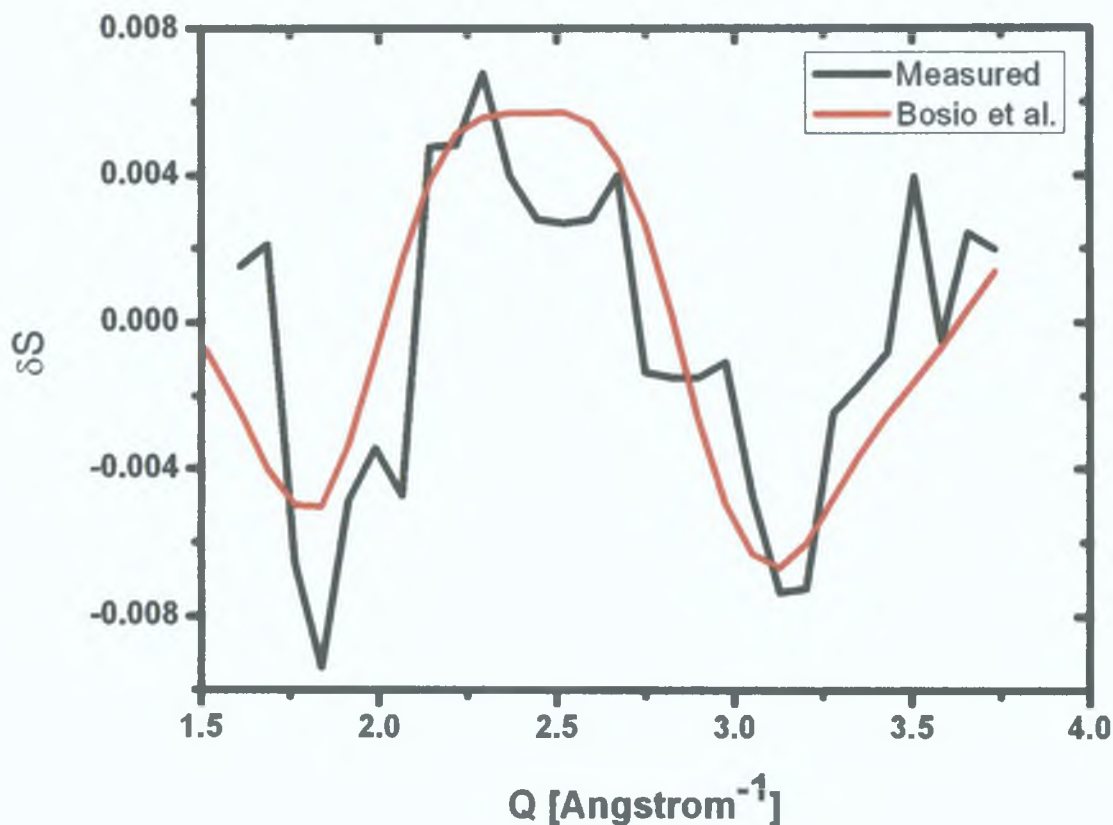
Figure 4.5: Comparison of transient data at $t = 700$ ps for neat water excited by 266 nm photons with the static isochoric measurements of Bosio *et al.* [84]. Black curve, transient data. Red curve, static data.

30 ps [87]. Thus, the x-ray probe pulse scatters from a roughly uniformly heated sample for the time scales probed here.

Instead of obtaining snapshots of $S(Q)$ at various time delays, one may instead fix the detector position and scan the relative time between pump and probe to directly obtain the time-dependent $\delta S(Q, t)$ for a given Q. Figure 4.7 on page 92 shows the time-resolved change at $Q = 2.5$ Å^{-1} on the shoulder of the diffracted intensity curve, over a 1.5 ns time scale. An increase in scattering occurring on a time scale limited by the time resolution of the experiment ($\sim$ 70 ps) is observed. This is in agreement with the direction and magnitude observed in the Q-dependent scans displayed in Figure 4.5.

The measured difference signal $\delta I(Q, t)$ may be directly related to a corresponding change in the intermolecular oxygen-oxygen radial distribution function $\delta g_{OO}(r)$ using Equation (4.35). As the static structure factor continues to oscillate at momentum transfers extending above 10 Å^{-1}, truncation effects often limit the accuracy of extracted pair correlation functions. In contrast, since most of the structural changes in water are associated with intermolecular rearrangements, the high Q (short-length-scale) part of the structure factor
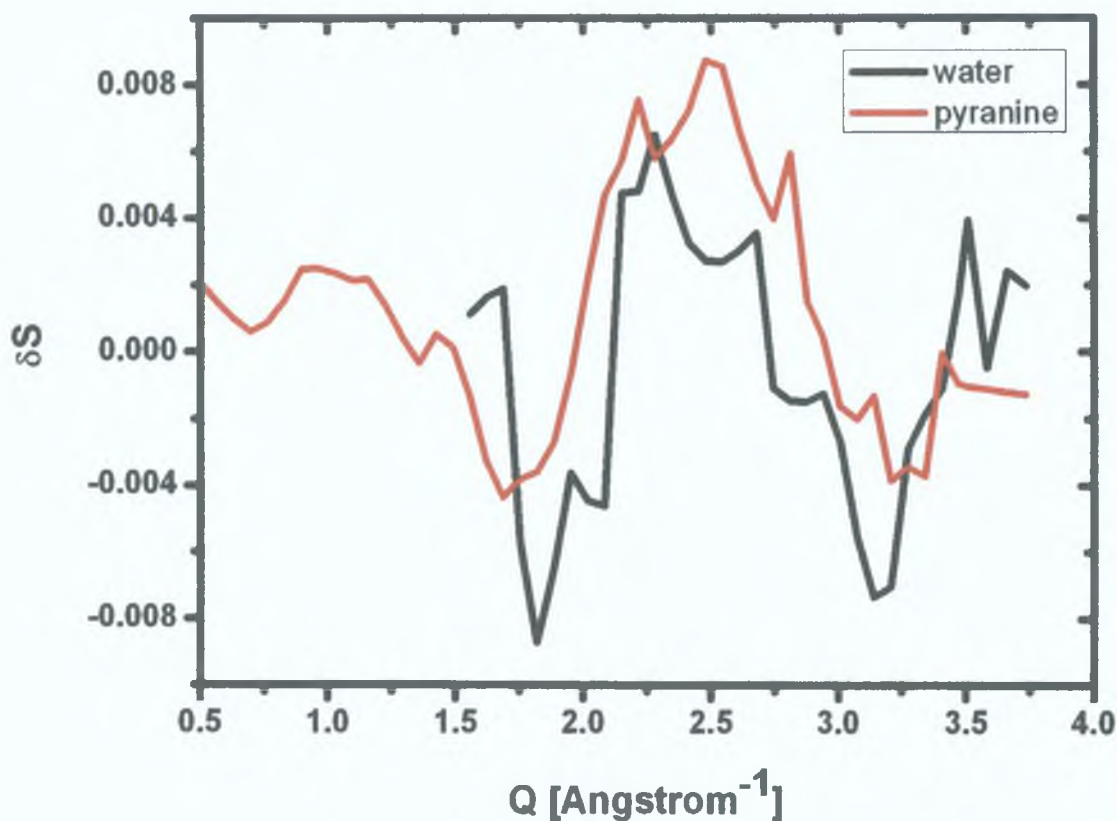
Figure 4.6: Comparison of transient effects observed for the case of two-photon excitation of neat water (black curve) and one-photon excitation of pyranine-doped water at 5 mM concentration (red curve) at $t = 700$ ps.

remains relatively constant. Thus the differential structure factor $\delta S(Q)$ (which is directly measured by the time-resolved technique) goes rapidly to zero above 5 Å^{-1}, more rapidly than the structure factor itself. This allows for the extraction of changes in the radial distribution function with data over only a limited range in Q [84]. Figure 4.8 (a) on page 93 shows the extracted time-dependent change in the pair correlation function from Equation (4.35) at $t = 700$ ps following excitation of neat water, again shown in comparison to the static isochoric measurements. No artificial damping at high Q of the structure factor data is applied. One observes that the positions of the first four minima and maxima for the transient data are in good agreement with the temperature dependent static measurements. The first minimum at about 2.7 Å is located near the peak of the static pair correlation function and corresponds to the well-known nearest neighbor oxygen-oxygen spacing as shown in Figure 4.8 (b). The second minimum at 4.5 Å corresponds to the next-nearest-neighbor spacing (at $\sqrt{8/3}$ times the nearest-neighbor spacing for perfect tetrahedral ordering), indicating a large change in the second nearest-neighbor shell. A corresponding increase occurs at 3.5 Å, in between the first and second nearest-neighbor peaks. The extracted changes extend significantly outside the nearest-neighbor shell and
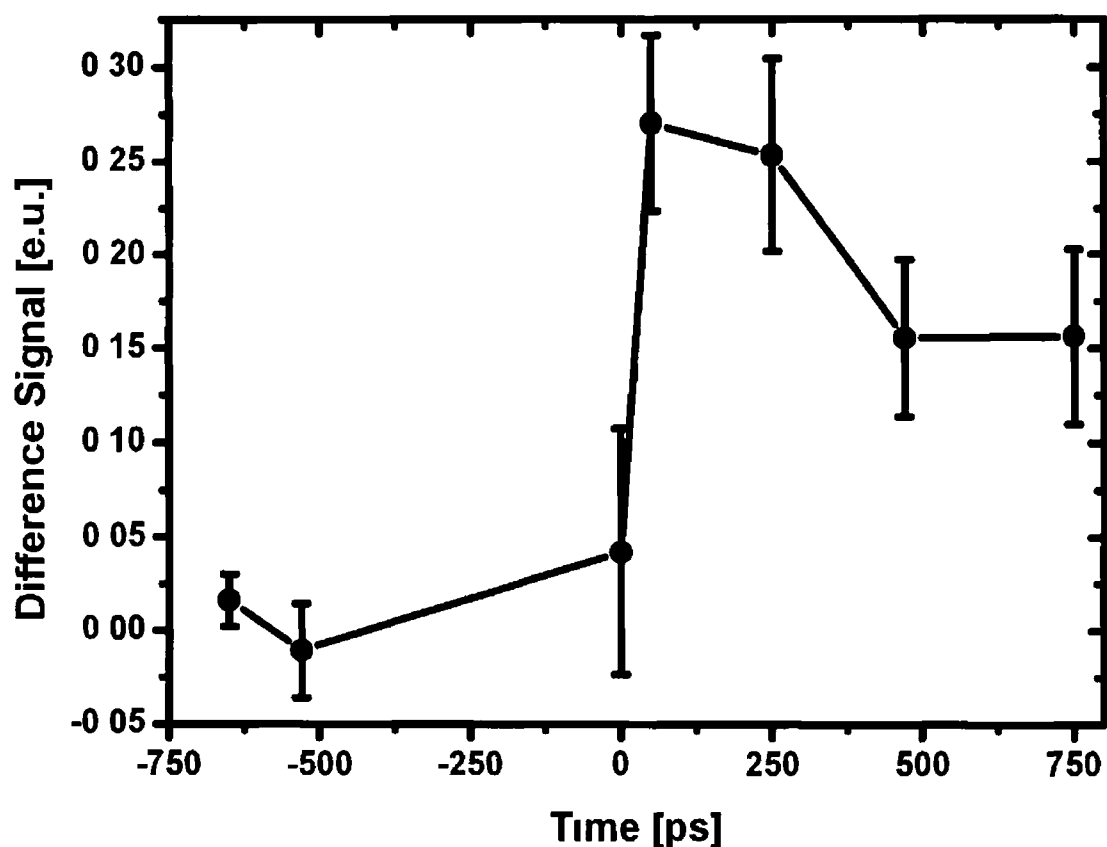
Figure 4 7 Time-resolved measurement of changes in $S(Q, t)$ at $Q = 2\,5\,\text{Å}^{-1}$ obtained by scanning the relative timing between laser pump and x-ray probe The observed structural changes occur on a time scale limited by our temporal resolution (~ 70 ps)

the fractional change in the pair correlation function is significantly larger at the second nearest-neighbor position as compared to the first The recorded differential pair correlation function at $t = 700$ ps after excitation thus captures the changes in the local structure of water associated with a breakdown of tetrahedral ordering, the same changes which give rise to an increase in density on heating water below 4 °C

4.5 Conclusions

A technique for probing the isochoric differential structure factor in water has been described which makes use of time-resolved x-ray techniques to probe changes in the structure of water before significant expansion occurs For time scales less than the expansion time but longer than typical hydrogen bond lifetimes, the observed changes are well described by constant volume temperature jump effects This technique may be extended to probe temperature-jump effects in other liquids under arbitrary initial conditions

Time-resolved differential changes in the pair correlation function have been extracted
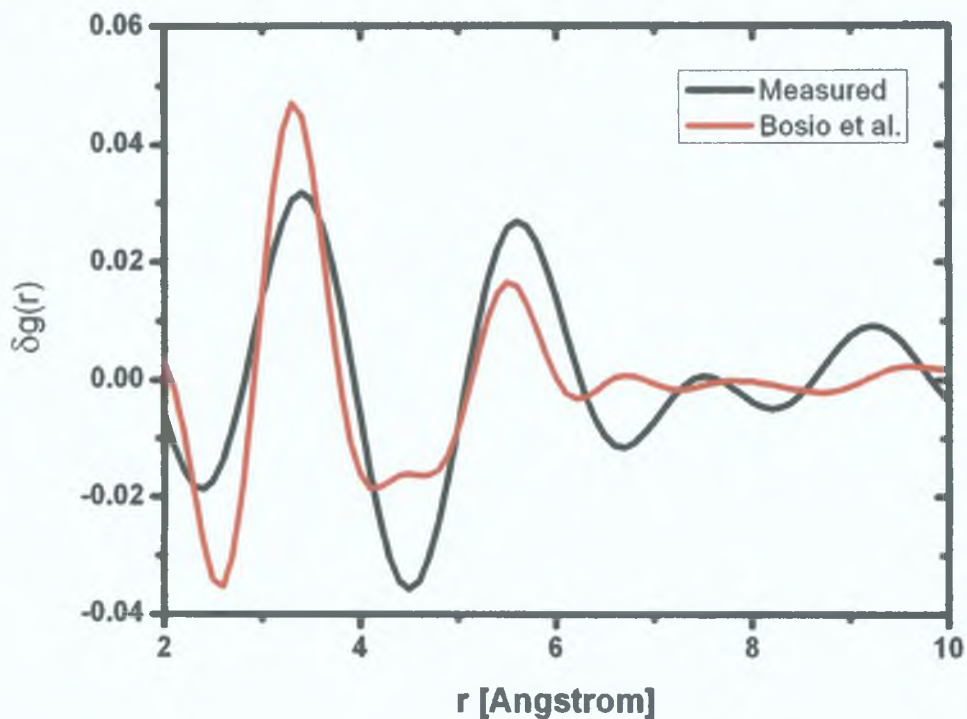
(a) Transient changes in the radial distribution function (black curve) compared with the isochoric data of Bosio *et al.* [84] (red curve).
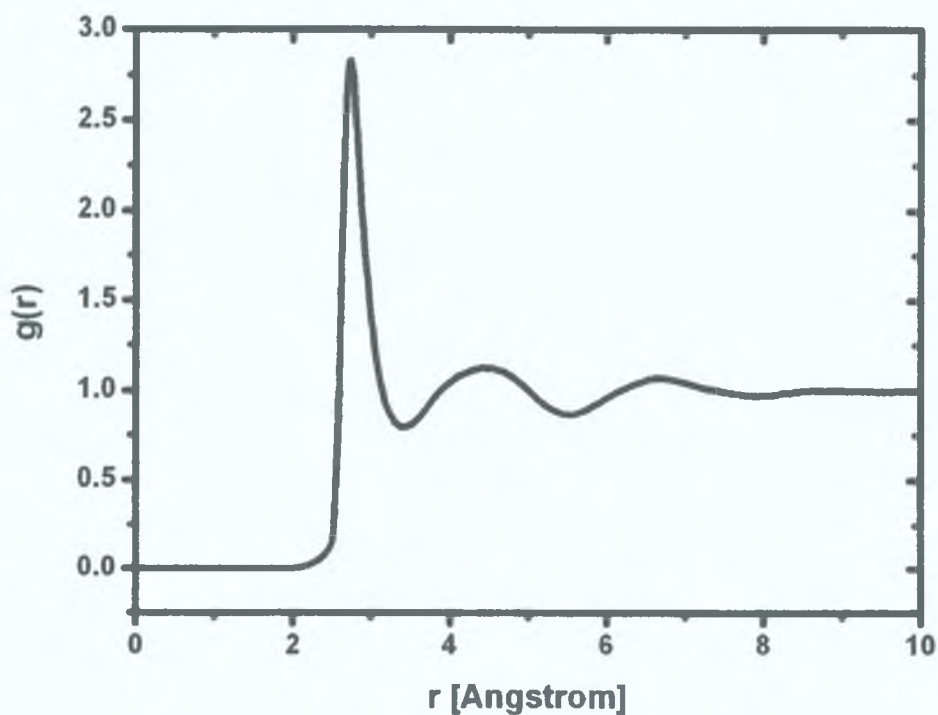
(b) Static radial distribution function of water.

Figure 4.8: (a) Comparison of change in the pair correlation function $\delta g(r)$ at $t = 700$ ps with the isochoric temperature differential data of Bosio *et al.* [84]. (b) Static radial distribution function of water measured by Hura and Sorenson [39,45].

under experimental conditions where data at large Q is limited due to weak scattering and photon number constraints We have shown that if one is interested in obtaining only transient changes in the pair correlation function, the requirements for reliable inversion of structure factor data are considerably reduced Next generation ultrafast x-ray sources [7] should be able to apply this principle to a variety of problems in the liquid state In particular, the application of these new sources to the problem of liquid water should enable direct measurement of intrinsic structural rearrangements and the breaking of hydrogen bonds in water on the time-scales upon which they occur

Acknowledgments

Chapter 5

Conclusions

In the first part of this thesis, the design, construction and test of a grazing incidence x-ray streak camera was described. The experimental apparatus of Chapter 2 has been used to characterise the quantum efficiency of reflection photocathodes. The reflection geometry has been shown to increase the detection efficiency of a grazing incidence camera several fold over its normal incidence counterpart. Whilst a temporal resolution of 6 ps was demonstrated, further development of the sweep plate geometry is necessary to push this to the sub-picosecond level. In its present guise, the camera compliments the slicing program at the Advanced Light Source. However any improvement to its temporal resolution can only enhance its applicability by further reducing signal integration times.

To date x-ray streak camera development has pursued a "brute force" strategy to achieve progressively higher temporal resolution. Photocathodes with narrow secondary electron energy distributions and significant extraction fields have been used to reduce space charge and secondary electron chromaticity induced temporal dispersion. Until recently, progress could be attributed less to innovation and more to technological refinement. Recently a novel scheme was proposed by Jaanimagi [160] to make an isochronous x-ray streak camera with the potential to break the 100 fs barrier. The positive energy dispersion of the secondary electron distribution is compensated by introducing a corresponding negative energy dispersion into the camera with a double hemi-spherical electrostatic chicane structure. In theory, the proposed idealised structure works. However, in practice simulations have demonstrated that fringe field effects at the interface of the hemi-spherical analysers makes the system unworkable. The idea, however, has motivated the design of chromaticity compensation structures that appear feasible [161].

So what is the ultimate temporal resolution of an x-ray streak camera? Is it 10 fs as suggested by Zavoisky and Fanchenko [26]? The aforementioned proposal with judicious design of the sweep plate structure would seem to imply that sub-100 fs is certainly possible. Photoconductive switch jitter can be avoided using fast readout CCDs and space charge dispersion using accelerator technology [161]. At these timescales the dynamics of the photoemission process within the cathode will become extremely important and it is proffered here that this is the physical bottleneck.

Consider two photons incident on a 1000 Å thick CsI photocathode A normal incidence transmission cathode geometry is assumed for the sake of simplicity One photon is absorbed at the front surface, the other at the back surface The transit time for the second photon to traverse the cathode thickness is approximately 0 3 fs, negligible on the timescales involved here Keeping the model simple, assume each photon decays instantly and generates a secondary electron with energy 1 eV The corresponding velocity of the electrons is approximately 6×10^5 m/s Thus if the front surface electron were to propagate straight through the cathode it would emerge $\sim$ 170 fs after the backside electron

In reality the previous result may be viewed as a lower bound that scales with cathode thickness A one dimensional field free Monte Carlo simulation developed by Boutboul *et al* [95] was employed to gain further insight into the problem Preliminary results tracking the electron cascade in a CsI photocathode indicate that the transit time is significantly increased due to the random walk the secondary electron undergoes due to interactions with optic and acoustic phonons A value of 3 ps was obtained It will be appreciated that the temporal resolution of x-ray streak cameras is significantly better than this At present we believe the extraction field significantly modifies the random walk such that the electron scattering becomes preferentially directed toward the cathode exit surface Hence the real value is somewhat lower than this This simple analysis has led to bounds on the ultimate temporal resolution of a normal incidence x-ray streak camera employing a CsI cathode 170 fs $\leq \tau_{instrument} \leq$ 3 ps Interestingly if a reflection cathode is used at grazing angle the lower bound scales to $\sim$ 40 fs with the Monte Carlo simulation demonstrating an upper bound of approximately 1 ps Thus reflection cathodes will not only be necessary in the future for quantum efficiency reasons but also to achieve the ultimate temporal resolution!

Further work needs to be undertaken The Monte Carlo simulation will be extended to three dimensions and more importantly, the electric field will be included Obviously the validity of the model will have to be tested and the following experiment is suggested Replace the photocathode in a conventional ultrafast optical streak camera with a CsI cathode coated with a thin layer of carbon Carbon, a conductor, will shield electrons inside the cathode from the extraction field whilst still enabling them to refract into vacuum In the limit that the field free simulation is correct one should record an electron pulse with significantly longer temporal duration compared to an uncoated cathode

In the future it is proposed that x-ray streak cameras will be used to monitor excited state dynamics in plasma's pumped by the x-ray beam from an XFEL In these high flux situations typical alkali halide materials will catastrophically degrade in a few shots due to color center formation [162, 163] These effects are already seen at some synchrotron sources [161] Thus alternative cathodes will have to be found One possibility showing

promise is diamond due to its radiation hardness By suitable surface treatment diamond can be made into a negative electron affinity photocathode with a very narrow secondary electron energy distribution (less than 1 eV) [164] Thus, the low x-ray photon absorption and its quantum efficiency implications may be compensated for and an ultrafast radiation robust cathode developed Preliminary measurements made using the total electron yield apparatus of Chapter 2 would seem to confirm this but further investigation is necessary Other nanotechnology based cathode structures have been conceived For example, silicon nano grass may have x-ray absorption properties similar to bulk silicon with significantly different electron emission characteristics owing to its pseudo two-dimensional structure Alas investigation of these structures must wait

A method to probe the isochoric differential structure factor of a liquid has been described in the latter half of this thesis Whilst it was not possible to achieve the initial experimental aim, namely resolution of the perturbative effect of solvated charged species on the aqueous structure, structural rearrangement at the second-neighbor shell was identified The transient changes in the radial distribution function were interpreted as a decrease in the local tetrahedral ordering

The experiment was specifically designed to be compatible with future ultrafast x-ray sources The Sub-Picosecond Photon Source (SPPS) in operation at the Stanford Linear Accelerator Center (SLAC) is a precursor and testbed for the XFELs that are due to come online in the next decade SPPS is a linac-based x-ray source that uses electron acceleration and bunch compression schemes nearly identical to those proposed for the Linac Coherent Light Source (LCLS) SPPS is the first source to employ compressed femtosecond electron bunches to produce sub-100 fs x-ray pulses and is currently the worlds brightest ultrafast x-ray source [7, 165, 166] A preliminary x-ray diffraction measurement of a liquid jet used in the experiments of Chapter 4 was undertaken at SPPS to ascertain the viability of a time-resolved pump-probe experiment An image intensified CCD placed in close proximity to the jet constituted the detector Whilst the whole diffraction ring was collected simultaneously, the setup negated the possibility of using a differencing technique Thus a time-resolved measurement would be prone to errors introduced by system drift Given the fractional percent scale difference signal from Chapter 4 and the integration times involved to collect a signal on the CCD, it was deemed unfeasible to resolve the difference signal from long term drifts associated with the source

However, with the brightness of future XFELs the experiment should become tenable and numerous enhancements to the experiment can be envisaged Hence one could imagine probing the evolution of the excited state water molecule through the formation of an intermediate "wet" electron and finally to the creation of the solvated electron The increased time resolution would allow snap shots to be recorded before non-radiative thermal effects dominate the signal Similarly one could probe the ejection of the proton from the

97

photoacid into the liquid

By extending this technique to the supercooled regime [167], it should be possible to record isochoric structure factor changes between two temperatures both of which are in the supercooled regime, where the anomalous properties of water are most evident By pumping at infrared photon energies, one would directly probe the induced intermolecular rearrangements One could even imagine performing experiments where an ice-water phase transition is driven by resonantly pumping the vibrational frequencies of the atoms Whilst the focus here has been on water, it should be stressed that the technique is applicable to any neat liquid or a liquid embedded with a chromophore

Bibliography

[1] B Adams, ed , *Nonlinear Optics, Quantum Optics, and Ultrafast Phenomena with X-rays*, p 160 Kluwer Academic Publishers, 2003

[2] W Rontgen, "On a new kind of rays," *Nature*, vol 53, p 274, 1896

[3] G Gould, "Optically pumped laser amplifiers," *US Patent No 4,053,845*, October 1977

[4] G Gould, "Light amplifiers employing collisions to produce a population inversion," *US Patent No 4,704,583*, November 1987

[5] J Watson and F Crick, "Molecular structure of nucleic acids," *Nature*, vol 171, pp 737–738, 1953

[6] T Udem, R Holzwarth, and T Hansch, "Optical frequency metrology," *Nature*, vol 416, no 6877, pp 233–237, 2002

[7] A Lindenberg, J Larsson, K Sokolowski-Tinten, K Gaffney, C Blome, O Synnergren, J Sheppard, C Caleman, A MacPhee, D Weinstein, D Lowney, T Allison, T Matthews, R Falcone, A Cavalieri, D Fritz, S Lee, P Bucksbaum, D Reis, J Rudati, P Fuoss, C Kao, D Siddons, R Pahl, J Als-Nielsen, S Duesterer, R Ischebeck, H Schlarb, H Schulte-Schrepping, T Tschentscher, J Schneider, D von der Linde, O Hignette, F Sette, H Chapman, R Lee, T Hansen, S Techert, J Wark, M Bergh, G Huldt, D van der Spoel, N Timneanu, J Hajdu, R Akre, E Bong, P Krejcik, J Arthur, S Brennan, K Luening, and J Hastings, "Atomic-scale visualization of inertial dynamics," *Science*, vol 308, pp 392–395, 2005

[8] K Gaffney, A Lindenberg, J Larsson, K Sokolowski-Tinten, C Blome, O Synnergren, J Sheppard, C Caleman, A MacPhee, D Weinstein, D Lowney, T Allison, T Matthews, R Falcone, A Cavalieri, D Fritz, S Lee, P Bucksbaum, D Reis, J Rudati, P Fuoss, C Kao, D Siddons, R Pahl, J Als-Nielsen, S Duesterer, R Ischebeck, H Schlarb, H Schulte-Schrepping, T Tschentscher, J Schneider, D von der Linde, O Hignette, F Sette, H Chapman, R Lee, T Hansen, S Techert, J Wark, M Bergh, G Huldt, D van der Spoel, N Timneanu, J Hajdu, R Akre, E Bong, P Krejcik, J Arthur, S Brennan, K Luening, and J Hastings, "Observation of structural anisotropy and the onset of liquidlike motion during the nonthermal melting of InSb," *Physical Review Letters*, vol 95, p 125701, 2005

[9] K Sokolowski-Tinten, C Blome, J Blums, A Cavalieri, C Dietrich, A Tarasevitch, I Uschmann, E Forster, M Kammler, M Horn-von Hoegen, and D von der

Linde, "Femtosecond x-ray measurement of coherent lattice vibrations near the Lindemann stability limit," *Nature*, vol 422, no 6929, pp 287–289, 2003

[10] A Cavalleri, M Rini, H Chong, S Fourmaux, T Glover, P Heimann, J Kieffer, and R Schoenlein, "Band-selective measurements of electron dynamics in VO_2 using femtosecond near-edge x-ray absorption," *Physical Review Letters*, vol 95, p 067405, 2005

[11] F Schotee, M Lim, T Jackson, A Smirnov, J Soman, J Olson, G Phillips, M Wulff, and P Anfinrud, "Watching a protein as it functions with 150-ps time-resolved x-ray crystallography," *Science*, vol 300, pp 1944–1947, 2003

[12] S Johnson, P Heimann, A MacPhee, A Lindenberg, O Monteiro, Z Chang, R Lee, and R Falcone, "Bonding in liquid carbon studied by time-resolved x-ray absorption spectroscopy," *Physical Review Letters*, vol 94, p 057407, 2005

[13] S Choe, Y Acremann, A Scholl, A Bauer, A Doran, J Stohr, and H Padmore, "Vortex core-driven magnetization dynamics," *Science*, vol 304, no 5669, pp 420–422, 2004

[14] R Neutze, R Wouts, D van der Spoel, E Weckert, and J Hajdu, "Potential for biomolecular imaging with femtosecond x-ray pulses," *Nature*, vol 406, pp 752–757, 2000

[15] M Hentschel, R Kienberger, C Spielmann, G Reider, N Milosevic, T Brabec, P Corkum, U Heinzmann, M Drescher, and F Krausz, "Attosecond metrology," *Nature*, vol 414, pp 509–513, 2001

[16] E Goulielmakis, M Uiberacker, R Kienberger, A Baltuska, V Yakovlev, A Scrinzi, T Westerwalbesloh, U Kleineberg, U Heinzmann, M Drescher, and F Krausz, "Direct measurement of light waves," *Science*, vol 305, pp 1267–1269, 2004

[17] A Zholents and W Fawley, "Proposal for intense attosecond radiation from an x-ray free-electron laser," *Physical Review Letters*, vol 92, no 22, p 224801, 2005

[18] D Lowney, P Heimann, H Padmore, E Gullikson, A MacPhee, and R Falcone, "Characterization of CsI photocathodes at grazing incidence for use in a unit quantum efficiency x-ray streak camera," *Review of Scientific Instruments*, vol 75, no 10, pp 3131–3137, 2004

[19] A Zholents and M Zolotorev, "Femtosecond x-ray pulses of synchrotron radiation," *Physical Review Letters*, vol 76, no 5, pp 912–915, 1996

[20] R Schoenlein, S Chattopadhyay, H Chong, T Glover, P Heimann, C Shank, A Zholents, and M Zolotorev, "Generation of femtosecond pulses of synchrotron radiation," *Science*, vol 287, pp 2237–2240, March 2000

[21] J Schwinger, "On the classical radiation of accelerated electrons," *Physical Review*, vol 75, no 12, pp 1912–1925, 1949

[22] H Winick, *Synchrotron Radiation Sources* World Scientific Publishing Co , 1995

[23] C Belzile, J Kieffer, C Cote, T Oksenhendler, and D Kaplan, "Jitter-free subpicosecond streak cameras," *Review of Scientific Instruments*, vol 73, no 3, pp 1617–1620, 2002

[24] J Courtney-Pratt, "A new method for the photographic study of fast transient phenomena," *Research*, vol 2, pp 287–294, 1949

[25] M Man Shakya and Z Chang, "Achieving 280 fs resolution with a streak camera by reducing the deflection dispersion," *Applied Physics Letters*, vol 87, no 4, p 041103, 2005

[26] E Zavoisky and S Fanchenko, "Image converter for high-spped photography with 10^{-9}–10^{-14} sec time resolution," *Applied Optics*, vol 4, no 9, pp 1155–, 1965

[27] P Gallant, P Forget, F Dorchies, Z Jiang, J Kieffer, P Jaanimagi, J Rebuffie, C Goulmy, J Pelletier, and M Sutton, "Characterization of a subpicosecond x-ray streak camera for ultrashort laser-produced plasma experiments," *Review of Scientific Instruments*, vol 71, no 10, pp 3627–3633, 2000

[28] J Liu, J Wang, B Shan, C Wang, and Z Chang, "An accumulative x-ray streak camera with sub-600-fs temporal resolution and 50-fs timing jitter," *Applied Physics Letters*, vol 82, no 20, pp 3553–3555, 2003

[29] G Fraser, "The characterisation of soft x-ray photocathodes in the wavelength band 1–300 å I Lead glass, lithium fluoride and magnesium fluoride," *Nuclear Methods and Instruments*, vol 206, pp 251–263, 1983

[30] G Fraser, "The characterisation of soft x-ray photocathodes in the wavelength band 1–300 å II Caesium iodide and other insulators of high photoelectric yield," *Nuclear Methods and Instruments*, vol 206, pp 265–279, 1983

[31] S Woutersen, U Emmerichs, and H Bakker, "Femtosecond mid-IR pump-probe spectroscopy of liquid water Evidence for a two-component structure," *Science*, vol 278, pp 658–660, 1997

[32] C Fecko, J Eaves, J Loparo, A Tokmakoff, and P Geissler, "Ultrafast hydrogen-bond dynamics in the infrared spectroscopy of water," *Science*, vol 301, pp 1698–1702, 2003

[33] A Soper, "Water and ice," *Science*, vol 297, pp 1288–1289, 2002

[34] M Chaplin, "Water structure and behavior," Tech Rep http //www lsbu ac uk/water, London South Bank University, 2005

[35] C Cho, S Singh, and G Robinson, "An explanation of the density maximum in water," *Physical Review Letters*, vol 76, no 10, pp 1651–1654, 1996

[36] C Cho, S Singh, and G Robinson, "Understanding all of water's anomalies with a nonlocal potential," *Journal of Chemical Physics*, vol 107, no 19, pp 7979–7988, 1997

[37] F Sette, G Ruocco, M Krisch, C Masciovecchio, R Verbeni, and U Bergmann, "Transition from normal to fast sound in liquid water," *Physical Review Letters*, vol 77, no 1, pp 83–86, 1996

[38] M Krisch, P Loubeyre, G Ruocco, F Sette, A Cunsolo, M D'Astuto, R LeToullec, M Lorenzen, A Mermet, M G, and R Verbeni, "Pressure evolution of the high-frequency sound velocity in liquid water," *Physical Review Letters*, vol 89, no 12, p 125502, 2002

[39] J Sorenson, G Hura, R Glaeser, and T Head-Gordon, "What can x-ray scattering tell us about the radial distribution functions of water?," *Journal of Chemical Physics*, vol 113, no 20, pp 9149–9161, 2000

[40] http //www el1 ph tum de/forschung/projekte/esolv en htm

[41] http //www yale edu/opa/newsr/05-07-13-02 all html

[42] http //www lsbu ac uk/water/magic html

[43] P Wernet, D Nordlund, U Bergmann, M Cavalleri, M Odelius, H Ogasawara, L Naslund, T Hirsch, L Ojamae, P Glatzel, L Pettersson, and A Nilsson, "The structure of the first coordination shell in liquid water," *Science*, vol 304, no 5673, pp 995–999, 2004

[44] J Smith, C Cappa, K Wilson, B Messer, R Cohen, and R Saykally, "Energetics of hydrogen bond network rearrangements in liquid water," *Science*, vol 306, pp 851–853, 2004

[45] G Hura, J Sorenson, R Glaeser, and T Head-Gordon, "A high-quality x-ray scattering experiment on liquid water at ambient conditions," *Journal of Chemical Physics*, vol 113, no 20, pp 9140–9148, 2000

[46] A Narten and H Levy, "Liquid water Molecular correlation functions from x-ray diffraction," *Journal of Chemical Physics*, vol 55, no 5, pp 2263–2269, 1971

[47] A Narten and H Levy, "Observed diffraction pattern and proposed models of liquid water," *Science*, vol 165, no 3892, pp 447–454, 1969

[48] T Head-Gordon and G Hura, "Water structure from scattering experiments and simulation," *Chemical Reviews*, vol 102, no 8, pp 2651–2670, 2002

[49] B Yang and J Kirz, "Extended x-ray absorption fine structure of liquid water," *Physical Review B*, vol 36, no 2, pp 1361–1364, 1987

[50] K Wilson, J Tobin, A Ankudinov, J Rehr, and R Saykally, "Extended x-ray absorption fine structure from hydrogen atoms in water," *Physical Review Letters*, vol 85, no 20, pp 4289–4292, 2000

[51] K Wilson, B Rude, T Catalano, R Schaller, J Tobin, D Co, and R Saykally, "X-ray spectroscopy of liquid water microjets," *Journal of Physical Chemistry B*, vol 105, pp 3346–3349, 2001

[52] K Wilson, R Schaller, D Co, R Saykally, B Rude, T Catalano, and J Bozek, "Surface relaxation in liquid water and methanol studied by x-ray absorption spectroscopy," *Journal of Chemical Physics*, vol 117, no 16, pp 7738–7744, 2002

[53] D Bowron, M Krisch, A Barnes, J Finney, A Kaprolat, and M Lorenzen, "X-ray-raman scattering from the oxygen K edge in liquid and solid H_2O," *Physical Review B*, vol 62, no 14, pp R9223–R9227, 2000

[54] U Bergmann, P Wernet, P Glatzel, M Cavalleri, L Pettersson, A Nilsson, and S Cramer, "X-ray Raman spectroscopy at the oxygen K edge of water and ice Implications on local structure models," *Physical Review B*, vol 66, no 9, p 092107, 2002

[55] J Guo, Y Luo, A Augustsson, J Rubensson, C Sathe, H Ågren, H Siegbahn, and J Nordgren, "X-ray emission spectroscopy of hydrogen bonding and electronic structure of liquid water," *Physical Review Letters*, vol 89, no 13, p 137402, 2002

[56] M Odelius, H Ogasawara, D Nordlund, O Fuchs, L Weinhardt, F Maier, E Umbach, C Heske, Y Zubavichus, M Grunze, J Denlinger, L Pettersson, and A Nilsson, "Ultrafast core-hole-induced dynamics in water probed by x-ray emission spectroscopy," *Physical Review Letters*, vol 94, no 22, p 227401, 2005

[57] J Polo and P Egelstaff, "Neutron-diffraction study of low-temperature water," *Physical Review A*, vol 27, no 3, pp 1508–1514, 1983

[58] J Dore, M Sufi, and M Bellissent-Funel, "Structural change in D_2O water as a function of temperature the isochoric temperature derivative function for neutron diffraction," *Physical Chemistry Chemical Physics*, vol 2, no 8, pp 1599–1602, 2000

[59] D Prendergast, J Grossman, and G Galli, "The electronic structure of liquid water within density-functional theory," *Journal of Chemical Physics*, vol 123, no 1, p 014501, 2005

[60] E Schwegler, J Grossman, F Gygi, and G Galli, "Towards an assessment of the accuracy of density functional theory for first principles simulations of water II," *Journal of Chemical Physics*, vol 121, no 11, pp 5400–5409, 2004

[61] Y Luo, H Ågren, and F Gel'mukhanov, "Symmetry assignments of occupied and unoccupied molecular orbitals through spectra of polarized resonance inelastic x-ray scattering," *Journal of Physics B Atomic, Molecular and Optical Physics*, vol 27, pp 4169–4180, 1994

[62] P R B, "Calculations of near-edge x-ray-absorption spectra of gas-phase and chemisorbed molecules by means of density-functional and transition-potential theory," vol 58, no 12, pp 8097–8110, 1998

[63] B Tomberli, C Benmore, P Egelstaff, J Neuefeind, and V Honkimaki, "Isotopic quantum effects in water structure measured with high energy photon diffraction," *Journal of Physics Condensed Matter*, vol 12, pp 2597–2612, 2000

[64] J Stohr, *NEXAFS Spectroscopy* Springer-Verlag, 2003

[65] B Teo, *EXAFS Basic Principles and Data Analysis* Springer-Verlag, 1986

[66] U Bergmann, P Glatzel, and S Cramer, "Bulk-sensitive XAS characterization of light elements from X-ray Raman scattering to X-ray Raman spectroscopy," *Microchemical Journal*, vol 71, pp 221–230, 2002

[67] Y Zubavicus and M Grunze, "New insights into the structure of water with ultra-fast probes," *Science*, vol 304, pp 974–976, 2004

[68] M Rini, B Magnes, E Pines, and E Nibbering, "Real-time observation of bimodal proton transfer in acid-base pairs in water," *Science*, vol 301, pp 349–352, 2003

[69] A Omta, M Kropman, S Woutersen, and H Bakker, "Negligible effect of ions on the hydrogen-bond structure in liquid water," *Science*, vol 301, pp 347–349, 2003

[70] M Miyazaki, A Fujii, T Ebata, and N Mikami, "Infrared spectroscopic evidence for protonated water clusters forming nanoscales cages," *Science*, vol 304, no 5674, pp 1134–1137, 2004

[71] J Shin, N Hammer, E Diken, M Johnson, R Walters, T Jaeger, M Duncan, R Christie, and K Jordan, "Infrared signature of structure associated with the $H^+(H_2O)_n$ (n = 6 to 27) clusters," *Science*, vol 304, no 5674, pp 1137–1140, 2004

[72] D Paik, I Lee, D Yang, J Baskin, and A Zewail, "Electrons in finite-sized water cavities Hydration dynamics observed in real time," *Science*, vol 306, no 5696, pp 672–675, 2004

[73] A Bragg, J Verlet, A Kammrath, O Cheshnovcky, and D Neumark, "Hydrated electron dynamics From clusters to bulk," *Science*, vol 306, no 5696, pp 669–671, 2004

[74] C Ruan, V Lobastov, F Vigliotti, S Chen, and A Zewail, "Ultrafast electron crystallography of interfacial water," *Science*, vol 304, pp 80–84, 2004

[75] J Stenger, D Madsen, P Hamm, E Nibbering, and T Elsaesser, "Ultrafast vibrational dephasing of liquid water," *Physical Review Letters*, vol 87, no 2, 2001

[76] M Mizuno and T Tahara, "Novel resonance Raman enhancement of local structure around solvated electrons in water," *Journal of Physical Chemistry A*, vol 105, no 39, pp 8823–8826, 2001

[77] S Walbran and A Kornyshev, "Proton transport in polarizable water," *Journal of Chemical Physics*, vol 114, no 22, pp 10039–10048, 2001

[78] N Agmon, "The Grotthuss mechanism," *Chemical Physics Letters*, vol 244, pp 456–462, 1995

[79] D Marx, M Tuckerman, J Hutter, and M Parrinello, "The nature of the hydrated excess proton in water," *Nature*, vol 397, pp 601–604, 1999

[80] A Reuther, A Laubereau, and D Nikogosyan, "Primary photochemical processes in water," *Journal of Physical Chemistry*, vol 100, pp 16794–16800, 1996

[81] R Laenen, T Roth, and A Laubereau, "Novel precursors of solvated electrons in water Evidence for a charge transfer process," *Physical Review Letters*, vol 85, no 1, pp 50–53, 2000

[82] R Bowman, H Lu, and K Eisenthal, "Femtosecond study of geminate electron-hole recombination in neat alkanes," *Journal of Chemical Physics*, vol 89, no 1, pp 606–608, 1988

[83] N Hammer, J Shin, J Headrick, E Diken, J Roscioli, G Weddle, and M Johnson, "How do small water clusters bind an excess electron?," *Science*, vol 306, pp 675–679, 2004

[84] L Bosio, S Chen, and J Teixeira, "Isochoric temperature differential of the x-ray structure factor and structural rearrangements in low-temperature heavy water," *Physical Review A*, vol 27, no 3, pp 1468–1475, 1983

[85] A Plech, M Wulff, S Bratos, F Mirloup, R Vuilleumier, F Schotte, and P Anfinrud, "Visualizing chemical reactions in solution by picosecond x-ray diffraction," *Physical Review Letters*, vol 92, no 12, p 125505, 2004

[86] H Ihee, M Lorenc, T Kim, Q Kong, M Cammarata, J Lee, S Bratos, and M Wulff, "Ultrafast x-ray diffraction of transient molecular structures in solution," *Science*, vol 309, pp 1223–1227, 2005

[87] R Crowell, R Lian, I Shkrob, J Qian, D Oulianov, and S Pommeret, "Light-induced temperature jump causes power-dependent ultrafast kinetics of electrons generated in multiphoton ionization of liquid water," *Journal of Physical Chemistry A*, vol 108, no 42, pp 9105–9114, 2004

[88] A Lindenberg, I Kang, S Johnson, T Missalla, P Heimann, Z Chang, J Larsson, P Bucksbaum, H Kapteyn, H Padmore, R Lee, J Wark, and R Falcone, "Time-resolved x-ray diffraction from coherent phonons during a laser-induced phase transition," *Physical Review Letters*, vol 84, no 1, pp 111–114, 2000

[89] C Bressler, M Saes, M Chergui, R Abela, and P Pattison, "Optimizing a time-resolved x-ray absorption experiment," *Nuclear Instruments and Methods in Physics Research A*, vol 467–468, pp 1444–1446, 2001

[90] B Henke, J Liesegang, and S Smith, "Soft-x-ray-induced secondary-electron emission from semiconductors and insulators Models and measurements," *Physical Review B*, vol 19, no 6, pp 3004–3021, 1979

[91] B Henke, J Knauer, and K Premaratne, "The characterization of x-ray photocathodes in the 0 1–10 keV photon energy region," *Journal of Applied Physics*, vol 52, no 3, pp 1509–1520, 1981

[92] B Henke, "Ultrasoft-X-Ray Reflection, Refraction, and Production of Photoelectrons (100–100-eV Region)," *Physical Review A*, vol 6, no 1, pp 94–104, 1972

[93] L Eliseenko, V Shchemelev, and M Rumsh, "Quantum yields of the surface x-ray photoeffect at 1–10 Å," *Soviet Physics – Technical Physics*, vol 13, no 1, pp 122–129, 1968

[94] A Akkerman, A Breskin, R Chechik, and A Gibrekhterman, "Secondary electron emission from alkali halides induced by x-rays and electrons," in *Ionization of Solids by Heavy Particles* (R Baragiola, ed), pp 359–380, Plenum Press, New York, 1993

[95] T Boutboul, A Akkerman, A Gibrekhterman, A Breskin, and R Chechik, "An improved model for ultraviolet- and x-ray-induced electron emission from CsI," *Journal of Applied Physics*, vol 86, no 10, pp 5841–5849, 1999

[96] A Akkerman, T Boutboul, A Breskin, R Chechik, and A Gibrekhterman, "Low-energy electron transport in alkali halides," *Journal of Applied Physics*, vol 76, no 8, pp 4656–4662, 1994

[97] A Akkerman, A Gibrekhterman, A Breskin, and R Chechik, "Monte Carlo simulations of secondary electron emission from CsI, induced by 1–10 keV x rays and electrons," *Journal of Applied Physics*, vol 72, no 11, pp 5429–5436, 1992

[98] A Akkerman, T Boutboul, A Breskin, R Chechik, A Gibrekhterman, and Y Lifshitz, "Inelastic electron interactions in the energy range 50 eV to 10 keV in insulators alkali halides and metal oxides," *Physica Status Solidi (b)*, vol 198, pp 769–784, 1996

[99] T Boutboul, A Akkerman, A Breskin, and R Chechik, "Electron inelastic mean free path and stopping power modelling in alkali halides in the 50 eV–10 keV energy range," *Journal of Applied Physics*, vol 79, no 9, pp 6714–6721, 1996

[100] A Gibrekhterman, A Akkerman, A Breskin, and R Chechik, "Spatial characteristics of electron- and photon-induced secondary electron cascades in CsI," *Journal of Applied Physics*, vol 76, no 3, pp 1676–1680, 1994

[101] T Boutboul, A Breskin, R Chechik, A Braem, and G Lion, "Ultraviolet photoabsorption measurements in alkali iodide and caesium bromide evaporated films," *Journal of Applied Physics*, vol 83, no 12, pp 7896–7899, 1998

[102] T Boutboul, A Akkerman, A Breskin, and R Chechik, "Escape length of ultraviolet induced photoelectrons in alkali iodide and CsBr evaporated films Measurements and modelling," *Journal of Applied Physics*, vol 84, no 5, pp 2890–2896, 1998

[103] A Gibrekhterman, A Akkerman, A Breskin, and R Chechik, "Characteristics of secondary electron emission from CsI induced by x rays with energies up to 100 keV," *Journal of Applied Physics*, vol 74, no 12, pp 7506–7509, 1993

[104] E Savinov and V Shchemelev, "Statistics of the external x-ray photoelectric effect of bulk cathodes," *Soviet Physics JETP*, vol 35, no 4, pp 741–745, 1971

[105] G Fraser and J Pearson, "Soft x-ray energy resolution with microchannel plate detectors of high quantum efficiency," *Nuclear Instruments and Methods in Physics Research*, vol 219, pp 199–212, 1984

[106] K Herrmann and M Korn, "Measurement of the detection quantum efficiency of microchannel plates for medium energy electrons," *Journal of Physics E Scientific Instruments*, vol 20, pp 177–181, 1987

[107] B Henke, E Gullikson, and J Davis, "X-ray interactions Photoabsorption, scattering, transmission, and reflection at $E = 50$–$30,000$ eV, Z=1–92," *Atomic Data and Nuclear Data Tables*, vol 54, no 2, pp 181–342, 1993

[108] J Underwood, E Gullikson, M Koike, P Batson, P Denham, K Franck, R Tackaberry, and W Steele, "Calibration and standards beamline 6 3 2 at the Advanced Light Source," *Review of Scientific Instruments*, vol 67, no 9, pp 1–5, 1996

[109] F Scholze, H Henneken, P Kuschnerus, H Rabus, M Richter, and G Ulm, "Determination of the electron-hole pair creation energy for semiconductors from the spectral responsivity of photodiodes," *Nuclear Instruments and Methods in Physics Research A*, vol 439, pp 208–215, 2000

[110] http //www detechinc com

[111] E Gullikson and B Henke, "X-ray-mduced secondary-electron emission from solid xenon," *Physical Review B*, vol 39, no 1, pp 1–9, 1989

[112] M Cardona, R Haensel, D Lynch, and B Sonntag, "Optical properties of the rubidium and cesium halides in the extreme ultraviolet," *Physical Review B*, vol 2, no 4, pp 1117–1131, 1970

[113] A Buzulutskov, A Breskin, and R Chechik, "Field enhancement of the photo-electric and secondary electron emission from CsI," *Journal of Applied Physics*, vol 77, no 5, pp 2138–2145, 1995

[114] G Fraser, "The characterisation of soft X-ray transmission photocathodes," *Nuclear Instruments and Methods in Physics Research*, vol 228, pp 532–540, 1985

[115] R Schoenlein, S Chattopadhyay, H Chong, T Glover, P Heimann, W Leemans, C Shank, A Zholents, and M Zolotorev, "Generation of femtosecond x-ray pulses via laser-electron beam interaction," *Applied Physics B Lasers and Optics*, vol 71, no 1, pp 1–10, 2000

[116] J Byrd, W Leemans, A Loftsdottir, B Marcelis, M Martin, W McKinney, F Sannibale, T Scarvie, and C Steier, "Observation of broadband self-amplified spontaneous coherent terahertz synchrotron radiation in a storage ring," *Physical Review Letters*, vol 89, p 224801, 2002

[117] P Heimann, H Padmore, and R Schoenlein, "ALS beamline 6 0 for ultrafast x-ray absorption spectroscopy," *AIP Conference Proceedings*, vol 705, no 1, pp 1407–1410, 2004

[118] D Weinstein, "The ultrafast x-ray streak camera honors thesis," tech rep, Physics Department, University of California, Berkeley, May 2004

[119] S Johnson, P Heimann, A Lindenberg, H Jeschke, M Garcia, Z Chang, R Lee, J Rehr, and R Falcone, "Properties of liquid silicon observed by time-resolved x-ray absorption spectroscopy," *Physical Review Letters*, vol 91, no 15, p 157403, 2000

[120] S Johnson, *Ultrafast X-Ray Absorption Spectroscopy Properties of Liquid Silicon and Carbon* PhD thesis, Physics Department, University of California, Berkeley, 2002

[121] B Shan, Z Chang, J Liu, X Liu, S Gao, Y Ren, W Zhu, Y Luo, J Cheng, C Yang, T Wen, D Tang, S Wen, and A Zheng, "Gated MCP framing camera system," in *Proceedings of SPIE 22nd International Congress on High-Speed Photography and Photonics* (D Paisley and A Frank, eds), vol 2869, pp 182–188, May 1997

[122] W Thur, R DeMarco, B Baldock, and K Rex, "Rigid, adjustable support of aligned elements via six struts," tech rep, Lawrence Berkeley National Laboratory, October 1997

[123] Z Chang, A Rundquist, J Zhou, J Murnane, H Kapteyn, X Liu, B Shan, J Liu, L Niu, M Gong, and X Zhang, "Demonstration of a sub-picosecond x-ray streak camera," *Applied Physics Letters*, vol 69, no 1, pp 133–135, 1996

[124] K Halbach and R Holsinger, "SUPERFISH - a computer program for evaluation of RF cavities with cylindrical symmetry," *Particle Accelerators*, vol 7, pp 213–222, 1976

[125] L Young, "PARMELLA," Tech Rep LA-UR-96-1835, Los Alamos National Laboratory, 1996

[126] B Qian and H Elsayed-Ali, "Electron pulse broadening due to space charge effects in a photoelectron gun for electron diffraction and streak camera systems," *Journal of Applied Physics*, vol 91, no 1, pp 462–468, 2002

[127] B Siwick, J Dwyer, R Jordan, and R Miller *Journal of Applied Physics*, vol 92, no 3, pp 1643–1648, 2002

[128] A El-Kareh and J El-Kareh, *Electron Beams, Lenses, and Optics*, vol 1, ch VII, pp 246–279 Academic Press, 1970

[129] P Sarma, S Pattanayak, and R Bhandari, "Improvement of field quality of Glaser magnets used for focusing ion beams," *Nuclear Instruments and Methods in Physics Research A*, vol 426, pp 243–248, 1999

[130] P Sarma, S Pattanayak, D Bandyopadhyay, and R Bhandari, "A Glaser magnet of improved field quality," *Nuclear Instruments and Methods in Physics Research A*, vol 432, pp 534–538, 1999

[131] H. Atwater, "Tests of microstrip dispersion formulas," *IEEE Transactions on Microwave Theory and Techniques*, vol. 36, no. 3, pp. 619–621, 1997.

[132] H. Wheeler, "Transmission-line properties of a strip on a dielectric sheet on a plane," *IEEE Transactions on Microwave Theory and Techniques*, vol. MTT-25, no. 8, pp. 631–647, 1997.

[133] M. Kirschning and R. Jansen, "Accurate model for effect dielectric constant of microstrip with validity up to millimetre-wave frequencies," *Electronics Letters*, vol. 18, no. 6, pp. 272–273, 1982.

[134] B. Wadell, *Transmission line design handbook*, pp. 94–95. Artech House, Inc., 1991.

[135] D. Brooks, "Crosstalk, part 1 understanding forward vs. backward," tech. rep., UltraCAD Design Inc. & Mentor Graphics, November 2003.

[136] D. Brooks, "Adjusting Signal Timing (Part 2), Crosstalk effects in serpentine traces," tech. rep., UltraCAD Design Inc. & Mentor Graphics, January 2004.

[137] D. Piscotty, J. Ferry, and R. Elco, "The Samtech Golden Standard: A Reference Structure for Electrical Simulation and Measurement: Part II," tech. rep., Samtech, Inc., January 2005.

[138] M. Kirschning and R. Jansen, "Accurate wide-range design equations for the frequency-dependent characteristic of parallel coupled microstrip lines," *IEEE Transactions on Microwave Theory and Techniques*, vol. MTT-32, no. 1, pp. 83–90, 1984.

[139] M. Kirschning and R. Jansen, "Corrections to "accurate wide-range design equations for the frequency-dependent characteristic of parallel coupled microstrip lines"," *IEEE Transactions on Microwave Theory and Techniques*, vol. MTT-33, no. 3, p. 288, 1985.

[140] R. Jansen and M. Kirschning, "Arguments and an accurate model fro the power-current formulation of microstrip characteristic impendance," *Arhiv Feur Elektrischnen Übertragung (AEU)*, vol. 37, no. 3–4, pp. 108–112, 1983.

[141] M. Kirschning, R. Jansen, and N. Koster, "Measurement and computer-aided modeling of microstrip discontinuities by an improved resonator method," *IEEE Microwave Symposium Digest, MTT-S International*, vol. 83, no. 1, pp. 495–497, 1983.

[142] M. Murnane, H. Kapteyn, and R. Falcone, "X-ray streak camera with 2 ps response," *Applied Physics Letters*, vol. 56, no. 20, pp. 1948–1950, 1990.

[143] M. Saes, F. van Mourik, W. Gawelda, M. Kaiser, M. Chergui, D. Grolimund, R. Abela, T. Glover, P. Heimann, R. Schoenlein, S. Johnson, A. Lindenberg, and R. Falcone, "A setup for ultrafast time-resolved x-ray absorption spectroscopy," *Review of Scientific Instruments*, vol. 75, no. 1, pp. 24–30, 2004.

[144] A Mudi and C Chakravarty, "Multiple time-scale behavior of the hydrogen-bond network in water," *Journal of Physical Chemistry B*, vol 108, no 51, pp 19607–19613, 2004

[145] F Sciortino, P Poole, H Stanley, and S Havlin, "Lifetime of the bond network and gel-like anomalies in supercooled water," *Physical Review Letters*, vol 64, no 14, pp 1686–1689, 1990

[146] P Debenedetti and H Stanley, "Supercooled and glassy water," *Physics Today*, vol 56, no 6, p 40

[147] J Errington, P Debenedetti, and S Torquato, "Cooperative origin of low-density domains in liquid water," *Physical Review Letters*, vol 89, no 21, p 215503, 2002

[148] B Warren, *X-ray Diffraction* Dover Publications, Inc , 1990

[149] R Pathria, *Statistical Mechanics*, pp 456–459 Butterworth-Heinemann, 1996

[150] D Lowney, "Analysis of the structural and optoelectronic properties of semiconductor materials and devices using photoacoustic spectroscopy and synchrotron x-ray topography," Master's thesis, School of Electronic Engineering, Dublin City University, Ireland, 2002

[151] J Jackson, *Classical Electrodynamics*, ch 9, pp 407–413 John Wiley & Sons, Inc , 1999

[152] M Tauber, R Mathies, X Chen, and S Bradforth, "Flowing liquid sample jet for resonance Raman and ultrafast optical spectroscopy," *Review of Scientific Instruments*, vol 74, no 11, pp 4958–4960, 2003

[153] F Mirloup, S Bratos, R Vuilleumier, M Wulff, and A Plech, *Femtochemistry and Femtobiology Ultrafast Events in Molecular Science*, pp 349–352 New York Elsevier, 2004

[154] P Egelstaff and J Polo, "Structural changes in low temperature water," *Chemical Physics*, vol 101, no 1, pp 175–181, 1986

[155] S Pommeret, F Gobert, M Mostafavi, I Lampre, and J Mialocq, "Femtochemistry of the hydrated electron at decimolar concentration," vol 105, no 51, pp 11400–11406, 2001

[156] P Rossky and J Schnitker, "The hydrated electron Quantum simulation of structure, spectroscopy, and dynamics," *Journal of Physical Chemistry*, vol 92, no 15, pp 4277–4285, 1988

[157] T Tran-Thi, T Gustavsson, C Prayer, S Pommeret, and J Hynes, "Primary ultrafast events preceeding the photoinduced proton transfer from pyranine to water," *Chemical Physics Letters*, vol 329, no 5–6, pp 421–430, 2000

[158] E Pines and D Huppert, "pH jump A relaxational approach," *Journal of Physical Chemistry*, vol 87, no 22, pp 4471–4478, 1983

[159] N Agmon, "Elementary steps in excited-state proton transfer," *Journal of Physical Chemistry A*, vol 109, no 1, pp 13–35, 2005

[160] P Jaanimagi, "Breaking the 100-fs barrier with a streak camera," in *Proceedings of SPIE Fourth-Generation X-Ray Sources and Ultrafast X-Ray Detectors* (R Tatchyn, Z Chang, J Kieffer, and J Hastings, eds), vol 5194, pp 171–182, January 2004

[161] J Feng, W Wan, J Qiang, A Bartlet, A Comin, A Scholl, J Byrd, R Falcone, G Huang, A MacPhee, J Nasiatka, K Opachich, D Weinstein, T Young, and H Padmore, "An ultra-fast x-ray streak camera for the study of magnetization dynamics," in *Proceedings of SPIE Ultrafast X-Ray Detectors, High-Speed Imaging, and Applications* (S Kleinfelder, D Paisley, J Chang, Z abd Kieffer, and J Hastings, eds), vol 592009, p 592009, September 2005

[162] G Vale, "The peculiarities of colour centre production in doped alkali halides," *Physica Status Solidi (b)*, vol 197, pp 293–297, 1996

[163] U Jain and A Lidiard, "The growth of colloidal centres in irradiated alkali halides," *Philosophical Magazine*, vol 35, no 1, pp 245–259, 1977

[164] A Shih, J yater, P Pehrsson, J Butler, C Hor, and R Abrams, "Secondary electron emission from diamond surfaces," *Journal of Applied Physics*, vol 82, no 4, pp 1860–1867, 1997

[165] P Emma, R Iverson, P Krejcik, J Raimondi, and X Safrarek, "Femtosecond electron bunch lengths in the SLAC FFTB beamline," in *Proceedings of the 2001 Particle Accelerator Conference (PAC2001)* (P Lucas and S Webber, eds), pp 4038–4040, 2001

[166] P Krejcik, F Decker, P Emma, K Hacker, L Hendrickson, C O'Connell, H Schlarb, H Smith, and M Stanek, "Commissioning of the SPPS linac bunch compressor," in *Proceedings of the 2003 Particle Accelerator Conference (PAC2003)* (J Chew, ed), pp 423–425, 2003

[167] K Wilson, B Rude, J Smith, C Cappa, D Co, R Schaller, M Larsson, T Catalano, and R Saykally, "Investigation of volatile liquid surfaces by synchrotron x-ray spectroscopy of liquid microjets," *Review of Scientific Instruments*, vol 75, no 3, pp 725–736, 2004

[168] D Spence, J Evans, W Sleat, and W Sibbett, "Regeneratively initiated self-mode locked Ti sapphire laser," *Optics Letters*, vol 16, pp 1762–1764, 1991

[169] S Backus, C Durfee, M Murnane, and H Kapteyn, "High power ultrafast lasers," *Review of Scientific Instruments*, vol 69, no 3, pp 1207–1223, 1998

Appendix A: Experimental Issues

The time-resolved measurements of Chapters 3 and 4 were performed at the bend magnet beamline 5 3 1 at the Advanced Light Source The purpose of this appendix is to briefly describe the temporal synchronisation of the femtosecond laser system to the synchrotron radiation source In particular, the time structure of the x-ray radiation is examined and the salient features of the laser x-ray synchronisation system are presented For a general discussion on synchrotron x-ray sources the reader is referred to [22, 150] and the references contained therein A more in-depth discussion of the synchronisation system can be found in [120]

Time Structure of the Advanced Light Source

The Advanced Light Source is a third generation synchrotron source with an electron energy of 1 9 GeV The radiation spectrum extends from infrared photon energies to hard x-ray The RF system of the synchrotron operates at 500 MHz yielding an electron bucket to bucket temporal spacing of 2 ns The synchrotron typically operates in a multi-bunch fill pattern wherein electrons occupy 276 buckets of a possible 328 Typically buckets 1 through 276 are filled and the remainder are empty, except bucket 312 This bucket, referred to as the camshaft bucket, is filled with approximately five times the charge of the other buckets The light output follows the electron bunch pattern Thus a train of light pulses separated by 2 ns, with a dark region of 72 ns preceding a bright camshaft pulse and another dark region of 34 ns, is output from the source The round-trip time is 656 ns This is illustrated in Figure 5 1 The camshaft pulse has a nominal duration of

70 ps but electron-electron scattering within the bucket over the course of a fill can cause this to change slightly
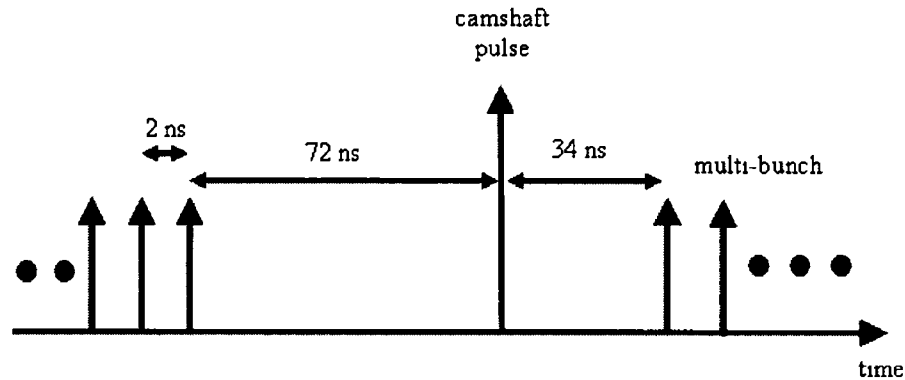

Figure 5 1   Synchrotron radiation pulse train output from the ALS

Laser X-ray Synchronisation

A Ti Al$_2$O$_3$ based laser system was used in all experiments The output from a Kerr-lens mode-locked oscillator was amplified using a regenerative amplifier in series with a two-pass amplifier A detailed review of the technology involved can be found in [168, 169] 150 fs pulses with a central wavelength of 800 nm and pulse energy of 2 mJ were output from the system at 1 kHz repetition rate

The optical path length for one round-trip of the oscillator cavity is 3 6 m, thus output pulses are separated by 12 ns Phase locking of the oscillator to the storage ring is achieved as follows The pulse train output from the oscillator is monitored by a fast diode The signal is filtered using a bandpass filter with a central frequency of 500 MHz, thereby isolating the 6th harmonic of the signal (corresponding to 2 ns or 500 MHz) This is amplified and mixed with a 500 MHz signal derived from the storage ring RF system The difference signal at the mixer output enters a phase locked-loop (PLL) and is low-pass, filtered (cut-off frequency 100 kHz) The laser oscillator cavity end-mirror is mounted on a piezoelectric crystal Thus a high voltage signal proportional to the error signal at the PLL input is fed back to the cavity mirror and alters the cavity length keeping the beat

113

frequency zero. The laser oscillator is functionally equivalent to a voltage controlled oscillator (VCO) with the feed back loop ensuring phase lock between the oscillator and the storage ring RF.

An I-Q vector modulator is inserted in the signal path of the storage ring RF signal. This device provides a means of electronically varying the phase between the synchrotron RF (x-ray pulse) and the oscillator output pulse. Essentially the device operates by taking a weighted sum of the RF signal with a 90 degree phase shifted version of itself. Thus relative delays of ±6 ns between the laser and x-ray pulses can be achieved with an accuracy better than 10 ps. Long-term drift in the oscillator cavity, for example due to thermal expansion/contraction, is compensated for by mounting the output coupler mirror on a picomotor translation stage. Thus the cavity control is kept within the range of the phase shifter using the picomotor. All the hardware is controlled from a PC as shown in Figure 5.2.
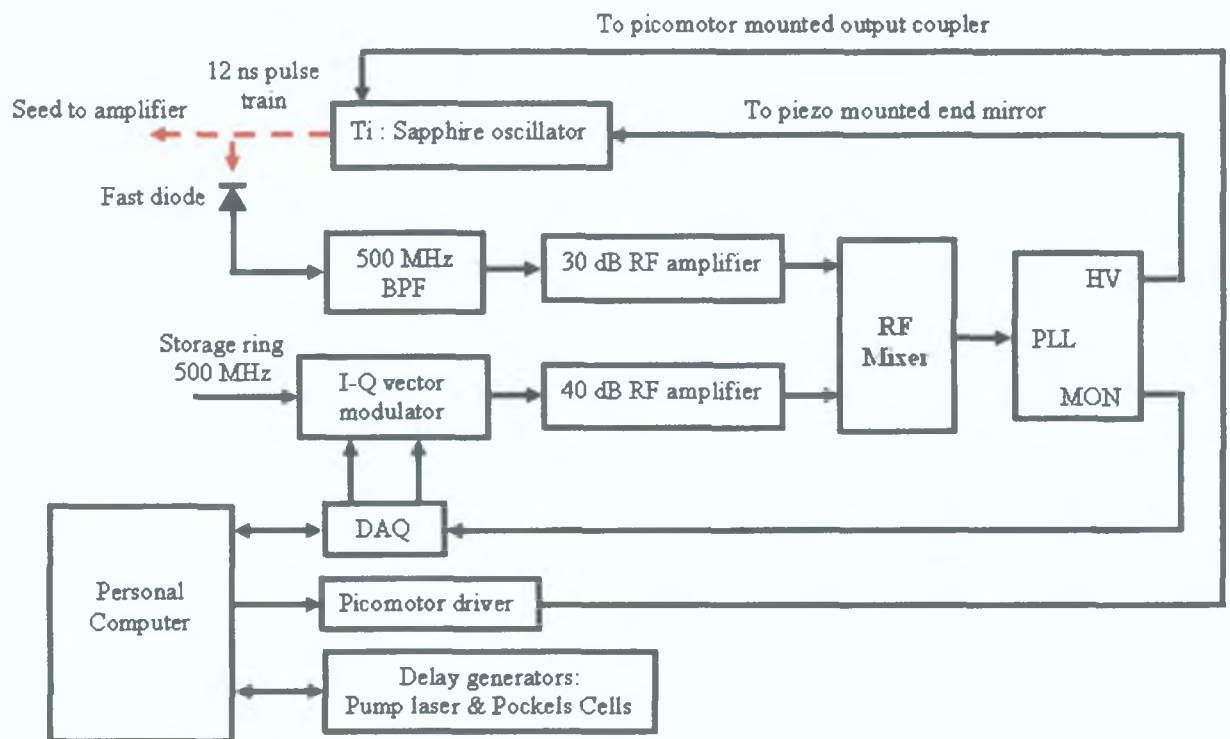

Figure 5.2: Oscillator-synchrotron synchronisation mechanism.

The timing triggers to the amplifier pump lasers and the Pockels cells in the regenerative amplifier also have to be synchronised to the storage ring The least common multiple of the oscillator pulse tram period (12 ns) and the round-trip time of the synchrotron (656 ns) is 1968 ns (corresponding to 510 kHz) 510 kHz is one third of the round-trip frequency 1 52 MHz (corresponding to 656 ns) The x-ray chopper used at the beamline is typically free running at 2 kHz with respect to the storage ring The chopper is run at twice the laser repetition frequency to facilitate the differencing technique discussed in Chapter 4 This signal is combined with a 510 kHz signal (derived from the round-trip signal provided by the storage ring RF system) in a delay flip-flop (DFF) The output of the DFF is a signal that is synchronised to both the chopper window and the synchrotron RF Using a toggle flip-flop (TFF) a 1 kHz signal is generated from this signal This in turn triggers the delay generators that are used to trigger the pump laser flashlamps and the Pockel cells in the regenerative amplifier This ensures the phased-locked oscillator pulse is amplified and delivered to the sample / photoconductive switch at the same time as the camshaft probe A schematic of the system is shown in Figure 5 3
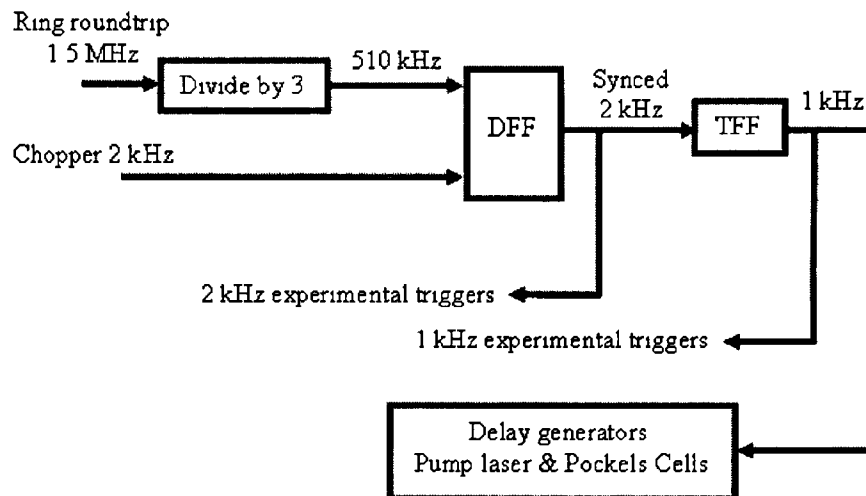

Figure 5 3 Laser amplifier-synchrotron synchronisation mechanism

To alter the relative timing of the laser pulse with respect to the camshaft pulse by an amount Δt, the phase shifter is moved by Δt mod 2 ns This ensures the oscillator pulses are at the correct relative timing The delay generators are also shifted by Δt